Validation of 3D Digital Image Correlation Incremental Hole Drilling Residual Stress Measurement

A Thesis Presented for the

Master of Science

Degree

The University of Tennessee, Knoxville

Chloe E. Mehelic

December 2025

Copyright © 2025 by Chloe Mehelic
All rights reserved.

ACKNOWLEDGEMENTS

I want to express my most sincere gratitude to everyone who made this work possible. I received constant support from my family, friends, mentors, advisors, and staff at UT. To my parents and siblings, thank you for believing in me and supporting me throughout my journey in completing this thesis, and for setting such high standards of what an education means. Thank you to my close friends for your constant encouragement and inquiries about my work.

Thank you to my committee led by Dr. Dayakar Penumadu for all the advice and support throughout my research. Dr. Penumadu, thank you for the opportunity to complete this research and for the confidence you have instilled in me throughout the process. Thank you to Dr. Jeff Bunn for extensive mentoring in the field of neutron diffraction. Thank you to Dr. Mark Denavit for helping me tie the importance of my research to the field of structural engineering through graduate level courses.

To the gifted researchers that I've met through Dr. Penumadu's research group, thank you for your advice, words of encouragement, and unwavering support. My undergraduate research assistants, Dylan Rogers, Griffin Heile, Helena Rohan, Katie Keegan, and Vlad Wheeler were essential in the development of my testing procedure. I greatly appreciated all the hours you spent assisting me in the shop and the lab. The most influential person throughout my graduate career has undoubtedly been Hannah Maeser. Hannah, thank you for sharing all of your knowledge with me and for being such a great supporter throughout the development of this project.

Thank you to the staff in the civil engineering department for the constant support and resources you all provided me with. To Andy Baker and Larry Roberts, thank you for getting the CNC set up in the machine shop, for preparing my samples, and all the other support. To Ken Thomas, thank you for your advice, constant assistance, and the time you took to help me learn and grow as an engineer. Thank you to Dr. Mobley and Dr. Retherford for seeing my potential as a researcher, for recruiting undergraduate students

to work on my project, and for your unending advice and support. To all other faculty and staff in the civil engineering department, thank you for the work you do that allows me and other students to learn.

ABSTRACT

Residual stresses within alloys can result from a multitude of complex processes associated with additive and subtractive manufacturing, extrusion, casting, machining, and welding due to thermo-mechanical loading. Residual stress within a structural element can lead to early yielding and premature failure of the part. Cyclical and long-term use of structural elements can lead to the development of residual stress. The importance and presence of residual stress extend into structural, aerospace, materials engineering, and other sectors where the resulting failure is catastrophic. The ability to accurately measure residual stresses within a structural component is essential to the lifetime of the part. Many methods currently exist for measuring residual stress, including diffraction-based techniques, compliance, curvature, and blind hole drilling.

Blind hole drilling is an advantageous measurement technique because it is semi-destructive and can be implemented in an engineering setting. Blind hole drilling is conventionally completed with typical strain gauge rosettes, as outlined in ASTM E837. A major drawback of standard strain gauge rosettes is the lack of measurement area available. Strain gauge rosettes also require precise and time-consuming preparation, require precise orientation on the part, and are single use. The application of 3D DIC (three-dimensional digital image correlation) to the blind hole drilling method provides a larger measurement area and simplifies sample preparation. In this study, 3D DIC is applied to the blind hole drilling method of measuring residual stress. The traditional method of residual stress calculation for incremental hole drilling, the integral method, is applied to 3D DIC. The 3D DIC integral method results are compared to a newly proposed method which uses radial displacements and calibration coefficients derived from finite element models to increase the accuracy of residual stress measurement.

Mesoscopic (Type II) and microscopic (Type I) residual stresses are typically of academic interest, while Type I bulk residual stresses are of highest importance for engineering applications. Type I residual stresses are addressed in this study by improving on the ASTM hole drilling procedure with the application of 3D DIC. The

integrated 3D DIC application to the incremental hole drilling procedure is verified by traditional strain gauge rosette measurements and with known applied stress in 4-point bending. A full residual stress analysis of a shrink fit ring and plug sample is evaluated in this study with measurement by hole drilling with standard strain gauge rosette and 3D DIC, x-ray diffraction, neutron diffraction, and preliminary Bragg edge imaging results.

TABLE OF CONTENTS

Chapter One Residual Stress Measurements in Alloys Using Hole Drilling Method Integrating 3-D Digital Image Correlation and Finite Element Method 1
Abstract 2
Introduction 2
Materials and Methods 5
Finite Element Analysis 5
3D DIC Camera Setup 7
4-point Bending Validation 7
3D DIC Data Filtering 10
Integral Method Analyses 12
3D DIC Radial Displacement Method Analysis 15
Results 15
Finite Element Analysis 15
Out of Plane 4-Point Bending 23
In Plane 4-Point Bending 23
Discussion 28
Finite Element Analysis 28
Finite Element Result Application to Measurement with DIC 30
3D DIC vs Strain Gauge Rosette: Radial Displacement and Integral Methods 33
Conclusions 38
Acknowledgments 39
Chapter Two Residual Stress Measurements in Alloys: Modified Hole Drilling Method versus Surface X-Ray Diffraction and Bulk Neutron Scattering 40
Abstract 41
Introduction 41
Materials and Methods 45
Ring and Plug Sample Assembly 45
Finite Element Analysis 45

Incremental Hole Drilling 46
X-Ray Diffraction 49
Neutron Diffraction 50
Bragg Edge Imaging 52
Results 52
Finite Element Analysis 52
Incremental Hole Drilling 54
X-Ray Diffraction 54
Neutron Diffraction 59
Bragg Edge Imaging 59
Discussion 59
Finite Element Analysis 59
Incremental Hole Drilling 62
X-Ray Diffraction 63
Neutron Diffraction 64
Bragg Edge Imaging 65
Conclusions 65
Acknowledgements 67
Conclusions 68
List of References 71
Appendix 74
Chapter 1: Finite Element Analysis Results 74
Chapter 1: 4-Point Bending Results 86
Chapter 1: Finite Element Analysis Discussion 90
Chapter 2: X-Ray Diffraction Ring & Plug Linear Fit Plots 91
Vita 96

LIST OF TABLES

Table 1: DIC Rosette Assemblies 14
Table 2: a Values for IHD Depths, 2.0mm Diameter Hole, 10mm Thick Plate 17
Table 3: b Values for IHD Depths, 2.0mm Diameter Hole, 10mm Thick Plate 18
Table 4: a Values for IHD Depths of 2.0mm Diameter Hole, 4mm Thick Model 74
Table 5: b Values for IHD Depths of 2.0mm Diameter Hole, 4mm Thick Model 75
Table 6: a Values for IHD Depths of 2.0mm Diameter Hole, 15mm Thick Model 76
Table 7: b Values for IHD Depths of 2.0mm Diameter Hole, 15mm Thick Model 77
Table 8: a Values for IHD Depths of 2.0mm Diameter Hole, 20mm Thick Model 78
Table 9: b Values for IHD Depths of 2.0mm Diameter Hole, 20mm Thick Model 79
Table 10: a Values for IHD Depths of 2.0mm Diameter Hole, 30mm Thick Model 80
Table 11: b Values for IHD Depths of 2.0mm Diameter Hole, 30mm Thick Model 81

LIST OF FIGURES

Figure 1: Finite Element Mesh for Radial Displacement Analysis, 20x20x8mm Plate 8
Figure 2: Finite Element Mesh for Integral Method Analysis, 20x20x8mm Plate..... 8
Figure 3: Out of Plane 4-Point Bending Fixture..... 9
Figure 4: In Plane 4-Point Bending Fixture..... 9
Figure 5: DIC Viewing Area..... 11
Figure 6: Spatial Average Filter Schematic..... 13
Figure 7: DIC Pseudo Gauges..... 13
Figure 8: Principal Stresses, 8mm Thick Al Plate, 80% Fy Uniaxial Applied Stress, Radial Displacement and Integral Methods..... 19
Figure 9: Average Principal Stresses, 8mm Thick Al Plate, 80% Fy Uniaxial Applied Stress, Radial Displacement and Integral Methods 19
Figure 10: Principal Stresses, 8mm Thick Al Plate, 20% Fy Uniaxial Applied Stress, Radial Displacement and Integral Methods..... 20
Figure 11: Principal Stresses, 8mm Thick Al Plate, 20% Fy Uniaxial Applied Stress, Radial Displacement and Integral Methods..... 20
Figure 12: Principal Stresses, 8mm Thick Ti Plate, Radial Displacement and Integral Methods..... 21
Figure 13: Average Principal Stresses, 8mm Thick Ti Plate, Radial Displacement and Integral Methods 21
Figure 14: Principal Stresses, 12mm Thick Steel Plate, Radial Displacement and Integral Methods..... 22
Figure 15: Average Principal Stresses, 12mm Thick Steel Plate, Radial Displacement and Integral Methods 22
Figure 16: Al 8mm Thick Plate, 20% Fy, Radial Displacements at Select Theta vs Hole Depth..... 24
Figure 17: Steel 8mm Thick Plate, 20% Fy, Radial Displacements at Select Theta vs Hole Depth..... 24

Figure 18: Ti 8mm Thick Plate, 20% Fy, Radial Displacements at Select Theta vs Hole Depth 25
Figure 19: Out of Plane 4-Point Bending Al Sample 25
Figure 20: Max Principal Stress Profile Comparison, Out of Plane 4-pt Bending 26
Figure 21: Average Cartesian Stress Comparison, Out of Plane 4-Point Bending 26
Figure 22: Average Principal Stress Comparison, Out of Plane 4-Point Bending 27
Figure 23: Max Principal Stress Profile Comparison, In Plane 4-pt Bending 27
Figure 24: Average Cartesian Stress Comparison, In Plane 4-Point Bending 29
Figure 25: Average Max Principal Stress Comparison, In Plane 4-pt Bending 29
Figure 26: RMS Error, FE Principal Stress Results 31
Figure 27: Max Stress Percentage Error, FE 31
Figure 28: RMS Error, Out of Plane Bending Stress Results 34
Figure 29: Max Stress Percentage Error, Out of Plane Bending 34
Figure 30: RMS Error, In Plane Bending Stress Results 35
Figure 31: Max Stress Percentage Error, In Plane Bending 37
Figure 32: Out of Plane 4-pt Bending Radial Displacement Method Results with Limited Theta Range 37
Figure 33: FE Al Ring & Plug Part 47
Figure 34: FE Al Ring & Plug Mesh 47
Figure 35: XRD Radial and Hoop Measurement Directions 51
Figure 36: Neutron Diffraction Geometry 51
Figure 37: Neutron Imaging Measurement Location 53
Figure 38: FE Radial, Hoop, and Axial Stresses 53
Figure 39: Ring & Plug After IHD 55
Figure 40: DIC Radial Displacement Results, Top of Ring 55
Figure 41: DIC Radial Displacement Results, Top of Plug 56
Figure 42: DIC Radial Displacement Results, Side of Ring 56
Figure 43: DIC Radial Displacement Method & SGR Compared to Finite Element Profiles 57

Figure 44: DIC Integral Method & SGR Compared to Finite Element Profiles 57
Figure 45: XRD Radial and Hoop Measurements & DIC Integral Method Results at Early Depths 58
Figure 46: Neutron Radial Stress 60
Figure 47: Neutron Hoop Stress 60
Figure 48: Ring & Plug Bragg Edge Results Compared to Theory 61
Figure 49: Grey Scale Summed Across Wavelength Range, Radiograph 61
Figure 50: Cartesian Stresses, 8mm Thick Al Plate, 80% Fy Uniaxial Applied Stress, Radial Displacement and Integral Methods 82
Figure 51: Average Cartesian Stresses, 8mm Thick Al Plate, 80% Fy Uniaxial Applied Stress, Radial Displacement and Integral Methods 82
Figure 52: Cartesian Stresses, 8mm Thick Al Plate, 20% Fy Uniaxial Applied Stress, Radial Displacement and Integral Methods 83
Figure 53: Average Cartesian Stresses, 8mm Thick Al Plate, 20% Fy Uniaxial Applied Stress, Radial Displacement and Integral Methods 83
Figure 54: Cartesian Stresses, 8mm Thick Ti Plate, Radial Displacement and Integral Methods 84
Figure 55: Average Cartesian Stresses, 8mm Thick Ti Plate, Radial Displacement and Integral Methods 84
Figure 56: Cartesian Stresses, 12mm Thick Steel Plate, Radial Displacement and Integral Methods 85
Figure 57: Average Cartesian Stresses, 12mm Thick Steel Plate, Radial Displacement and Integral Methods 85
Figure 58: X Stress Profile Comparison, Out of Plane 4-pt Bending 86
Figure 59: XY Stress Profile Comparison, Out of Plane 4-pt Bending 86
Figure 60: Y Stress Profile Comparison, Out of Plane 4-pt Bending 87
Figure 61: Minimum Stress Profile Comparison, Out of Plane 4-pt Bending 87
Figure 62: X Stress Profile Comparison, In Plane 4-pt Bending 88
Figure 63: XY Stress Profile Comparison, In Plane 4-pt Bending 88

Figure 64: Y Stress Profile Comparison, In Plane 4-pt Bending 89
Figure 65: Minimum Stress Profile Comparison, In Plane 4-pt Bending 89
Figure 66: RMS Error, FE Cartesian Stress Results 90
Figure 67: XRD Radial Plug Measurement d-spacing Sin^2 X linear at ¼ Radial Distance off Center 91
Figure 68: XRD Radial Plug Measurement d-spacing Sin^2 X linear at -¼ Radial Distance off Center 92
Figure 69: XRD Radial Ring Measurement d-spacing Sin^2 X linear at ¾ Radial Distance off Center 92
Figure 70: XRD Radial Ring Measurement d-spacing Sin^2 X linear at -¾ Radial Distance off Center 93
Figure 71: XRD Hoop Plug Measurement d-spacing Sin^2 X linear at ¼ Radial Distance off Center 93
Figure 72: XRD Hoop Plug Measurement d-spacing Sin^2 X linear at -¼ Radial Distance off Center 94
Figure 73: XRD Hoop Ring Measurement d-spacing Sin^2 X linear at ¾ Radial Distance off Center 94
Figure 74: XRD Hoop Ring Measurement d-spacing Sin^2 X linear at ¾ Radial Distance off Center 95

CHAPTER ONE

RESIDUAL STRESS MEASUREMENTS IN ALLOYS USING HOLE DRILLING METHOD INTEGRATING 3-D DIGITAL IMAGE CORRELATION AND FINITE ELEMENT METHOD

Abstract

Residual stresses within an alloy result from complex processes associated with additive and subtractive manufacturing, extrusion, casting, machining, and welding due to thermo-mechanical loading. While mesoscopic (Type II) and microscopic residual stresses (Type III) are of academic interest, Type I bulk residual stresses are of primary importance for engineering applications and is addressed in this study by improving ASTM approved hole drilling procedure enhanced with integrating three-dimensional Digital Image Correlation (DIC) technique. The precise hole drilling positioning and advancement at high spindle rate was implemented using a custom developed CNC drill integrated with DIC cameras with suitable optics to realize high spatial resolution. The methodology was validated by comparing the results with strain gage rosette-based measurement and data inversion using analytical models currently approved in existing standards. Significant effort was invested in evaluating the suitability advantages of hole drilling method with DIC using in situ loading in a four-point flexure and results compared with expected data from traditional mechanics of materials approach. An alternative method with improved accuracy was developed using radial displacement contour method with inverse Finite Element Method results for directly relating the residual stress tensor with radial displacement vector. Novel solution is proposed for isolating the relative role of normal and shear stresses on the radial displacement method and sensitivity of inferred results are identified.

Introduction

Materials in cyclical use have more potential for residual stress development than extruded materials. Additive manufactured materials are of high importance for residual stress measurement due to their unique stress development during manufacturing and post-processing [1]. Residual stress also poses a threat to essential elements of infrastructure, aviation, and automotive industries [2]. From a structural engineering standpoint, residual stress measurement is critical for structural steel elements and connections [3]. The residual stress effects mentioned prior are of Type I and are therefore known to vary throughout an affected part [4]. The hole drilling method of

measuring residual stresses with strain gauge rosettes is outlined in ASTM E837 [5]. Preparing a sample for residual stress measurement with strain gauge rosettes requires precise orientation of the rosette, a delicate bonding procedure, and wire soldering [2]. Soldering wires to the rosettes proves to be a difficult and time-consuming process due to the delicate nature and single measurement use of strain gauges. The three-dimensional digital image correlation (3D DIC) method is applied to the hole drilling method to simplify sample preparation, improve measurement speed, and allow for a broader area of inspection around the drilled hole. Sample preparation for DIC measurement requires applying a painted, stochastic speckle pattern to the sample. Once the speckle pattern is applied, hole drilling measurements can be made at any point of interest on the sample. Measurement with 3D DIC allows for residual stress determination using the integral method and using radial displacements at specified distances from the center of the drilled hole [6], [7].

Blind hole drilling is one of the most commonly used methods for measuring residual stress. Drilling a small hole into a part allows for structural integrity to remain intact, therefore making the method semi-destructive [8]. Plasticity can be induced by hole drilling when residual stresses are on the order of 60% of the yield stress [9]. The effects of plasticity are not investigated in this study, but the consideration of plasticity in DIC hole drilling residual stress measurement is encouraged for future work. Here, a hole diameter of 2mm is used with material removed in 50 micron increments to a final depth of 1mm. As material is removed incrementally, strain relaxation in the area around the hole is on the order of the residual stress within the part [6]. Conventionally, strains are collected after each drill increment, or drill step, and are used with the integral method to determine the residual stress within the part. This method is applicable to linearly elastic materials in which stresses remain relatively constant across the drilled hole diameter. ASTM E837-20 outlines the integral method of calculating residual stress as well as standardized strain gauge rosettes [5]. Strain gauge rosettes for hole drilling are comprised of three linear strain gauges oriented at 0°, 45°, and 90° around a center space for the drilled hole, an idea which was proposed by Rendler and Vigness for non-

incremental hole drilling [10]. The size of the strain gauges and their distance from the hole center is predetermined in the ASTM based on the diameter of the drilled hole. Data collected with 3D DIC can also be directly applied to the integral method of residual stress measurement by replicating the size and shape of the standard strain gauges [7].

Optical techniques such as 3D DIC have gained popularity in the hole drilling residual stress community because they offer the advantage of providing larger areas of measurement in comparison to strain gauges [11]. With 3D DIC the user gains the ability to easily define the desired orientation of measurements around the drilled hole, which is advantageous compared to the manual process of alignment required with conventional strain gauge rosettes. Using optical techniques, residual stresses can be calculated from measured radial displacements at specified radial distances from the center of the drilled hole. This allows the user to take advantage of the large amount of collected data associated with DIC measurements [6]. Previous work by Nelson provides calibration coefficient data for use in single drill blind hole drilling experiments [12]. To expand on this work, calibration coefficients for each 50 micron drilling increment up to a final depth of 1mm for a 2mm diameter hole have been determined. Along with these coefficients, analysis of the method for aluminum, steel, and titanium finite element models are performed to provide guidance for material specific use. The integral method is performed for the various material models to provide direct comparisons.

In the current study, three-dimensional digital image correlation (3D DIC) was applied to the incremental hole drilling procedure in place of strain gauge rosettes. Incremental hole drilling allows for measurements of non-uniform stress through the cross section of the material [13]. An extensive finite element analysis was conducted to determine required calibration coefficients for use in the radial displacement method of calculating residual stresses with 3D DIC [6]. 3D DIC offers many advantages for sample preparation and also allows for data collection over a larger area. Calculation errors like hole eccentricity and gauge orientation that are common with strain gauge rosettes are removed with use of 3D DIC [8]. In comparison to other optical techniques, DIC has less errors associated

with vibrational and environmental noises, making it more suitable for in-shop measurements [14]. Two-dimensional digital image correlation can be applied to the hole drilling method as well but has limitations with out of plane movement. 3D DIC allows for limited out of plane movement which can preserve measurements between drilling increments and is advantageous for samples with unique geometries [6].

Materials and Methods

Finite Element Analysis

Finite element analyses were conducted to determine required calibration coefficients for the development of the 3D DIC radial displacement method of calculating residual stresses for incremental hole drilling. Radial displacements associated with stress relief measured with incremental blind hole drilling can be communicated in terms of the components of residual stress, σ_x, σ_y, and τ_{xy} [6],

$$u_r = \big(A + Bcos(2\theta)\big)\sigma_x + \big(A - Bcos(2\theta)\big)\sigma_y + (2Bsin(2\theta))\tau_{xy} \qquad Eqn\ 1.1$$

Where, $A = r_0(1+\nu)a/2E$, $B = r_0 b/2E$, r_0 = hole radius, ν = Poisson's ratio, E = elastic modulus, θ is the angle from the pre-defined X direction, and a & b are the coefficients derived from the presented finite element analysis. Equation 1 is valid for materials with linear elastic and isotropic behavior [6]. Calibration coefficients are determined here for an applied uniaxial stress that is constant with the hole depth; however, these coefficients can be applied to materials with stresses that vary throughout the cross section of the material. A set of coefficients a & b are found for each step depth in the incremental hole drilling process, resulting in 20 sets of coefficients. As proposed by Nelson, a linear system of equations can be produced to solve for the components of residual stress, σ_x, σ_y, and τ_{xy} [6]. Radial displacements, u_r, can be obtained as a function of θ at a prescribed radial distance from the hole center. Through this thought process, equation 1 can be considered as a function of angle, θ_i, which has n experimentally determined values of u_{ri} around the drilled hole:

$$u_{ri} = \left(A + Bcos(2\theta_i)\right)\sigma_x + \left(A - Bcos(2\theta_i)\right)\sigma_y + (2Bsin(2\theta_i))\tau_{xy} \qquad \textit{Eqn 1.2}$$

To successfully determine coefficients a & b, equation 2 can be reorganized to the following form in equation 3, where A & B can be solved by using a least squares solution [15]:

$$\boldsymbol{u = Mc} \qquad \textit{Eqn 1.3}$$

$$\begin{bmatrix} u_{r1} \\ u_{r2} \\ \cdots \\ u_{rn} \end{bmatrix} = \begin{bmatrix} (\sigma_x + \sigma_y) & \left(\sigma_x - \sigma_y\right)cos(2\theta_1) + 2Bsin(2\theta_1)\tau_{xy} \\ (\sigma_x + \sigma_y) & \left(\sigma_x - \sigma_y\right)cos(2\theta_2) + 2Bsin(2\theta_2)\tau_{xy} \\ \cdots & \cdots \\ (\sigma_x + \sigma_y) & \left(\sigma_x - \sigma_y\right)cos(2\theta_n) + 2Bsin(2\theta_n)\tau_{xy} \end{bmatrix} \begin{bmatrix} A \\ B \end{bmatrix} \qquad \textit{Eqn 1.4}$$

Coefficients A & B are material dependent and therefore must be determined from separate analyses for different materials. Coefficients a & b are independent of material properties but are dependent on the hole depth to diameter ratio [12]. Once the coefficients are resolved for the required material, residual stress components can be determined as [6]:

$$\boldsymbol{u = Ks} \qquad \textit{Eqn 1.5}$$

$$\begin{bmatrix} u_{r1} \\ u_{r2} \\ \cdots \\ u_{rn} \end{bmatrix} = \begin{bmatrix} A + Bcos(2\theta_1) & A - Bcos(2\theta_1) & 2Bsin(2\theta_1) \\ A + Bcos(2\theta_2) & A - Bcos(2\theta_2) & 2Bsin(2\theta_2) \\ \cdots & \cdots & \cdots \\ A + Bcos(2\theta_n) & A - Bcos(2\theta_n) & 2Bsin(2\theta_n) \end{bmatrix} \begin{bmatrix} \sigma_x \\ \sigma_y \\ \tau_{xy} \end{bmatrix} \qquad \textit{Eqn 1.6}$$

The finite element models were created in Abaqus finite element software [16]. A quarter of a 20 x 20 x 8mm plate was modeled due to the symmetric nature of the problem. Various plate depths were used to simulate plane strain and plane stress loading conditions. The model was comprised of C3D8R elements provided in the Abaqus software. The meshes used for radial displacement and integral method analyses are provided below in Figure 1 and Figure 2, respectively. Aluminum, steel, and titanium models were created to provide useful coefficients for a range of industries. For each model, uniaxial stresses in 20% increments of material yield stress were applied to plates of various depths. A biaxial stress state was also evaluated to confirm application to different stress states.

3D DIC Camera Setup

Two 12-megapixel optical cameras were used to collect data for 3D DIC measurements. The cameras provide 4096 x 3000-pixel resolution, with a pixel size corresponding to 6.10 micron. 100 mm focal length lenses were used with 50 mm extenders. The area in measurement view was 25 x 15 mm. To allow for maximum data processing, 15 DIC images were taken for each measurement. DIC images were collected and analyzed in Aramis Professional 2020 software [17]. An image collection rate of 2 Hz is used to decrease time during the measurement. Calibration deviations below 0.04 were accepted to ensure data quality. For all data collection in Aramis, a facet size of 50 pixels was used with a point distance of 25 pixels, corresponding to the size of the applied speckle pattern. The point distance of 25 pixels allows for full overlap which increases the computational accuracy of calculated strains and displacements. Aramis software allows for a maximum intersection deviation of 0.3 pixels, corresponding to 1.8 micron for the proposed setup. The displacement noise floor for the following experiments had a maximum displacement of 0.034 microns, which is less than the maximum allowable deviation. Based on this assessment, displacements larger than 0.034 microns are measurable with the proposed DIC measurement setup.

4-point Bending Validation

Two 4-point bending load fixtures were designed to verify use of DIC for hole drilling residual stress measurements. Placing a sample in 4-point bending creates a state of temporary residual stress and allows collected data to be verified by an expected or applied stress. This method has been utilized by Arabul and Lunt to verify their respective 2D DIC system [7]. The first loading fixture shown in Figure 3 loads the sample out of plane with measurements locations indicated by arrows. This loading fixture is advantageous because it allows for measurement over an area with constant stress; However, it does not allow for compressive measurements. The second loading fixture presented in Figure 4 was designed to bend the sample in plane and therefore allows for both tensile and compressive measurements. With the in-plane loading fixture,

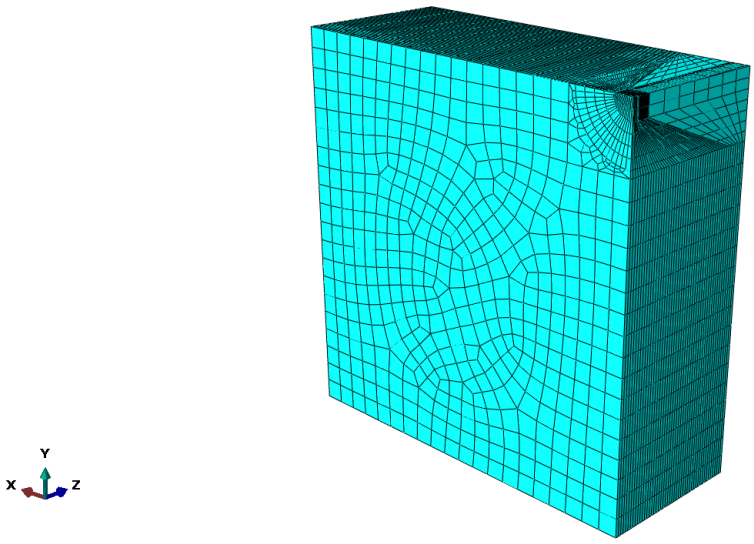


Figure 1: Finite Element Mesh for Radial Displacement Analysis, 20x20x8mm Plate

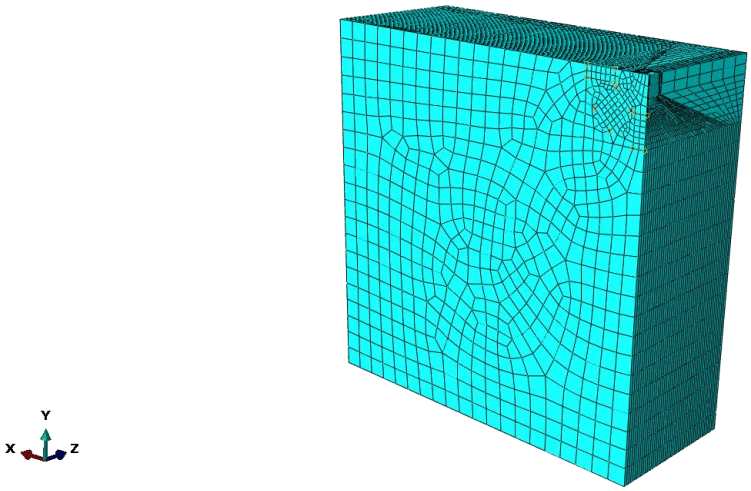


Figure 2: Finite Element Mesh for Integral Method Analysis, 20x20x8mm Plate

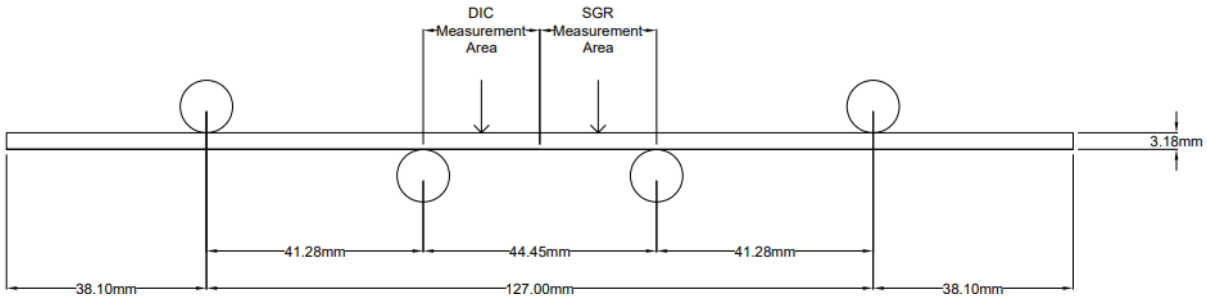


Figure 3: Out of Plane 4-Point Bending Fixture

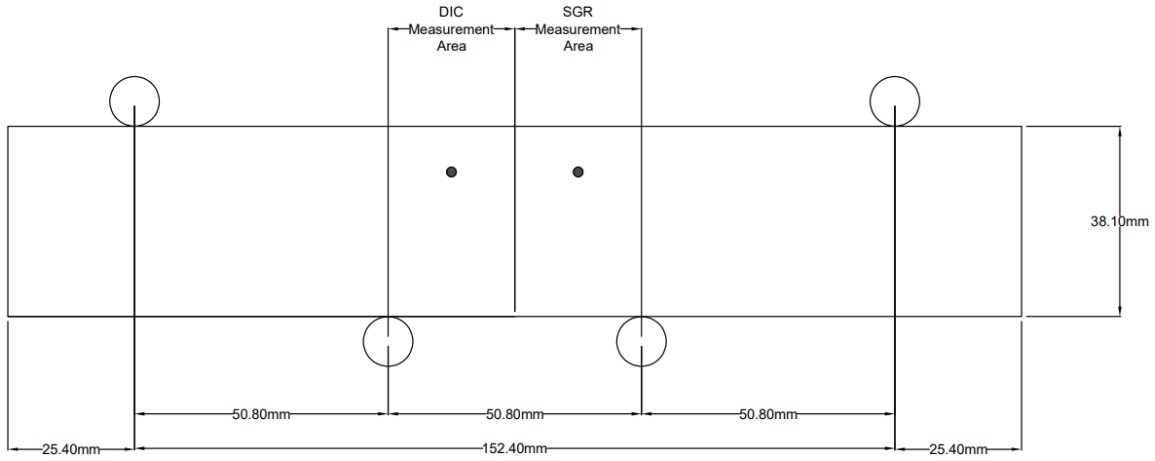


Figure 4: In Plane 4-Point Bending Fixture

the applied strain varies along the measurement area. The measurements were taken at the marked locations in Figure 4. The applied load from both fixtures is measured by a load cell. Data from the load cell and strain gauges is collected with a Micro Measurements System 8000, where data is recorded in Strain Smart software [18].

4-point bending is utilized here to directly compare DIC to strain gauge rosette measurements. For 4-point bending verification tests, the sample is prepared by applying a stochastic speckled pattern to areas of DIC measurement. Strain gauge rosettes of type CEA-06-062UL-120 are applied to corresponding areas and prepared by manufacturer's instructions. Both DIC and strain gauge measurements are performed within the pure moment region of the 4-point bending fixture. Reference DIC and strain gauge measurements are taken prior to loading for the in plane fixture. Then, the sample is loaded incrementally to the desired applied stress. Note that for DIC, it is advantageous to take a few measurements while loading incrementally to allow the software to accurately account for deformations. For the out of plane fixture, reference DIC measurements are taken after the sample is loaded and strain gauge rosette reference measurements are taken prior to loading. Once the sample is loaded, the drilling sequence is initiated. Drilling is completed with a desktop CNC machine. The sample moves from the DIC viewing area, represented in Figure 5, to the drilling area. The spindle is stopped after the drilling to decrease the electronic interference between itself and the load cell. After drilling, the sample moves back to the DIC viewing area, and this sequence is repeated until the desired depth of 1mm is reached. After each drill step, 15 DIC images are collected at a rate of 2 Hz. For strain gauge testing, the applied load remains, and the strain gauge is drilled incrementally. The spindle is stopped for 30 seconds after drilling to once again decrease the electronic interference between the spindle, load cell, and strain gauges. This sequence is repeated until the desired depth of 1mm is reached.

3D DIC Data Filtering

Spatial and temporal filters in Aramis software are used to minimize noise from DIC measurements. Use of these filters also acts as minimal rigid body compensation. Since

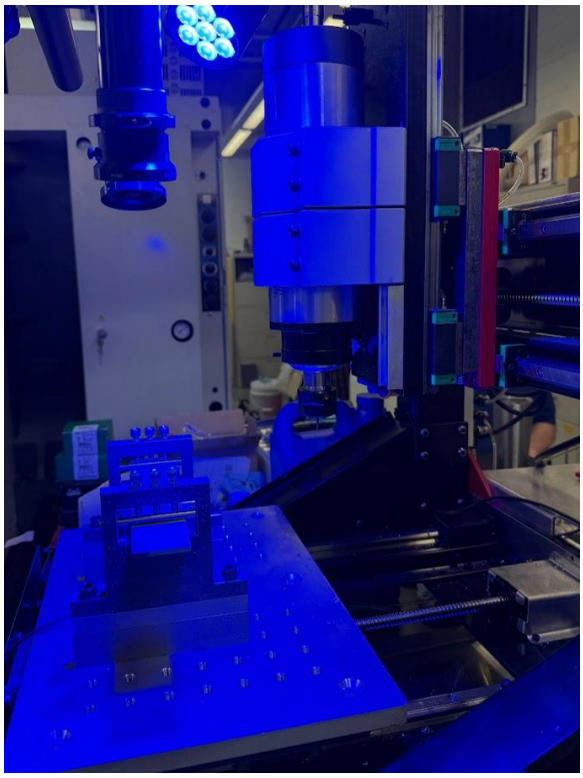


Figure 5: DIC Viewing Area

there is not a point in the DIC image which remains at a constant location, other rigid body compensation tactics were not applicable. Spatial average filtering allows you to average strains over multiple points of the surface component to reduce the influence of outlying data points that arise from the limited DIC view. Based on the filter size, n, strains are averaged over n number of points in the neighborhood of the initial measurement point. A visual representation of a spatial average filter value of 1 is provided in Figure 6. Temporal average filters take strains from neighboring images into account. Since 15 images are taken for each measurement here, a temporal average filter value of seven is applied to calculated strains. Use of the temporal average filter then allows the strains to be average over seven images before and after, allowing the eighth image in the sequence to be used as the measured and filtered data. Use of spatial and temporal average filters ensures noise reduction and performs minimal rigid body motion compensation.

Integral Method Analyses

Pseudo strain gauges are created in Aramis professional 2020 by selecting regions within the correlated measurement area, commonly known in Aramis as the surface component [17]. Pseudo gauges, or DIC gauges, were modeled after micro measurements CEA-06-062UL-120 strain gauge rosettes, following the ASTM E837 standard for a 2mm hole diameter. Due to increased measurement area, eight individual strain gauges can be mapped and placed around the hole area as shown in Figure 7. From these eight pseudo strain gauges, assemblies of eight strain gauge rosettes can be created and used for residual stress calculations, represented in Table 1.

Residual stress calculations from measured DIC and strain gauge data are performed using H-Drill software. H-Drill applies the integral method as outlined in ASTM E837-20 and provides stress values between each incremental step depth, up to 1mm for the purpose of this work [19]. Residual stress final results are taken as the average of the calculated stresses over the depth into the part. For DIC measurements, the average of integral method results for select rosette assemblies is taken as the final result. DIC

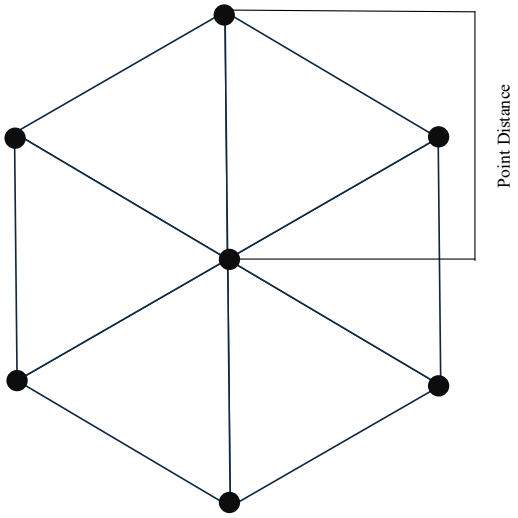


Figure 6: Spatial Average Filter Schematic

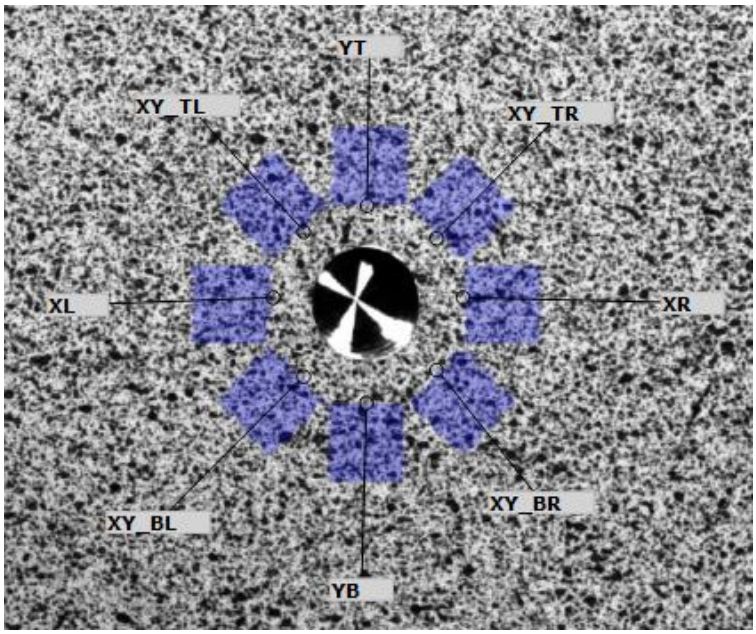


Figure 7: DIC Pseudo Gauges

Table 1: DIC Rosette Assemblies

Rosette	Orientation	G1	G2	G3
1	CW	XR	XYBR	YB
2	CW	XR	XYTL	YB
3	CW	XL	XYTL	YT
4	CW	XL	XYBR	YT
5	CCW	XR	XYTR	YT
6	CCW	XR	XYBL	YT
7	CCW	XL	XYBL	YB
8	CCW	XL	XYTR	YB

rosette assemblies are chosen based on the smoothness of the pseudo gauge strain profiles.

3D DIC Radial Displacement Method Analysis

Displacements at radial distances from the hole center are determined in Aramis by creating surface curves from individual points on the surface component. The displacements are calculated in Aramis software with spatial average and temporal average filter values of 10 and 7 respectively. The radius of each curve is expressed by the ratio of the curve radius, r, to the radius of the drilled hole, r_0. Calibration coefficients for each r-r0 curve are used to calculate the applied stress using previously defined equations.

Results

Finite Element Analysis

Finite element models were used to obtain calibration coefficients, a & b, at hole depths for incremental hole drilling of a 2mm diameter hole to a final depth of 1mm. The incremental steps of 50 micron are the same as those outlined in ASTM E837 for application to the integral method. The coefficients were derived from a model of a 20 x 20 x 10mm aluminum plate, with an applied uniaxial stress of 276 MPa: equal to the material's yield stress. A depth of 10mm was chosen for general use to simulate a loading condition between plane stress and plane strain. Coefficients derived from models with plate depths of 4mm, 15mm, 20mm and 30mm are provided in the appendix for more specific application. Deriving calibration coefficients from a model with high applied stress is advantageous to get high quality results from recorded radial displacements. Four different radial distances from the hole center were used here and the coefficients were obtained using previously defined equations. The resulting a & b coefficients are provided in Table 2 and Table 3 below. With these coefficients, a stress profile against the depth into material can be constructed for direct comparison to the integral method.

Uniaxial Stress values in increments of 20% of yield stress were performed to evaluate the accuracy of the coefficients derived from the 100% yield stress model. Several plate thicknesses were also evaluated during modeling. For each increment, the appropriate a & b coefficients for the plate depth were used to calculate the applied uniaxial stress. The stress profile results for the applied uniaxial stress of 80% yield stress for an 8mm thick aluminum plate are shown below in Figure 8; the averages of the stress profiles over the 1mm depth into the plate are provided in Figure 9. The stress profile and average stress results of an applied 20% yield stress for an 8mm thick aluminum plate are presented in Figure 10 and Figure 11. The standard integral method outlined in ASTM E837 was also evaluated for finite element models for direct comparison to the proposed finite element radial displacement method of calculating residual stress. Cartesian stress profiles and average results are provided in the appendix.

As previously mentioned, derived coefficients a and b are independent of material properties. Steel and titanium finite element models were created, and the resulting radial displacements were used with a & b coefficients derived from a 10mm thick aluminum model to calculate applied stress. The integral method results are included for comparison. A uniaxial stress of 60% yield was applied to the 8mm thick titanium plate. The results for the 8mm thick titanium plate are provided in Figure 12 and Figure 13. For the steel plate, a biaxial stress of 40% yield in the X direction and 20% yield in the Y direction was applied. The results for the 12mm thick steel plate are shown in Figure 14 and Figure 15.

Finite element analyses were performed on 8mm thick aluminum, steel, and titanium plates for applied uniaxial loads in increments of 20% of the yield stress to evaluate the magnitude of the radial displacements resulting from incremental hole drilling. The radial displacements for thetas 0, 45, and 90 degrees for each incremental hole depth are shown

Table 2: a Values for IHD Depths, 2.0mm Diameter Hole, 10mm Thick Plate

a Values, 20x20x10mm Plate				
Depth (mm)	1.5 r/r_0	2.0 r/r_0	2.5 r/r_0	3.0 r/r_0
0.05	0.014994	0.007375	0.012603	0.001523
0.1	0.056935	0.017634	0.017798	0.009617
0.15	0.11025	0.040703	0.025682	0.016906
0.2	0.149745	0.064672	0.036482	0.023788
0.25	0.190625	0.092278	0.051583	0.032991
0.3	0.223043	0.115649	0.06595	0.04202
0.35	0.255824	0.140486	0.08265	0.053004
0.4	0.281718	0.160819	0.097138	0.062956
0.45	0.307928	0.182061	0.113034	0.07435
0.5	0.328699	0.199298	0.126386	0.084257
0.55	0.349853	0.217242	0.140734	0.095249
0.6	0.366685	0.231763	0.152624	0.104593
0.65	0.38366	0.246673	0.165147	0.114701
0.7	0.397405	0.25888	0.175562	0.123258
0.75	0.411713	0.271732	0.186706	0.132577
0.8	0.423264	0.282203	0.195905	0.140385
0.85	0.435297	0.293216	0.205707	0.148827
0.9	0.445021	0.302183	0.213773	0.155855
0.95	0.455157	0.311595	0.222321	0.163378
1	0.462534	0.318553	0.228751	0.169139

Table 3: b Values for IHD Depths, 2.0mm Diameter Hole, 10mm Thick Plate

b Values, 20x20x10mm Plate				
Depth (mm)	1.5 r/r_0	2.0 r/r_0	2.5 r/r_0	3.0 r/r_0
0.05	0.036617	0.021611	0.024662	0.005785
0.1	0.113578	0.043342	0.039279	0.022245
0.15	0.215502	0.087849	0.057426	0.038624
0.2	0.295304	0.135761	0.080016	0.053744
0.25	0.38181	0.192831	0.11146	0.073392
0.3	0.45342	0.242958	0.141849	0.092624
0.35	0.528888	0.298276	0.178087	0.116311
0.4	0.590781	0.345124	0.210347	0.138118
0.45	0.655843	0.395798	0.246781	0.163613
0.5	0.709136	0.438172	0.278177	0.186216
0.55	0.765342	0.483722	0.312864	0.21187
0.6	0.811412	0.521589	0.342305	0.234104
0.65	0.859649	0.561827	0.374244	0.258764
0.7	0.899652	0.595498	0.401341	0.279995
0.75	0.94249	0.631896	0.431019	0.303594
0.8	0.977871	0.662185	0.455994	0.323697
0.85	1.015837	0.694924	0.483273	0.345918
0.9	1.047266	0.722192	0.506195	0.364772
0.95	1.081063	0.751688	0.531201	0.38553
1	1.107695	0.775123	0.551262	0.402375

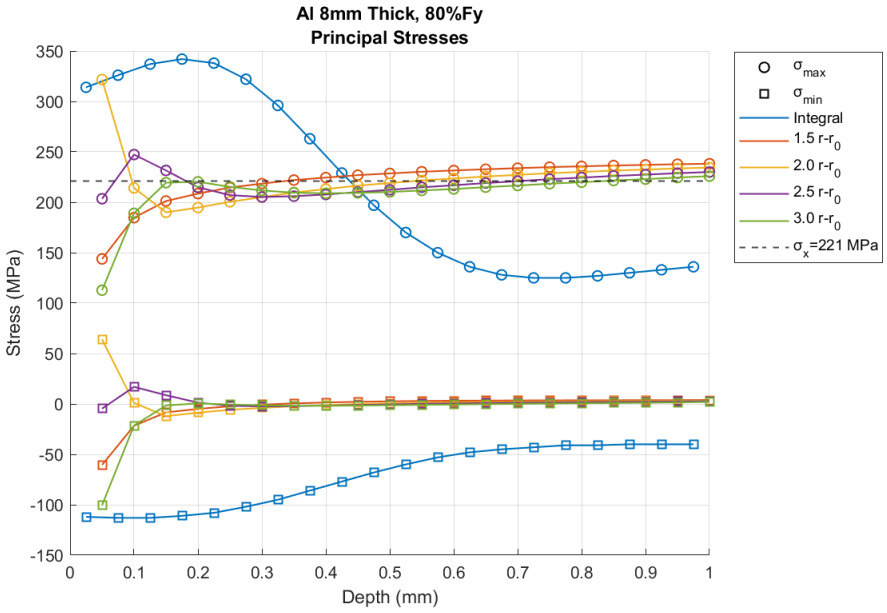


Figure 8: Principal Stresses, 8mm Thick Al Plate, 80% Fy Uniaxial Applied Stress, Radial Displacement and Integral Methods

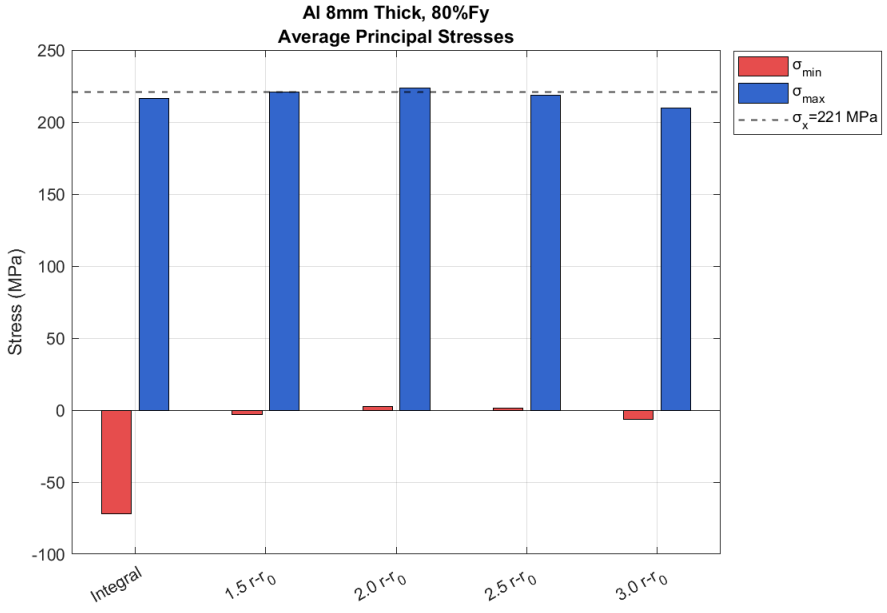


Figure 9: Average Principal Stresses, 8mm Thick Al Plate, 80% Fy Uniaxial Applied Stress, Radial Displacement and Integral Methods

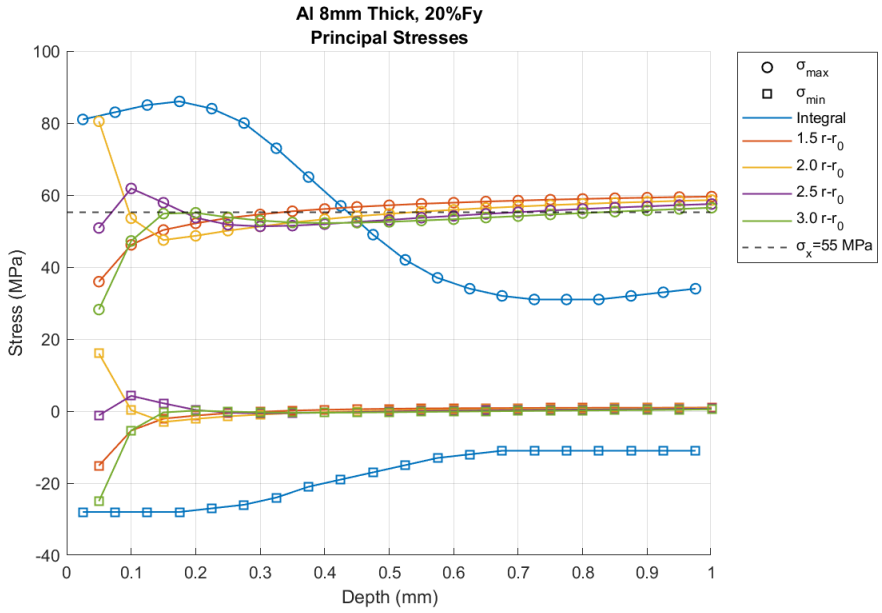


Figure 10: Principal Stresses, 8mm Thick Al Plate, 20% Fy Uniaxial Applied Stress, Radial Displacement and Integral Methods

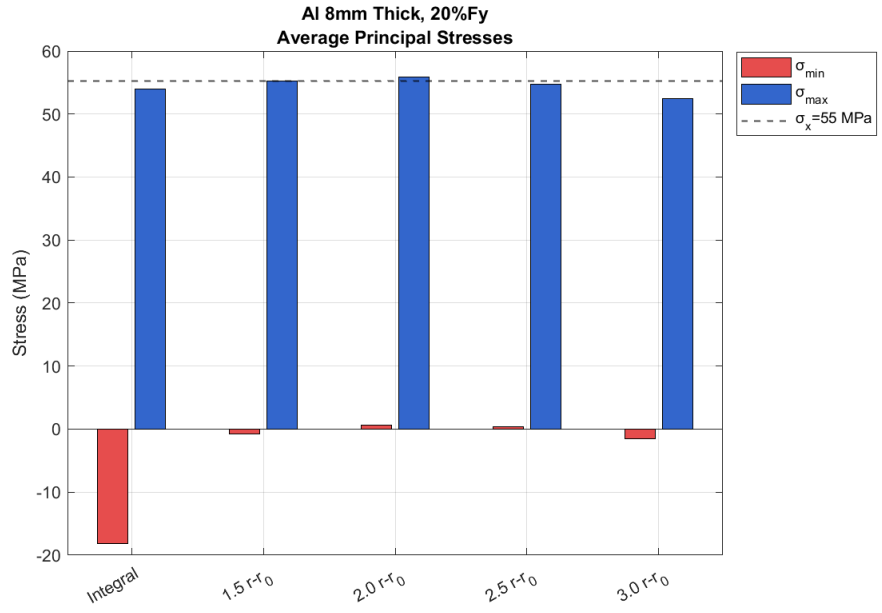


Figure 11: Principal Stresses, 8mm Thick Al Plate, 20% Fy Uniaxial Applied Stress, Radial Displacement and Integral Methods

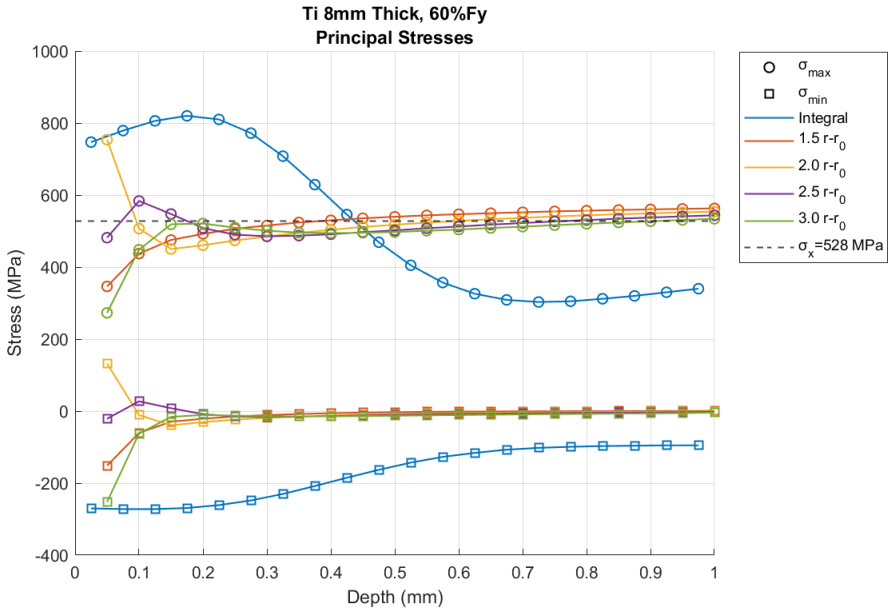


Figure 12: Principal Stresses, 8mm Thick Ti Plate, Radial Displacement and Integral Methods

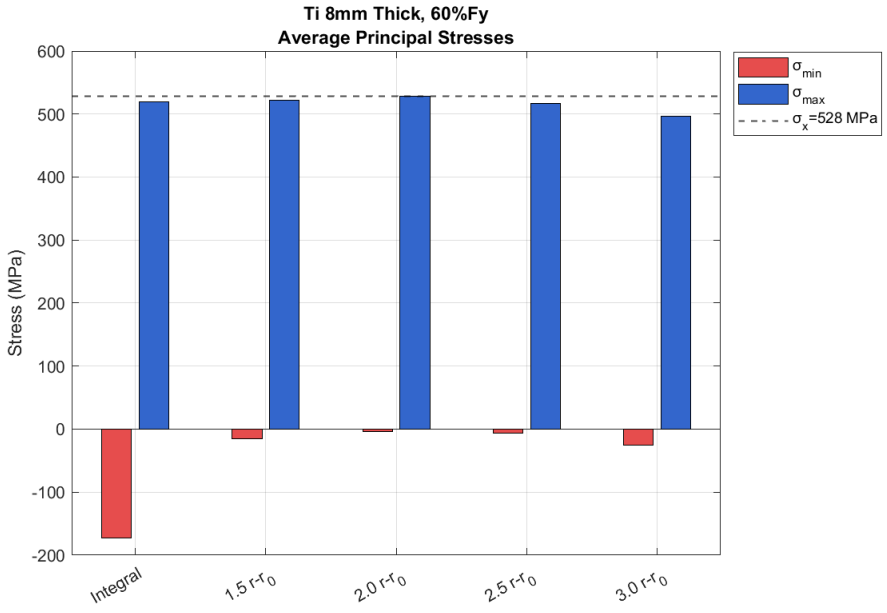


Figure 13: Average Principal Stresses, 8mm Thick Ti Plate, Radial Displacement and Integral Methods

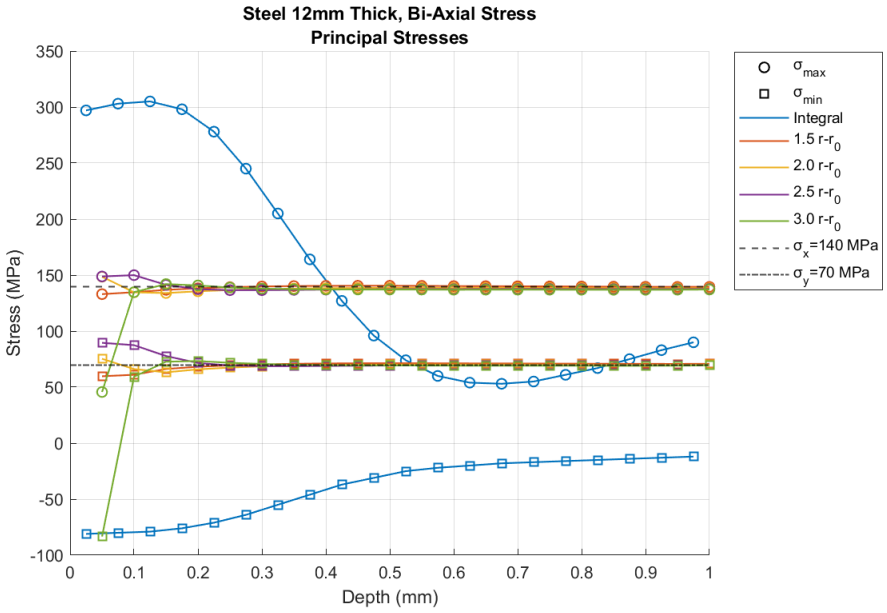


Figure 14: Principal Stresses, 12mm Thick Steel Plate, Radial Displacement and Integral Methods

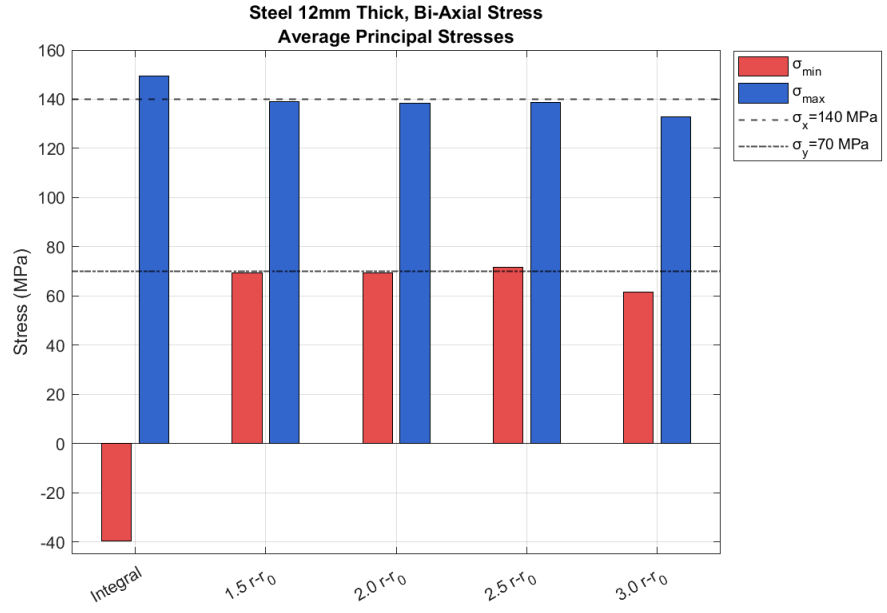


Figure 15: Average Principal Stresses, 12mm Thick Steel Plate, Radial Displacement and Integral Methods

in Figure 16, Figure 17, and Figure 18 for each evaluated material. On the figures, the plotted radial displacements are compared to the minimum displacement measurable by the DIC setup as mentioned previously. The yield stresses for aluminum, steel, and titanium were 276, 250, and 880 MPa respectively.

Out of Plane 4-Point Bending

Using the out of plate 4-point bending fixture, residual stress results from 3D DIC and a conventional strain gauge rosette were compared. The sample tested is shown below in Figure 19. The sample was loaded to a maximum bending stress of 87 MPa to generate strains and displacements of measurable magnitude. The stress is constant within the 1.0mm hole depth due to the thin plate being in a plane stress loading condition. All three methods had stresses constant with depth, supporting the plane stress behavior. Stresses before a depth of 0.275mm were not considered to preserve comparability between the radial displacement method and the integral method. For the DIC integral method results, DIC rosettes 1 and 2 were excluded because the strain profiles were not smooth. The strain gauge rosette was not drilled to the complete depth of 1.0mm; therefore, the stress result is limited to 0.875mm final depth. Maximum stress profiles at incremental hole depths are shown Figure 20, cartesian and minimum stress profiles are provided in the appendix. Average stress values for each method are compared in Figure 21 and Figure 22.

In Plane 4-Point Bending

For the in plane four point bending experiment, residual stresses calculated from a conventional strain gauge rosette, DIC pseudo rosette, and DIC radial displacements at 1.5 r-r0 are presented here. The sample was loaded to a tensile stress of 102 MPa at the locations of the drilled holes. As for the out of plane results, stresses before a depth of 0.275mm are not included in the following results to directly compare the radial displacement and integral methods. The DIC integral method results include the averages of rosettes 1, 2, 5, and 6 because the strain profiles were smooth. Maximum stress profiles are shown in Figure 23 and remaining stress profiles are provided in the

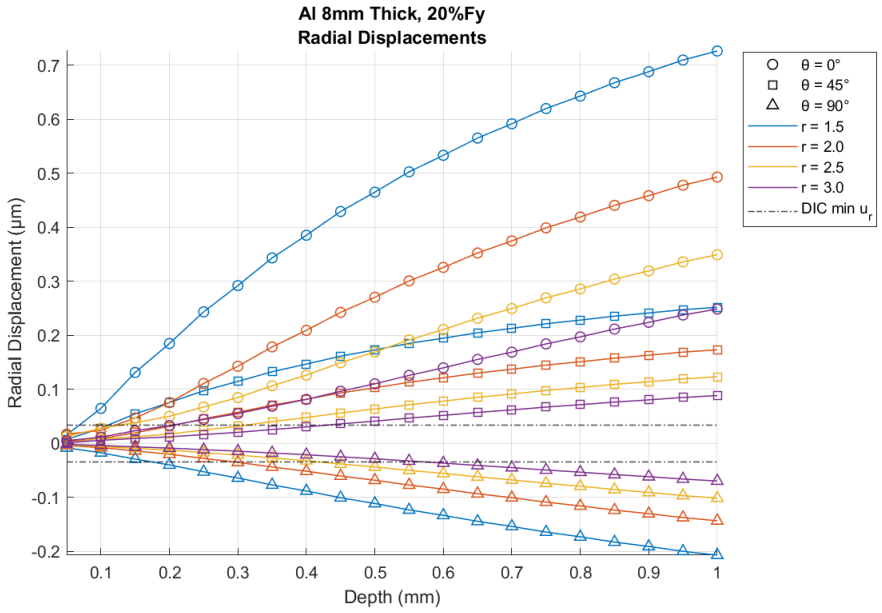


Figure 16: Al 8mm Thick Plate, 20% Fy, Radial Displacements at Select Theta vs Hole Depth

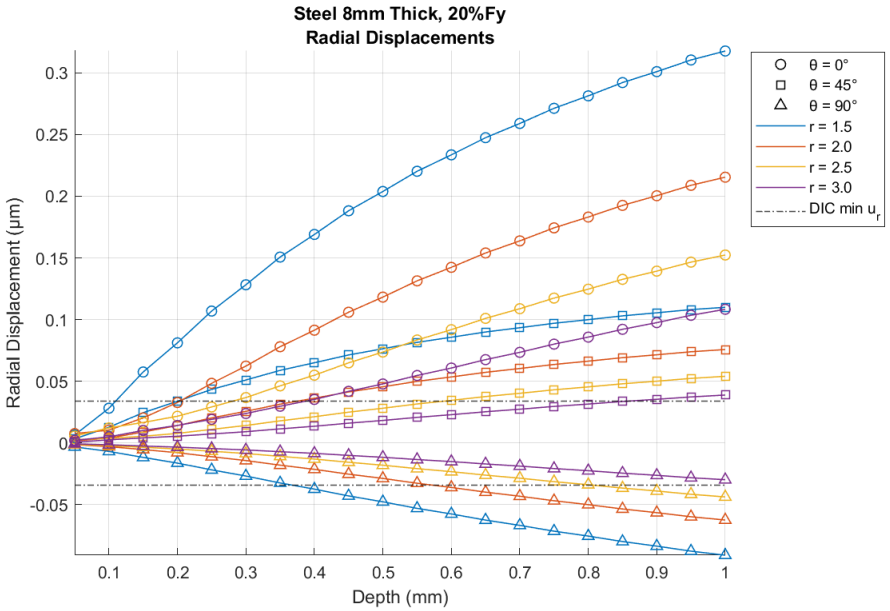


Figure 17: Steel 8mm Thick Plate, 20% Fy, Radial Displacements at Select Theta vs Hole Depth

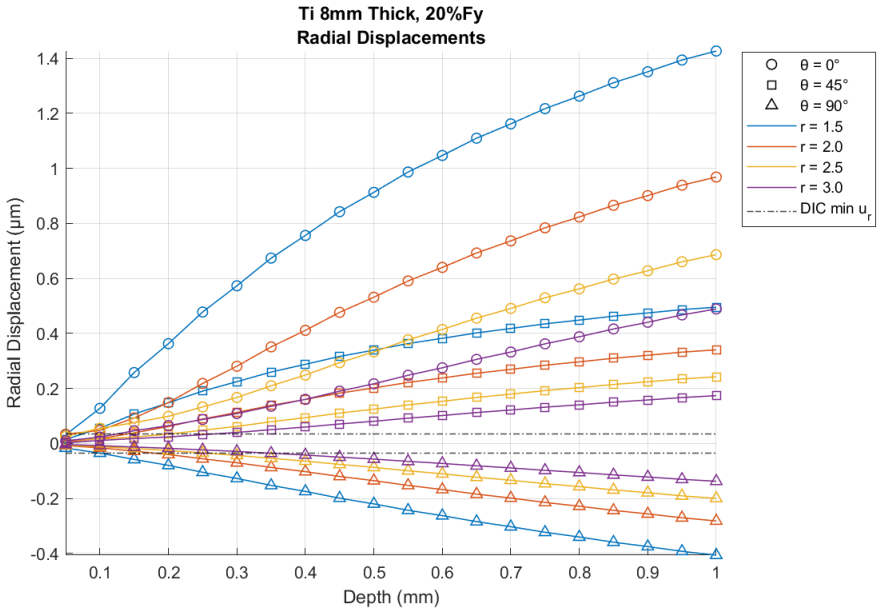


Figure 18: Ti 8mm Thick Plate, 20% Fy, Radial Displacements at Select Theta vs Hole Depth

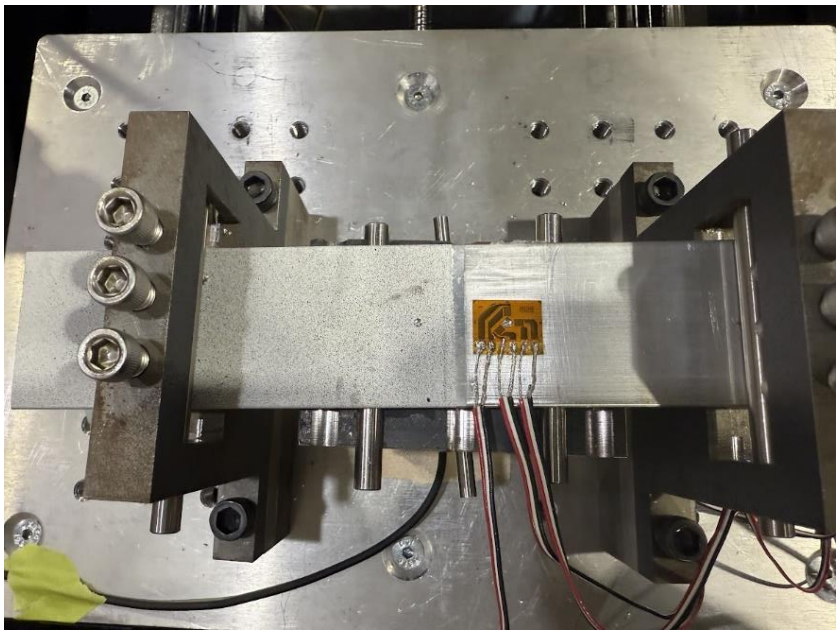


Figure 19: Out of Plane 4-Point Bending Al Sample

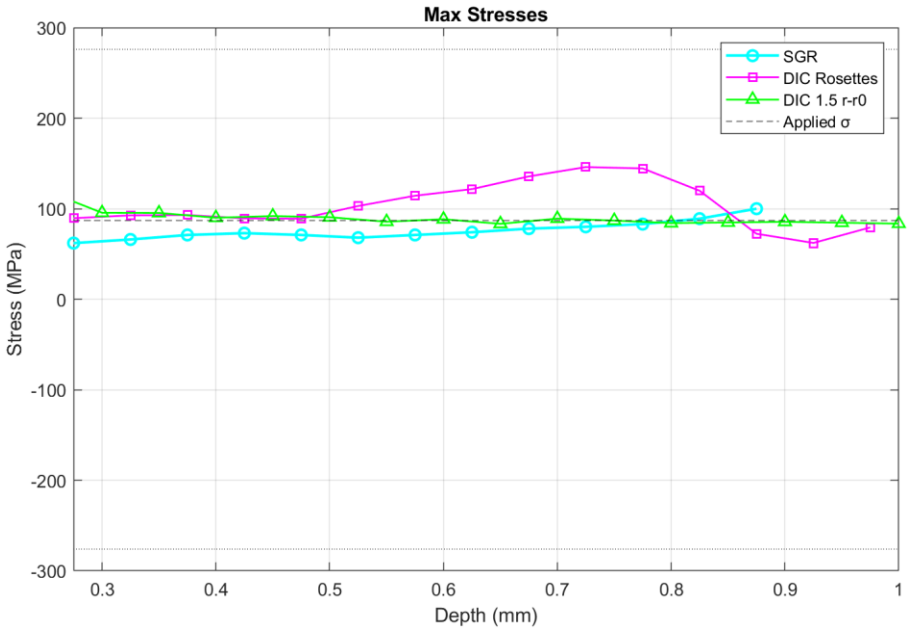


Figure 20: Max Principal Stress Profile Comparison, Out of Plane 4-pt Bending

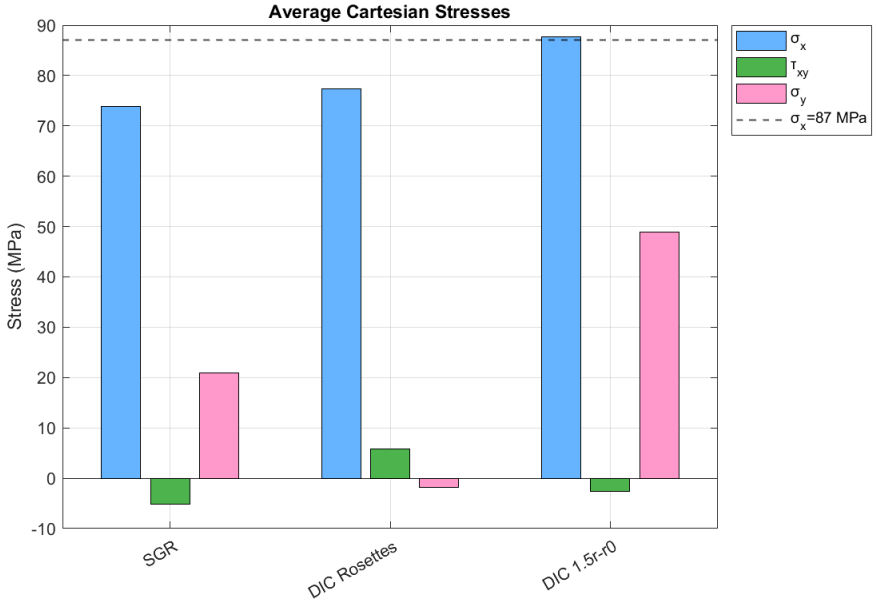


Figure 21: Average Cartesian Stress Comparison, Out of Plane 4-Point Bending

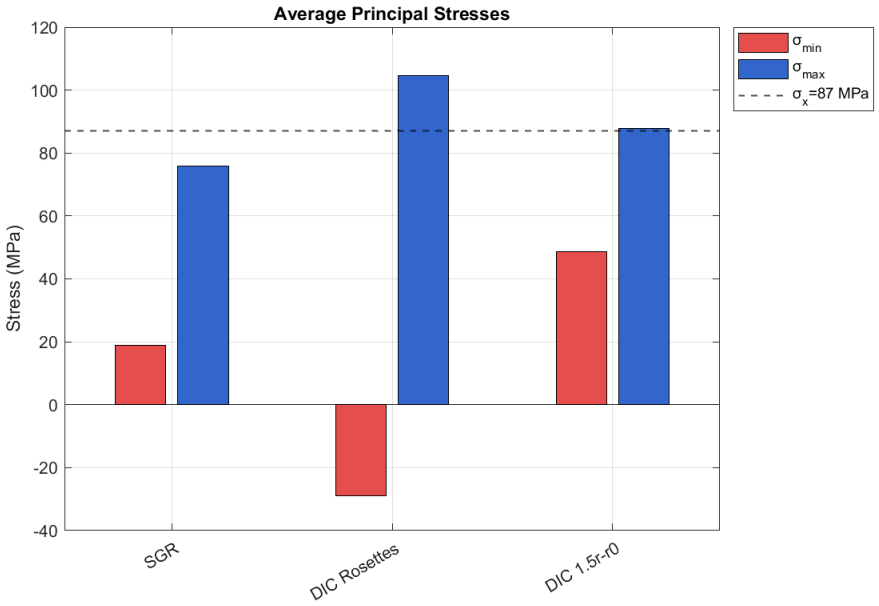


Figure 22: Average Principal Stress Comparison, Out of Plane 4-Point Bending

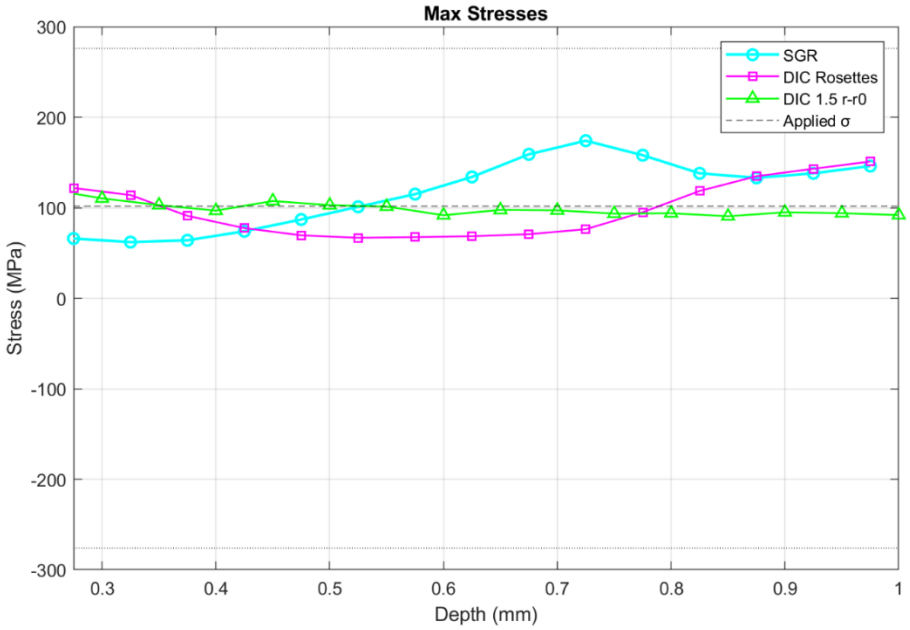


Figure 23: Max Principal Stress Profile Comparison, In Plane 4-pt Bending

appendix. The average of the stresses over the considered depth into the part are provided in Figure 24 and Figure 25.

Discussion

Finite Element Analysis

Calibration coefficients to be used in the radial displacement method of residual stress calculation for application to incremental hole drilling were successfully derived. The derived coefficients are dependent on the part depth due to plane strain and plane stress conditions. The stress results at depths less than 0.25mm are not reliable due to low and non-uniform radial displacements at those hole depths. This is not atypical for incremental hole drilling residual stress calculations. Often, stresses calculated at low hole depths using the integral method are outliers and are not included in the final analysis. It is common to use limited depths for integral method analyses, as seen in [7]. The stress results obtained at depths lower than 0.25mm with the radial displacement should not be used in final conclusions using the radial displacement method.

The 12mm thick steel model with applied biaxial stress shows the accuracy of the radial displacement method for measuring stresses in the respective X and Y directions. RMS errors are reported for the principal stresses for each calculation method in Figure 26. RMS errors for the cartesian stresses are provided in the appendix. The RMS errors are normalized by the applied stress in the X direction to make the values comparable. Although the stress values at depths below 0.25mm are unreliable, they are included in the RMS errors to provide a conservative estimate of the accuracy of the radial displacement method. The integral method stress profile did not show the uniformly applied stress and instead showed that the stress was varying with depth. The average of the integral method stresses was in good agreement with the applied stress, but the RMS error of the entire profile is in poor agreement due to the variety of stress magnitudes over the profile. Mesh refinements were performed to assess to cause of the non-uniform profile. Element sizes throughout the part were decreased and it was found that the results

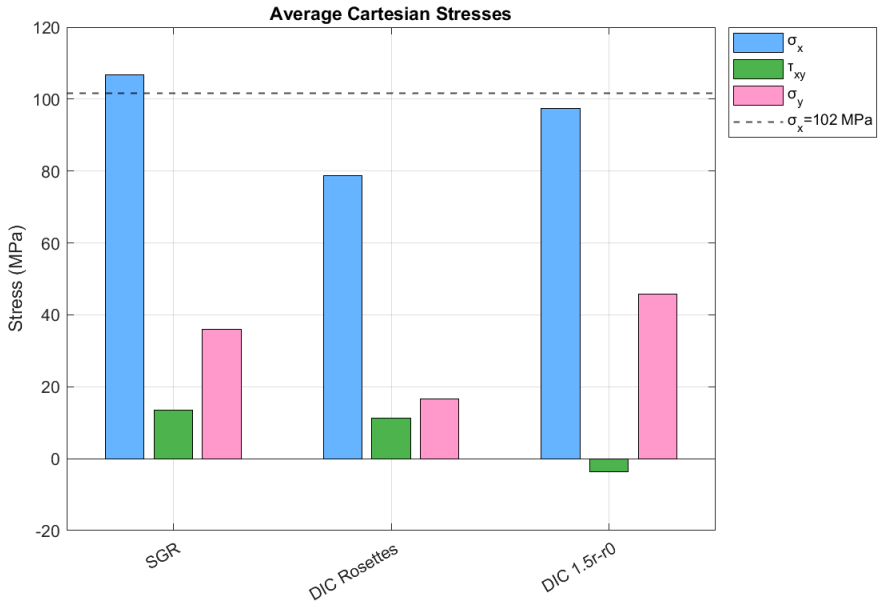


Figure 24: Average Cartesian Stress Comparison, In Plane 4-Point Bending

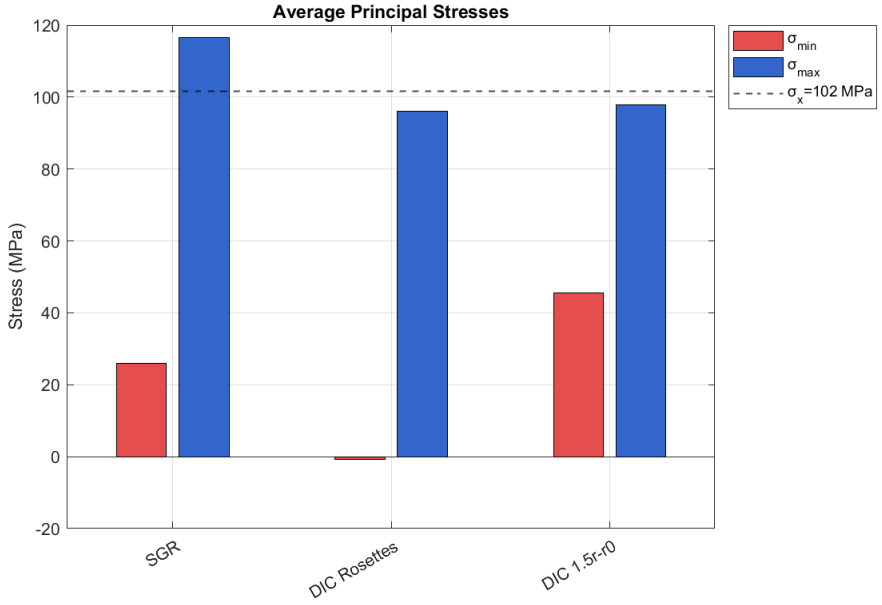


Figure 25: Average Max Principal Stress Comparison, In Plane 4-pt Bending

remained the same while keeping computation times low. The conclusion of a residual stress calculation using the integral method is usually taken as the average of the stress over the depth into the part, so the integral method performed here on the steel 12mm thick finite element model is accurate in that regard. Figure 27 shows the percentage error of the average max stress values over the depth into the part for each residual stress calculation method. The radial displacement method averages are in excellent agreement with the applied stress value, and the RMS errors are low. This amplifies the accuracy of the radial displacement method for calculating residual stress profiles using the incremental hole drilling method.

The highest RMS errors for the radial displacement method are for curve 3.0 r-r0. The stresses applied to this model were relatively low; 40% of yield in the X direction and 20% of yield in the Y direction. Displacements caused by incremental hole drilling are locationally dependent on the magnitude of residual stress present in the part. Lower stress values result in measurable displacements at smaller radial distances from the hole center. These displacements decrease as the distance from the hole center increases, making curve 3.0 r-r0 less ideal for measuring these stresses. If residuals stresses are known to be large, it is advantageous to use higher r-r0 values to calculate the residual stress. The same is true for the opposing case; if stresses are known to be small, displacements at lower r-r0 values should be used to calculate the residual stress.

Finite Element Result Application to Measurement with DIC

The resulting radial displacements for aluminum, steel, and titanium with an applied uniaxial stress of 20% of the material yield strength were compared to the minimum required displacement necessary for accurate DIC measurement. For aluminum, all displacements past the recommended depth of 0.25mm were greater than the required DIC minimum for radial distances of 1.5 r-r0. Curve 2.0 r-r0 surpasses the minimum at depths greater than 0.3mm. If residual stresses are assumed to be small in an aluminum part, radial displacements from curve 1.5 or 2.0 r-r0 should be used in calculation. For steel, radial distance 1.5 r-r0 did not exceed the DIC minimum displacement until a depth

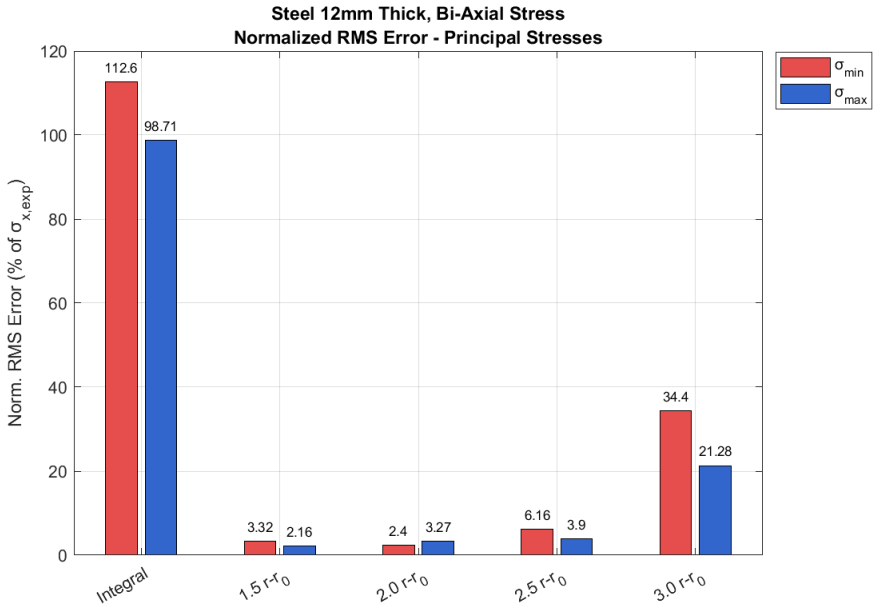


Figure 26: RMS Error, FE Principal Stress Results

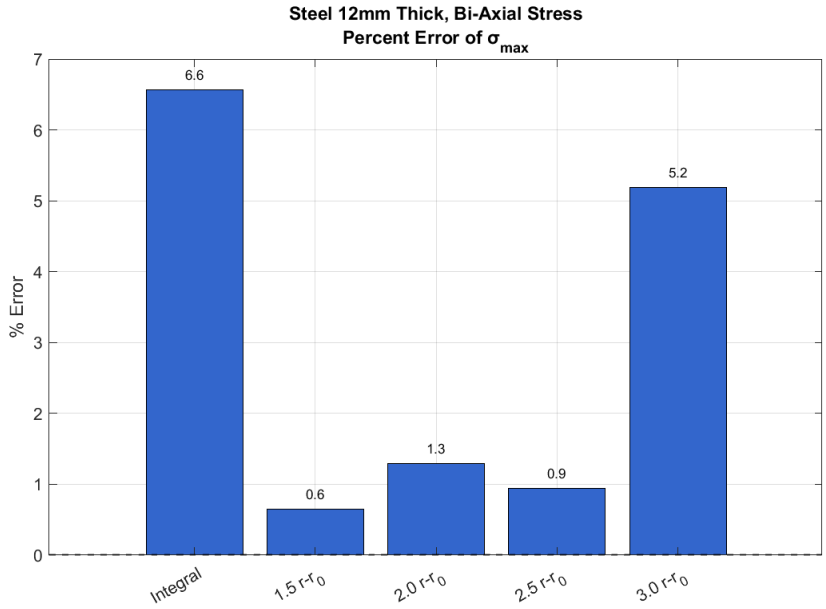


Figure 27: Max Stress Percentage Error, FE

of 0.4mm. A partial stress profile for steel can be created using the radial displacement method of calculating residual stress with DIC measurement from 0.4 to 1.0mm using curve 1.5 r-r0. Radial displacements in a steel part with applied 40% yield stress were greater than the DIC minimum past the recommended depth of 0.25mm for curve 1.5 r-r0. For steel, it is recommended to use radial displacements at 1.5r-r0 for residual stresses calculation regardless of the stress magnitude. For the titanium plate with 20% of yield applied stress, radial displacements at 1.5, 2.0, and 2.5 r-r0 surpassed the minimum displacement required for DIC measurement. For 40% yield applied stress, all four investigated radial distances provided displacements larger than the DIC minimum. Based on these results, the radial displacement method is ideal for calculating small residual stresses in titanium with DIC measurement. For residual stress measurement in a titanium part, all four presented radial distances are recommended for general use. The radial displacement method of calculating residual stresses with DIC measurement can be applied to aluminum, steel, and titanium parts by using displacements at the recommended radial distances.

The radial displacement method has been extended to incremental hole drilling in this study. The method shows great accuracy for uniaxial and biaxial stresses in aluminum, steel, and titanium through finite element analysis. Implementation of this method is dependent on the part thickness, the assumed magnitude of the residual stresses, and the number of displacements and corresponding theta values obtained. As mentioned previously, multiple sets of a and b coefficients are provided in the appendix to allow for flexibility in sample dimensions. Choosing the right set of coefficients is integral to the success of the radial displacement method. Using the correct r-r0 ratio for the radial displacements is also important to the accuracy of stress measurement. It will be most helpful to perform calculations with multiple r-r0 ratios if the magnitude of the stress state is unknown. From there, the user can implement judgement based on the agreement of all r-r0 ratio curves and choose the best ratio for drawing conclusions. It is also advantageous to use many radial displacements and corresponding theta values for stress calculation. It was originally believed that limiting radial displacements to certain theta

ranges based on assumed residual stress direction would be advantageous for accurate use of the radial displacement method. It has been found in this study that the most accurate and conservative stress values are the result of using as many radial displacements at available theta values as provided by the finite element simulation or measurement type. This topic is discussed more in the following section where the radial displacement method is applied to data collected using 3D DIC.

3D DIC vs Strain Gauge Rosette: Radial Displacement and Integral Methods

Results of 4-point bending tests show good agreement between 3D DIC and standard strain gauge rosette calculations. For both out of plane and in plane bending tests, the 1.5 r-r0 curve was used to collect displacements due to the magnitude of the applied stresses. The results of the strain gauge rosette integral method, DIC pseudo rosette integral method, and DIC radial displacement method are compared below using normalized RMS errors for both out of plane and in plane bending tests. For the out of plane 4-point bending test, the DIC rosette results had the highest disagreement with the applied stress. This is because the integral method stress profile showed relatively non-uniform stresses, while the strain gauge rosette and the DIC radial displacement methods were more uniform. The nonuniformity in DIC integral method calculations arises from less stable strain data. Because of this non-uniformity, the RMS error is higher for the DIC rosette. The RMS error for the DIC rosette was calculated for stresses at depths of 0.275 to 0.875mm because the stresses past that depth were outliers compared to the other stress values and based on knowledge that the applied stress was uniform. The average of the stresses over the depth into the part for the DIC rosette were in good agreement with the applied stress. As mentioned previously, the average of the stress over the depth into the part is often taken as the result of the residual stress analysis. The percentage errors for the average of the maximum principal stresses for each residual stress calculation method are shown in Figure 29.

The RMS error results for the in plane bending test were similar to those of the out of plane bending test. For the in plane bending test, the strain gauge rosette stress results

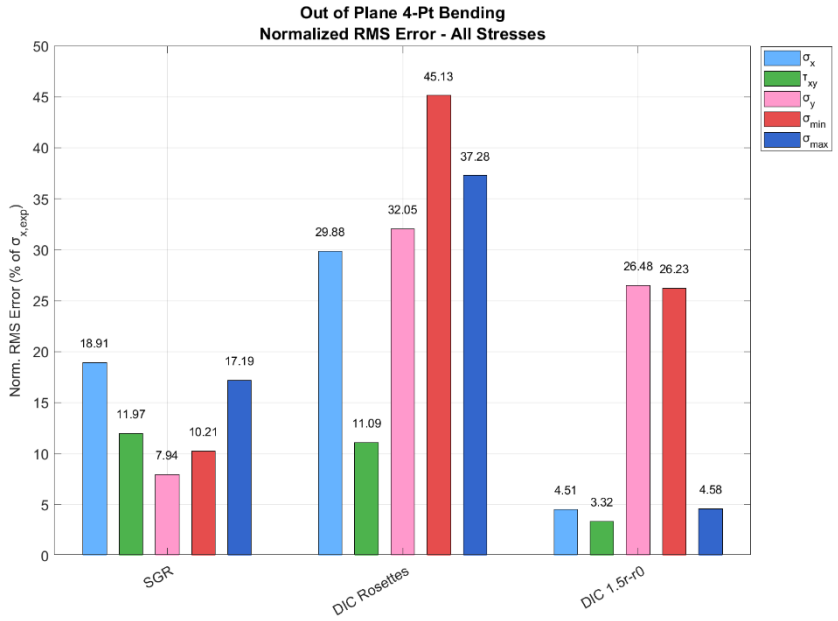


Figure 28: RMS Error, Out of Plane Bending Stress Results

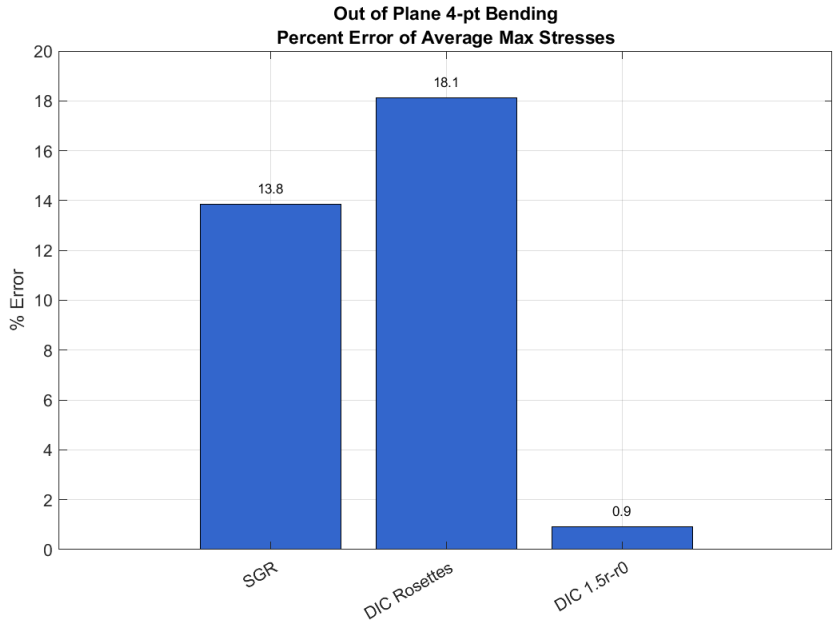


Figure 29: Max Stress Percentage Error, Out of Plane Bending

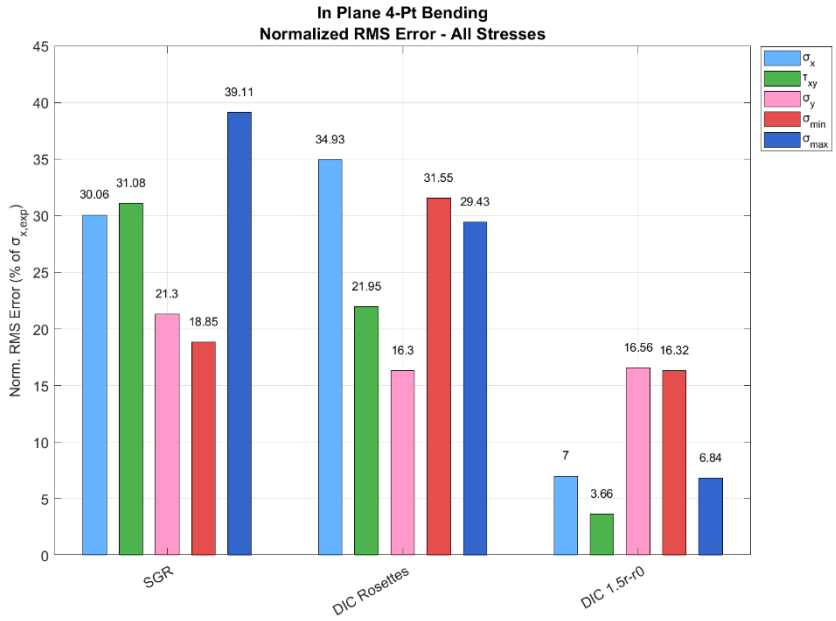


Figure 30: RMS Error, In Plane Bending Stress Results

have higher RMS errors. The radial displacement method using curve 1.5 r-r0 had the best agreement to the expected value across the entire profile, as shown in Figure 30. The strain gauge rosette and DIC integral method have higher RMS errors, but the average value of the stresses over the depth into the part have low percentage errors compared to the applied stress value as seen in Figure 31. For the in plane bending test, the strains varied across the hole drilling area which is likely the cause of lower agreement of the integral method results. DIC software is also less accurate at calculating low strains in the Y direction, which can contribute to higher errors. Nonetheless, the average values of the integral method and radial displacement results are in good agreement with the applied stress.

For the out of plane and in plane bending test the curves 1.5 r-r0 used for radial displacement method calculations had 271 and 273 data points respectively. As previously stated, it was initially assumed that using specific ranges of displacements at theta values amicable to the assumed stress direction would be advantageous. It was discovered in this study that including more data points in calculations leads to more stable and uniform results when obtaining radial displacements from DIC data. See Figure 32 where cartesian stresses were calculated from curve 1.5 r-r0 using thetas from 0 to 10, 80 to 100, and 350 to 360 degrees. The result shows Y stress values hovering around 0 MPa, which was the expected value for this test. However, it leads to a slightly less accurate result for the X stress and an unstable Y stress profile. Although there is assumed to be no applied Y stress in the four-point bending configuration, it is conservative to use the entire theta range and have a calculated Y stress that is higher than the applied stress. For these reasons, it is recommended that all collected radial displacements at the entire theta range be used to calculate the residual stresses in practice.

It is seen in this study that the radial displacement method of calculating applied stresses in 4-point bending fixtures using incremental hole drilling results in a highly accurate uniform stress profile into the part. Compared to the strain gauge rosette and DIC integral method results, the radial displacement method proves to be more accurate from a stress

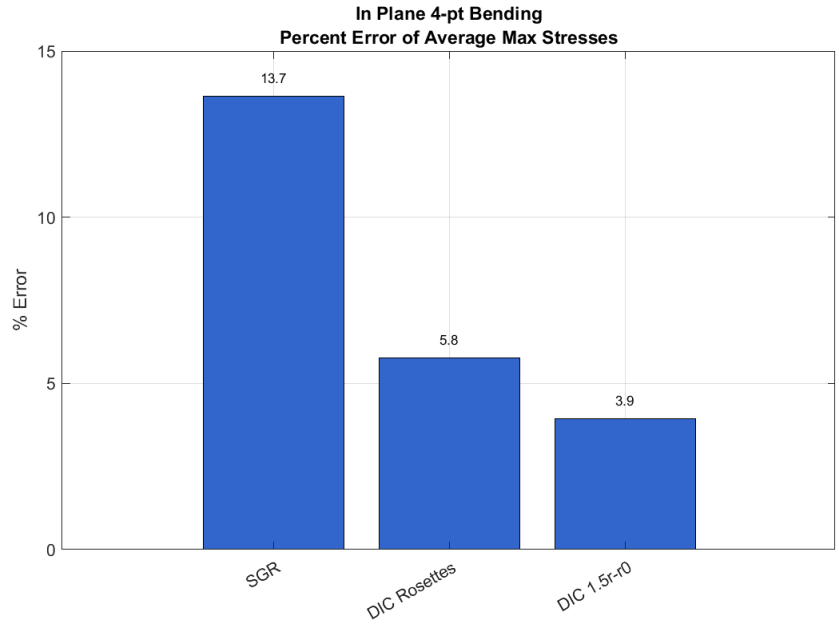


Figure 31: Max Stress Percentage Error, In Plane Bending

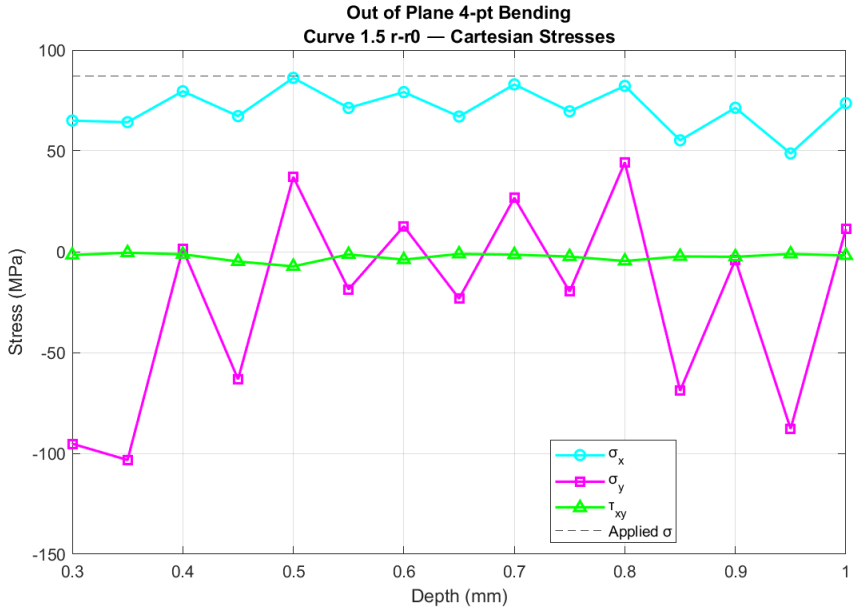


Figure 32: Out of Plane 4-pt Bending Radial Displacement Method Results with Limited Theta Range

profile view. In both four point bending experiments, the radial displacement method was most accurate in detecting the absence of applied shear stress within the part. All three residual stress calculation methods yielded accurate results when taking the average of the maximum principal stresses over the depth into the part.

Conclusions

Finite element models on plates of various materials, depths, and loading conditions were successfully used to determine calibration coefficients for implementation of the radial displacement method of residual stress calculation to incremental hole drilling. Finite element models were used to validate the derived coefficients and were compared to the traditional integral method outlined in ASTM E837. This study compared the stress profiles and average of the stress profiles for various materials in Abaqus finite element software and found the radial displacement method to be comparable to the standard integral method. Recommended radial distances for use in residual stress calculation of aluminum, steel, and titanium parts have been presented. For aluminum, displacements at radial distances of 1.5 and 2.0 r-r0 are recommended for general use. For steel, it is recommended to use radial displacements at a radial distance of 1.5 r-r0, and at low residual stress magnitudes a partial depth profile may be necessary. It was found that all four proposed radial distances (1.5, 2.0, 2.5, and 3.0 r-r0) are suitable for residual stress calculation using radial displacement method in titanium parts. These recommendations are made based on the minimum displacement measurable by DIC.

The radial displacement method for calculating residual stress was further validated with 4-point bending tests. These four point bending tests successfully compared the standard hole drilling strain gauge rosette to 3D DIC. 3D DIC was used to calculate residual stress from the integral and radial displacement methods. The results of 3D DIC were accurate and compatible with those of the strain gauge rosette. Unique assemblies of DIC pseudo rosettes were implemented to take advantage of the large number of data points available with the use of 3D DIC. Alongside the increased number of strain gauges, the radial displacement method utilized approximately 270 data points of radial displacements to

calculate the applied stress from the radial displacement method. This study successfully utilized the surplus of data available with DIC measurement and improved on the residual stress calculation method. The recommendations made from finite element analyses for various materials are provided for application to many industries where the presence of residual stress can be critical.

Acknowledgments

Thank you to my advisor, Dr. Penumadu, for assistance and support with this project. Thank you to Ken Thomas for assembling the CNC machine and for designing and machining the four point bending fixtures used in this study. Thank you to Andy Baker and Larry Roberts for use of the Tickle machine shop and assistance with the CNC machine. To Hannah Maeser, thank you for helping me get this research off the ground and for the time spent training and assisting with the DIC cameras. Thank you to Dr. Sarah Mobley for allowing us to use the micro measurements system 8000 for strain gauge and load cell data collection.

CHAPTER TWO

RESIDUAL STRESS MEASUREMENTS IN ALLOYS: MODIFIED HOLE DRILLING METHOD VERSUS SURFACE X-RAY DIFFRACTION AND BULK NEUTRON SCATTERING

Abstract

Type-1 Residual stresses within an alloy result from complex processes associated with additive and subtractive manufacturing, extrusion, casting, machining, and welding due to thermo-mechanical loading are critically important to evaluate reliably for engineering applications. Using ring and plug samples made from Al 7050 alloy, we prepared samples with predetermined locked in residual stress by allowing inner plug to expand in outer ring while allowing the plug to warm from liquid nitrogen temperature to room temperature. Using a modified hole drilling procedure enhanced with integrating three-dimensional Digital Image Correlation (DIC) technique, residual stresses as a function of location and orientation were evaluated by advancing small diameter holes of 1 mm radius to a depth of 1 mm using incremental hole drilling using a custom developed CNC drill integrated with DIC cameras with suitable optics to realize high spatial resolution. The methodology was validated by comparing the results with strain gage rosette-based measurement and data inversion using analytical models currently approved in existing standards. An alternative method with improved accuracy was developed using radial displacement contour method with inverse Finite Element Method to infer normal and shear residual stresses. At discrete locations on the surface, x-ray diffraction was utilized to evaluate residual stresses using $\mathrm{Sin}^2\mathrm{X}$ method. Using neutron diffraction, bulk residual stresses were also obtained at target locations to compare with hole drilling method. Initial results using energy selective neutron imaging were also obtained for these samples to identify atomic planar spacing as a function of location and orientation towards developing methods for inferring residual stress using neutron imaging.

Introduction

Residual stresses are those which are “locked in” to a part through manufacturing, cyclical use, and other processes [1]. Residual stress develops due to eigenstrains between different areas of a sample. Residual stresses are typically categorized into three types based on the length scales over which they exist; Type I, Type II, and Type III [20]. Type I stresses are macroscopic and are assumed to be uniform from grain to grain. Type

II stresses typically exist over a length apropos to that of the material grain structure and are often found in polycrystalline materials. Type III stresses exist within the material grains, and include those stresses that arise due to dislocations [3]. Different measurement techniques are favorable to the type of residual stress present within a part. Diffraction based techniques contain the ability to measure and infer all types of residual stress, based on the measurement and characteristic volumes. Mechanical residual stress measurements such as hole drilling can measure Type I residual stresses only [20]. The presence of residual stress can have negative and catastrophic effects on the performance of a part. The ability to accurately measure residual stress is crucial to civil engineering, additive manufacturing, aerospace, and a variety of other industries [3]. Nearly all manufacturing processes impose residual stress on a part, including curing, quenching, and welding [21].

For residual stress measurement technique comparison, a shrink fit aluminum ring and plug assembly was created. This sample assembly is advantageous as it allows for a known amount of induced residual stress. The first method applied here uses incremental hole drilling with 3D DIC (digital image correlation) and conventional strain gauge rosette. Data collected from DIC measurements can be used for residual stress calculations via the integral and the radial displacement methods. The integral method is outlined in ASTM E-837-20 for use with standard strain gauge rosettes. The radial displacement method was initially proposed by Nelson, and is applied to incremental hole drilling here [5], [6]. The following methods evaluated here are diffraction-based measurements, where changes in interplanar atomic spacing are measured. X-Ray diffraction measurements are completed using the Sin^2X method. The Sin^2X method is a grazing incidence x-ray diffraction measurement which collects data near the sample surface [4]. Bulk neutron diffraction measurements were completed to map strains through the radial thickness of the material. For diffraction-based measurements it is necessary to have an accurate measurement of the unstrained lattice parameter. Finally,

preliminary neutron imaging and Bragg edge measurements were used to evaluate the part assembly.

Blind hole drilling is a common method used in engineering spaces to measure residual stress. When material is removed from a stressed part by drilling, the strains around the drilled area are allowed to relax on the order of the residual stress present in the part. When material is removed incrementally, as presented here, a stress profile against the depth into the material can be created [1]. The blind hole drilling procedure is typically completed with standard strain gauge rosettes as the measurement system. 3D DIC is applied to the integral method of residual stress measurements for incremental hole drilling. The integral method is outlined in ASTM E837 and standard strain gauge rosette orientations and sizes are provided [5]. The typical strain gauge rosettes can be replicated in DIC software and easily applied to the integral method [7]. By replicating strain gauges with DIC, the results can be directly compared to standard strain gauge rosettes [7]. Data collected using 3D DIC can also be used to calculate residual stresses using the radial displacements around the drilled hole area [6]. To complete a stress measurement using radial displacements, finite element analyses were performed to obtain calibration coefficients.

The basis of diffraction residual stress measurement techniques is built on Bragg's law which relates the wavelength of radiation, the distance between lattice planes, and the angle at which radiation is scattered. Diffraction techniques measure a strain averaged over the sample gauge volume utilized during measurement. X-ray diffraction penetrates only the surface of the sample, approximately 10s of microns deep. Measurements through a sample are possible through surface removal techniques [20]. Short penetration depth of x-rays is useful to the Sin^2X method of residual stress measurement because it allows the stress in the sampled region to be assumed as in plane. Using the Sin^2X method, there is no need for an accurate strain free lattice spacing. For plane strain, the residual stress can be inferred by the slope of the lattice spacing with specimen tilt in X.

Use of the Sin^2X measurement technique is valid for determining residual stresses near the surface of a sample [4].

Neutron diffraction is an alternative and often favorable technique to x-ray diffraction. Benefits of neutron diffraction measurements include the ability to penetrate on the order of centimeters through a sample, nondestructive properties, adjustable spatial resolution, and inference of bulk macroscopic engineering stress [4], [20]. The high penetration power of neutrons allows for access to the inside of solid samples, compared to surface penetrating abilities of x-rays [20]. Neutron diffraction measurements were completed here with a continuous wavelength source at the high flux isotope reactor at Oak Ridge National Laboratory. With a constant wavelength, the d spacings through the bulk of the sample can be measured with Bragg's law. Neutron diffraction measurements are best suitable to areas far from the sample edge [4]. In this way, x-ray diffraction, blind hole drilling, and neutron diffraction residual stress measurements are complimentary. X-ray diffraction collects measurements at the sample surface, blind hole drilling collects measurements at a small depth into the part, and neutron diffraction collects measurements far from free edges. These techniques together allow for a rounded analysis of the residual stress field within a part.

To further complete the residual stress analysis of the ring & plug sample, experimental and preliminary neutron Bragg edge imaging was performed. Neutron imaging allows for large volumes of a sample to be investigated. From neutron imaging, users can identify sample density, strains, texture, and other material properties. Neutron scattering methods identify features over an average gauge volume, whereas neutron imaging techniques can identify material properties in real space. Neutron imaging measurements are based on the attenuation of the neutrons at specific wavelengths throughout the measurement. Neutron imaging techniques are often limited by the background of the transmitted beam. Bragg edge imaging refers to spatially resolved wavelength resolved transmission measurements. With Bragg edge imaging, information is collected from visible Bragg edges in polycrystalline samples. When measuring strain with Bragg edge imaging, the

data is averaged through the sample thickness and the strain is measured along the incident beam direction [22]. Neutron Bragg edge imaging is an emerging technique with high interest and importance to the residual stress community.

Materials and Methods

Ring and Plug Sample Assembly

The ring and plug samples were created as outlined in the VAMAS report. The separate ring and plugs were manufactured from aluminum alloy 7050. The outer diameters of the unassembled ring and plug were 50 and 25.03mm respectively. This provided a nominal radial interference of 15 micron. The height of the ring and plug assembly is 50mm. The assembly of the sample is as follows, replicating the procedure from the VAMAS report. A ring was placed in liquid nitrogen and then allowed to equilibrate thermally. Then, the ring was removed and allowed to come to room temperature. The ring was then placed in a small oven and heated to 50° C. Following this procedure, a plug was placed in liquid nitrogen and allowed to equilibrate thermally, then the plug was quickly removed from the liquid nitrogen and inserted into the ring [23]. This procedure was identically replicated for two samples used in this study. One sample was used for IHD and XRD measurements at the University of Tennessee, and a separate sample was used for neutron measurements at Oak Ridge National Laboratory.

Finite Element Analysis

Finite element analysis of the aluminum ring and plug assembly was completed in Abaqus Standard 2021 [16]. Elastic press-fit modeling was used to assemble the sample with a diametral interference of 30 micron. Due to symmetry, $1/8^{th}$ of the part was modeled with appropriate symmetry boundary conditions, shown in Figure 33. Eight node linear brick reduced integration elements, C3D8R were used with an approximate element size of 0.5mm. The finite element mesh is visualized in Figure 34. A partition was made from the part center to the outer diameter to obtain expected stress values

through the width of the part. The stress values were converted to polar coordinates in Abaqus to obtain radial, hoop, and axial stresses.

Incremental Hole Drilling

For collection of 3D DIC data, two 12-megapixel optical cameras were used. With the employed DIC setup the cameras provide 4096 x 3000-pixel resolution resulting in a pixel size of 6.10 micron. The setup consisted of 100mm focal length lenses and 50mm extenders. This setup provides a 25 x 15mm area of view for DIC measurements. For optimal data processing, 15 DIC images were collected for each measurement. Images were collected at a rate of 2 Hz to decrease total time of measurement. All DIC images were collected and processed in Aramis Professional 2020 software [17].

The aluminum ring and plug sample was prepared for DIC measurement with a stochastic speckled pattern using airbrush painting techniques. Holes of 2mm diameter were drilled incrementally in steps of 50 micron to a total hole depth of 1mm. All measurements were performed on the CNC sample stage. Reference images were taken in the DIC viewing area, then the drilling sequence was initiated. The CNC stage moved the sample from the DIC viewing area to the drilling area. After each drill step of 50 micron, the sample was returned to the DIC viewing area for measurement images to be taken. This sequence proceeded until the final depth of 1mm was obtained. In total, 10 DIC IHD measurements were performed on the ring and plug sample; four in the top of the ring, four in the side of the ring, and two in the top of the plug.

Spatial and temporal filters in Aramis software were used to minimize noise from DIC measurements, acting as minimal rigid body compensation. Since the entire DIC view is occupied by the sample area, the relative noise was high. Spatial average filtering allows averaging of strain and displacement measurements over multiple points of the surface component to reduce the influence of outlying data points that arise from the limited DIC view. Based on the filter size, n, strains are averaged over n number of points in the neighborhood of the initial measurement point. Temporal average filters average

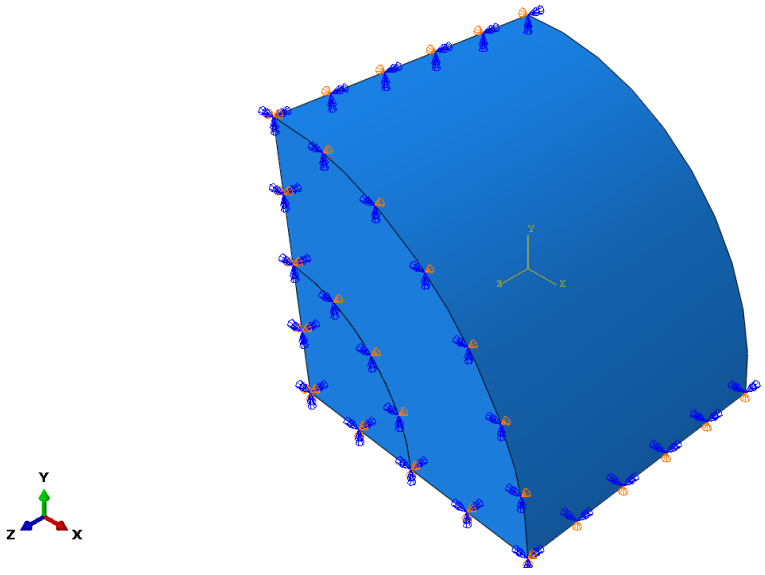


Figure 33: FE Al Ring & Plug Part

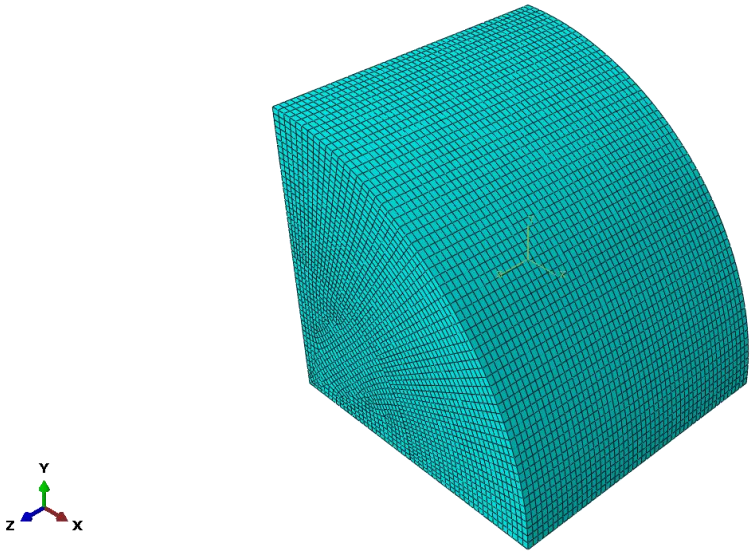


Figure 34: FE Al Ring & Plug Mesh

measurements over neighboring images. Since 15 images are taken for each measurement in the current study, a temporal average filter value of seven is applied to all measurements: allowing data to be average over seven images before and after. Use of spatial and temporal average filters ensures noise reduction and performs minimal rigid body motion compensation.

The DIC data was used to calculate residual stresses using the standard integral method outlined in ASTM E837 [5]. H-Drill software is used to perform integral method calculations [19]. To process data for the integral method, DIC pseudo strain gauges were placed around the drilled hole. These DIC pseudo gauges were modeled after micro measurements CEA-06-062UL-120 strain gauge rosettes. Eight individual strain gauges are placed on the surface component using the "create component region" tool in Aramis. From these eight individual strain gauges, eight DIC pseudo strain gauge rosette assemblies were created. The final residual stress result is obtained by using strains from each DIC rosette to perform the integral method, averaging the result of choice DIC rosette across the entire depth into the part, then averaging the stress result of each DIC rosette. DIC rosette assemblies are chosen based on the stability and uniformity of the pseudo gauge strain data. This method is thorough, and due to the averaging minimizes defects and incorrect measurements.

For direct comparison, incremental hole drilling measurements with conventional strain gauge rosettes were performed in the ring of the sample. Micro measurements CEA-06-062UL-120 strain gauge rosettes were used in this study. The drilling parameters were identical to those of DIC measurements, and an integral method analysis was performed to calculate the residual stress profile for each measurement location. Between each drilling increment, the spindle was stopped for 30 seconds to decrease noise interference in the strain gauge rosette measurements. As for DIC, the averages of the integral method stress profile analyses are taken as the final residual stress values presented here. Single strain gauge rosette measurements were made in the top of the ring and in the side of the ring.

The DIC data was also used to calculate residual stresses using the finite element radial displacement method. In this method, radial displacements were collected at prescribed radial distances from the hole center. These radial displacements were used with a calibration matrix at measured angles to determine residual stress. This method was proposed by Nelson [6] for use with single step hole drilling, and is expanded here for application to incremental hole drilling. The equations used to measure residual stress from radial displacement are as follows:

$$\boldsymbol{u = Ks} \qquad \textit{Eqn 2.1}$$

$$\begin{bmatrix} u_{r1} \\ u_{r2} \\ \cdots \\ u_{rn} \end{bmatrix} = \begin{bmatrix} A + Bcos(2\theta_1) & A - Bcos(2\theta_1) & 2Bsin(2\theta_1) \\ A + Bcos(2\theta_2) & A - Bcos(2\theta_2) & 2Bsin(2\theta_2) \\ \cdots & \cdots & \cdots \\ A + Bcos(2\theta_n) & A - Bcos(2\theta_n) & 2Bsin(2\theta_n) \end{bmatrix} \begin{bmatrix} \sigma_x \\ \sigma_y \\ \tau_{xy} \end{bmatrix} \qquad \textit{Eqn 2.2}$$

Where , $A = r_0(1+\nu)a/2E$, $B = r_0 b/2E$, r_0 = hole radius, ν = Poisson's ratio, E = elastic modulus, θ is the angle from the pre-defined X direction, and a & b are the coefficients derived from finite element analysis. These equations are valid and applicable to materials with linear elastic and isotropic behavior [6]. The calibration coefficients, a & b, used here were derived from a 20mm thick aluminum plate finite element model with applied uniaxial stress that was constant with depth. These coefficients are applicable to stresses that vary due to the nature of their derivation.

X-Ray Diffraction

X-ray diffraction residual stress measurements were completed at the Institute of Advanced Materials Manufacturing (IAMM) diffraction laboratory. Sin^2 X measurements, an adaptation of the $Sin^2 \Psi$ method specific to available diffraction geometry, were performed in radial and hoop stress directions. Measurements were performed with copper kα radiation source and an average measurement volume of 0.204mm^3. During the initial measurement, positive and negative tilts in X were performed to determine if shear splitting would occur. No shear splitting was found, so

all subsequent measurements were completed with positive X tilts only. The approximate measurement time for each radial and hoop measurement was 1.5 hours.

Radial and hoop stresses were mapped at four locations across the sample. To obtain radial and hoop measurements, the sample was tilted in X along the directions shown in Figure 35. Symmetric measurements were made in the ring at 0.75r, where r is the overall radius of the sample, and in the plug at 0.25r. To obtain stress at each location, a linear fit was performed:

$$d = m * sin^2(X) + d_0 \qquad \textit{Eqn 2.3}$$

Where $m = d_0 \frac{\sigma}{E}(1 + \nu)$, E = Young's Modulus, ν = Poisson's Ratio, d_0 = spacing at $sin^2(\chi)$=0, σ = residual stress [24].

Neutron Diffraction

Residual stress measurements were completed with the high intensity diffractometer for residual stress analysis (HIDRA) beamline at the high flux isotope reactor (HFIR) at Oak Ridge National Laboratory [25]. The neutron diffraction geometry is illustrated in Figure 36. The gauge volume for neutron diffraction measurements was 3mm incident beam width, 3mm diffracted beam width, and 20mm out of plane (3x3x20mm) with steps of 1mm for all measurements to achieve oversampled results. Neutron diffraction measurements were completed for the hoop and radial directions. For each measurement, the interaction volume was perpendicular to the stress direction. The exposure time for data collection was approximately 200 seconds per point. An incident wavelength of ~1.54 angstroms, copper kα, was used for all measurements. The (311) plane was measured based on the VAMAS report and because the (311) plane is most representative of the macro strain [23]. The pyRS package was used to reduce the neutron events to diffraction data. The raw data relies on instrument parameters utilized during data collection, and use of pyRS removes these parameters from the data [26]. Bragg's law was used to measure atomic planar spacing, d_{hkl}, changes.

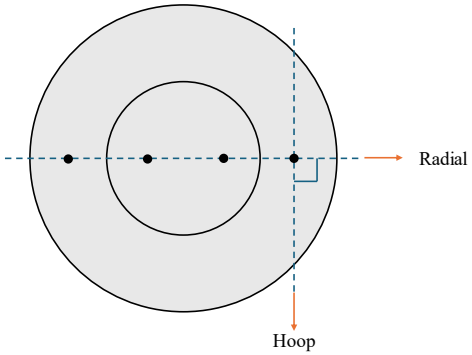


Figure 35: XRD Radial and Hoop Measurement Directions

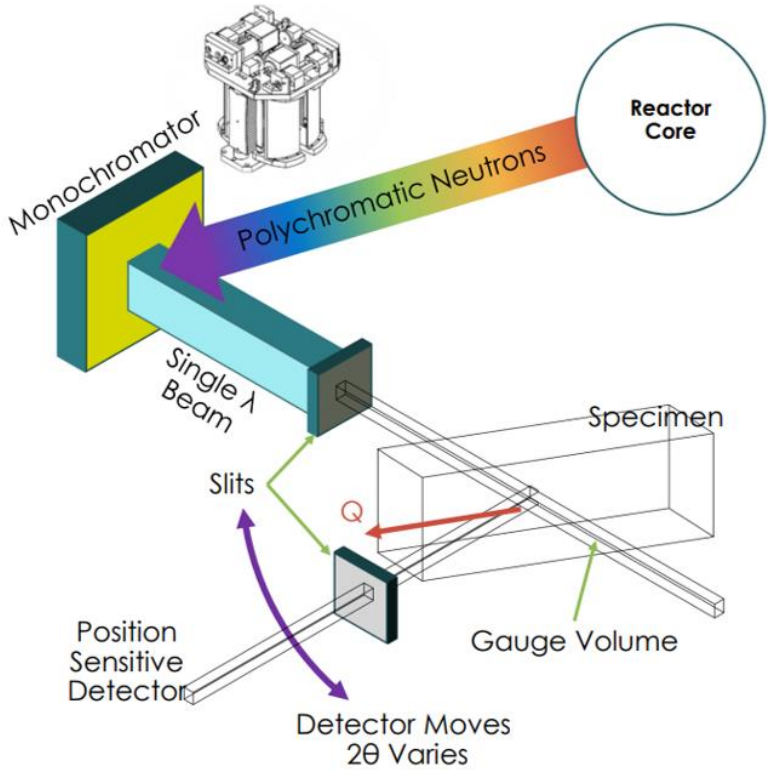


Figure 36: Neutron Diffraction Geometry

$$\lambda = 2d_{hkl} sin\,(\theta_{hkl}) \qquad \textit{Eqn 2.4}$$

Where λ is the wavelength of the incident neutrons and $2\theta_{hkl}$ is the measured angle of the diffraction peak. Measurements were performed through the thickness of the ring and plug sample, at approximately half of the sample height. In lieu of axial strain measurements, the hoop and radial stresses for the neutron diffraction data are approximated based on the assumption that axial stresses are low. The following equations were used for stress approximation as outlined in VAMAS [23]. Another approximation made for stress calculations was the unstrained atomic planar spacing.

$$\sigma_\theta = \frac{E}{1-\nu^2}(\varepsilon_\theta + \nu\varepsilon_r) \qquad \textit{Eqn 2.5}$$

$$\sigma_r = \frac{E}{1-\nu^2}(\varepsilon_r + \nu\varepsilon_\theta) \qquad \textit{Eqn 2.6}$$

Bragg Edge Imaging

Preliminary Bragg edge imaging results were performed at VENUS beamline at SNS at Oak Ridge National laboratory [27]. Measurements were taken for one hour and were averaged over the whole detector. The location of measurements on the ring and plug sample is shown in Figure 37. One resulting measurement is presented here at the prescribed radial location of 0°.

Results

Finite Element Analysis

Results of the finite element model were taken as polar stresses from the center to the outer radius of the ring and plug. The radial, hoop, and axial stresses through the thickness of the modeled part are shown below in Figure 38. The analyzed stresses follow the expected trend for the diametral interference used in this study.

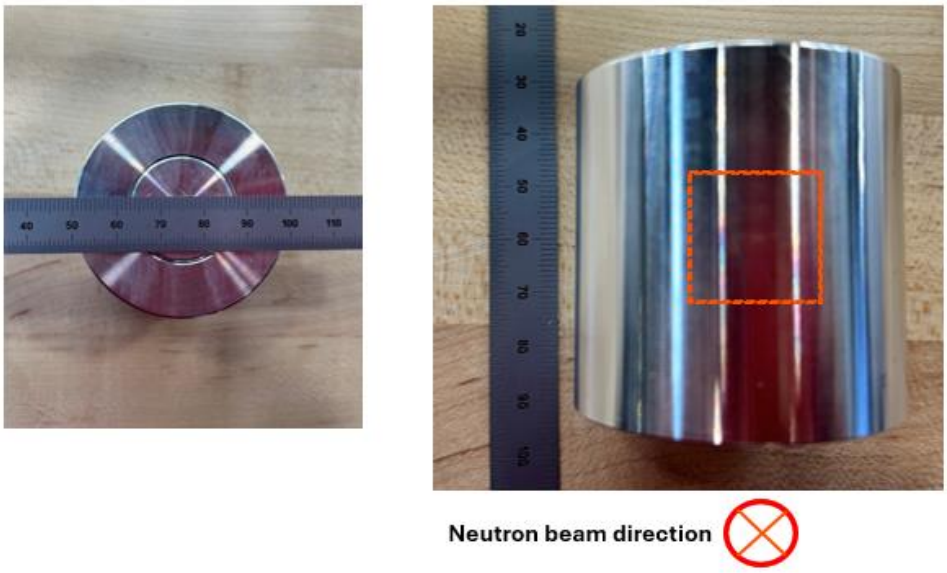


Figure 37: Neutron Imaging Measurement Location

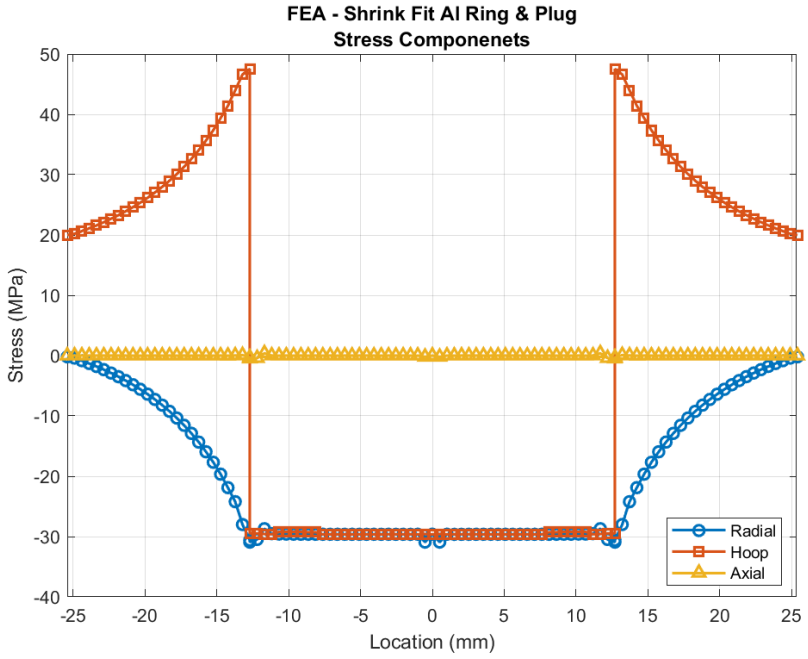


Figure 38: FE Radial, Hoop, and Axial Stresses

Incremental Hole Drilling

Incremental hole drilling measurements with 3D DIC were performed at radial locations around the sample. Hole drilling on the top of the sample is shown in Figure 39. The residual stress results calculated from radial displacements in the top of the ring, top of the plug, and side of the ring are presented below in Figure 40, Figure 41, and Figure 42 respectively. These results are from the radial displacements at distance 1.5r-r0 from the drilled hole center, based on the known stress magnitude. For the ring side measurement at 135°, the 1.5r-r0 was not viable for displacement measurement due to speckle pattern damage close to the drilled hole.

In the cumulative comparison of all IHD results, Figure 43 and Figure 44, the ring side measurement at 135° was computed from displacements at 2.0r-r0. DIC integral method analysis averages are included in the cumulative comparison when applicable. In some measurement locations, there were no smooth strain profiles that created a useable DIC rosette and could not be included. Error bars were constructed from standard deviation analysis of each respective measurement method. In each figure, the maximum and minimum stresses represent the principal stresses from stress calculation. In relation to the ring & plug sample, the maximum and minimum stresses in the ring represent the hoop and radial stresses respectively.

X-Ray Diffraction

X-ray diffraction results in the hoop and radial direction are shown at the location of the ring and plug sample in Figure 45. Linear fits of the d-spacing and Sin^2 X data for each location are provided in the appendix. For direct comparison, DIC integral method results at the earliest depth into the sample, 0.025mm, are included. The expected stress profile from finite element analysis is provided with separate y-axis values to show the trend of the expected stress profiles.

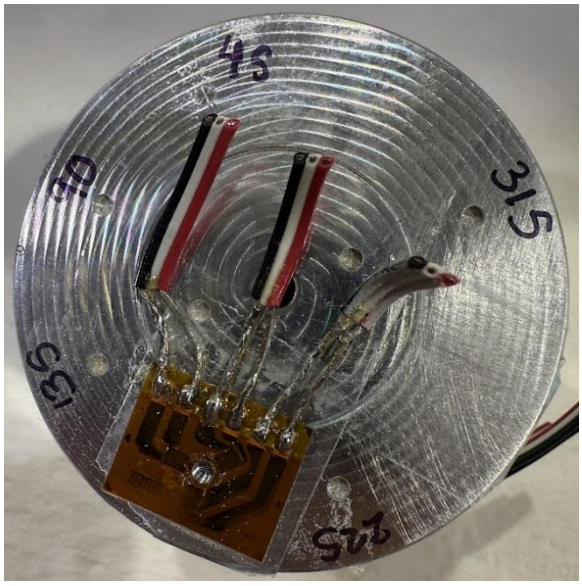


Figure 39: Ring & Plug After IHD

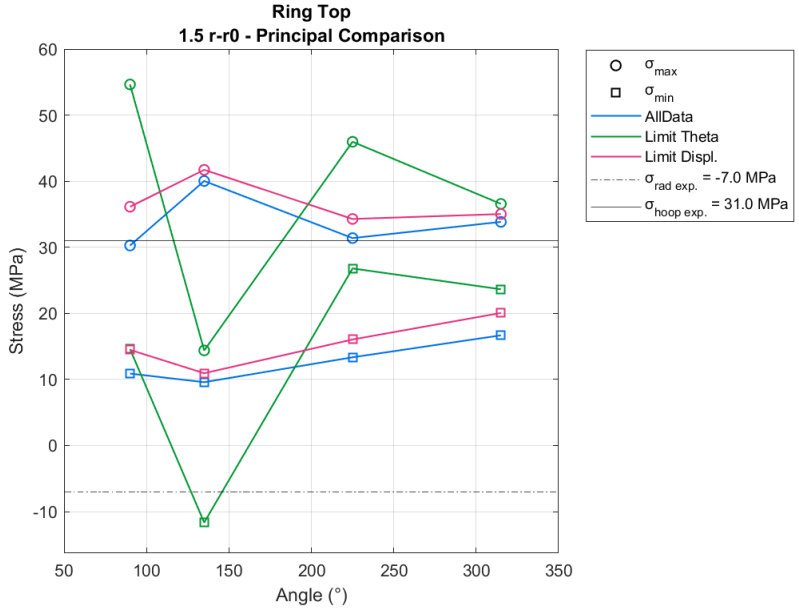


Figure 40: DIC Radial Displacement Results, Top of Ring

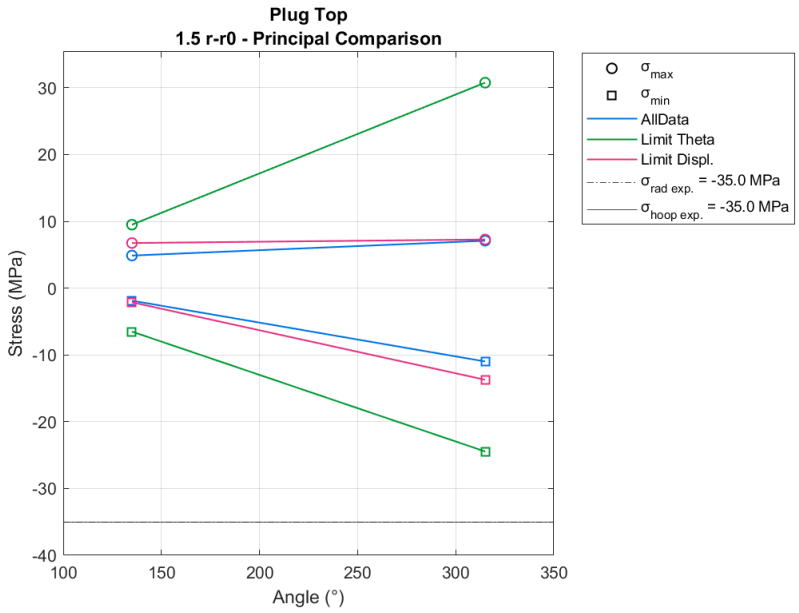


Figure 41: DIC Radial Displacement Results, Top of Plug

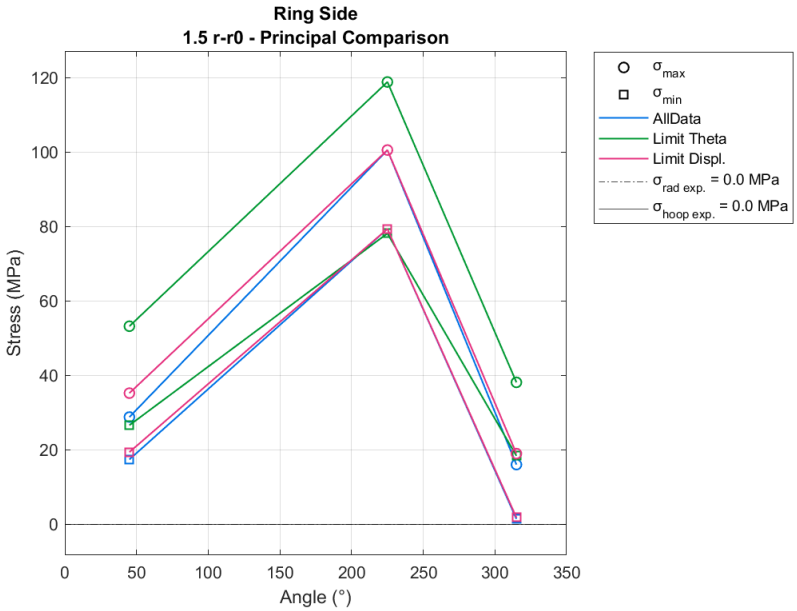


Figure 42: DIC Radial Displacement Results, Side of Ring

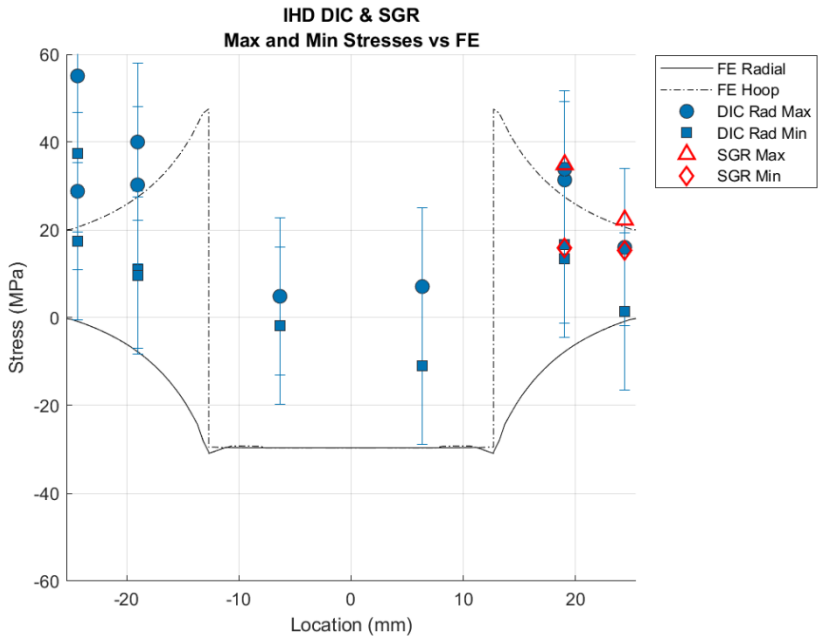


Figure 43: DIC Radial Displacement Method & SGR Compared to Finite Element Profiles

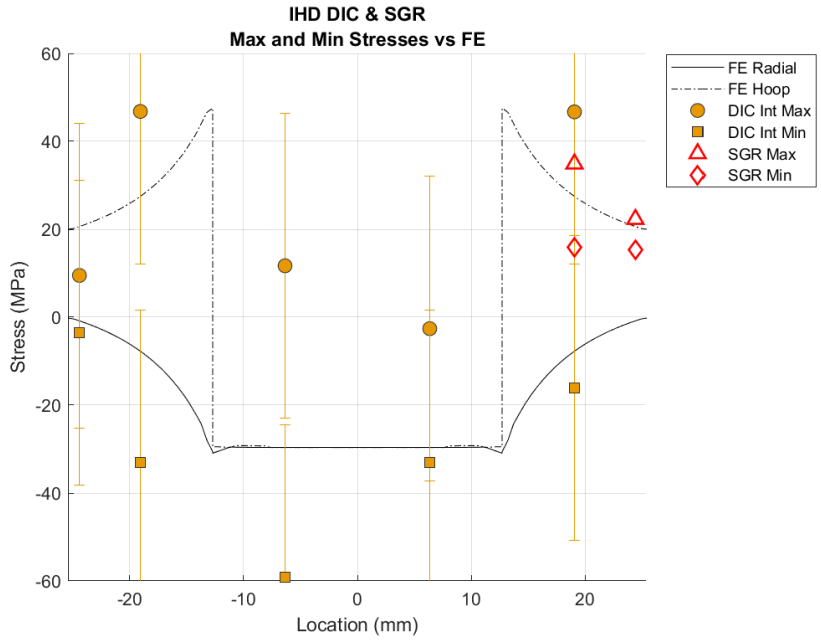


Figure 44: DIC Integral Method & SGR Compared to Finite Element Profiles

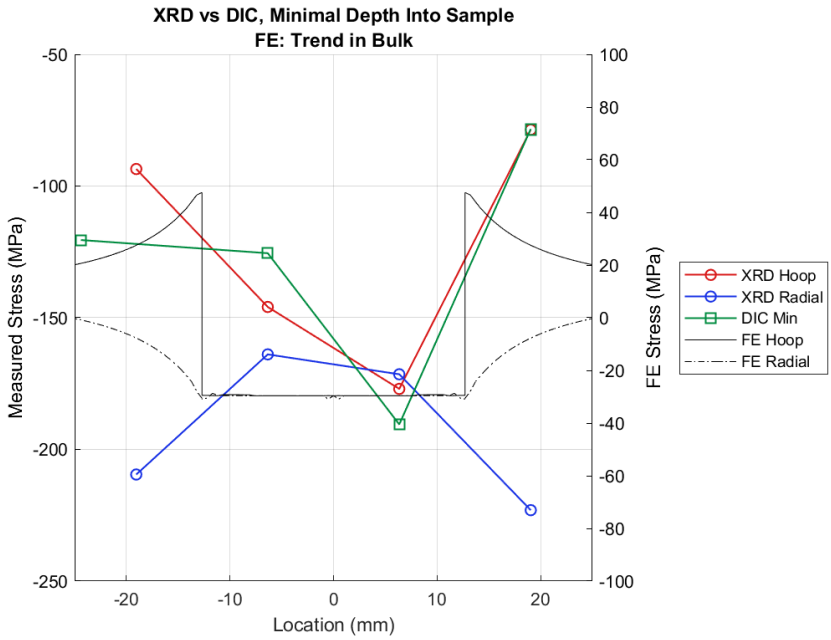


Figure 45: XRD Radial and Hoop Measurements & DIC Integral Method Results at Early Depths

Neutron Diffraction

The neutron diffraction results in the aluminum ring and plug sample are presented here. The results of neutron diffraction in the radial and hoop directions through the thickness of the sample are shown in Figure 46 and Figure 47 respectively. In both plots, the expected stress profiles from finite element analysis are included. An unstrained d spacing of 1.2255 Å was used to calculate the strains measured by neutron diffraction.

Bragg Edge Imaging

Bragg edge results through the width of the aluminum ring and plug were successfully obtained. The results are presented here in Figure 48. For direct comparison, the experimentally determined values are plotted on a logarithmic scale. The sharp drop in neutron attenuation in both theory and experiment indicates the location of a Bragg edge. A summed image result of the grey scale across all collected wavelengths is provided in Figure 49.

Discussion

Finite Element Analysis

A successful finite element analysis to determine expected stress profiles was completed for this study. The radial, hoop, and axial stresses follow expected trends for the sample creation. There are some artificial defects near the center of the part and interface of the ring and plug, specifically in the radial and axial directions. These were determined to be artificial based on the smooth profile of the hoop stress. These defects were more pronounced with the initial mesh of the model, with approximate element sizes of 1.0 and 0.5mm in the ring and plug respectively. To evaluate the validity of the defects, the element sizes in the ring were decreased to 0.5mm match the plug. This decreased the defects in both the sample center and at the interfaces and therefore the effects were determined to be artificial. To avoid lengthy computational times and related high expenses, the mesh was preserved with an overall element size of 0.5 and again it was

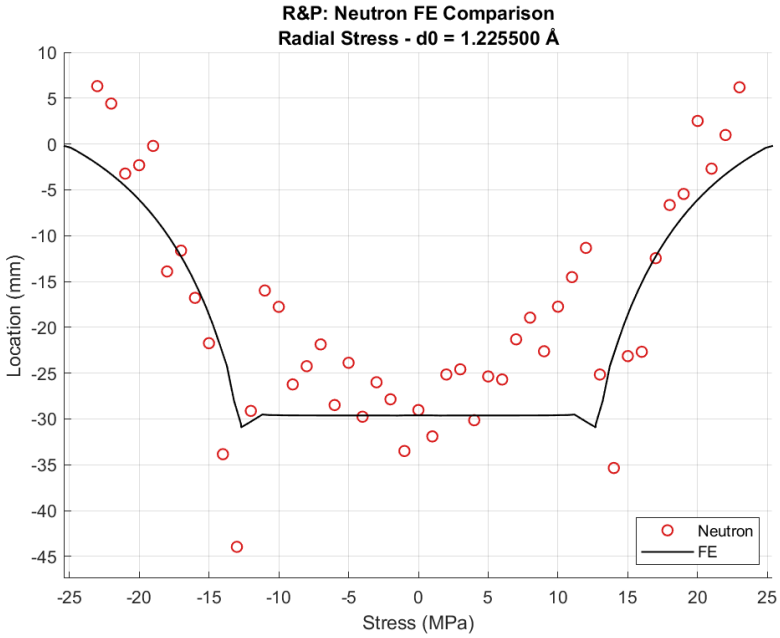


Figure 46: Neutron Radial Stress

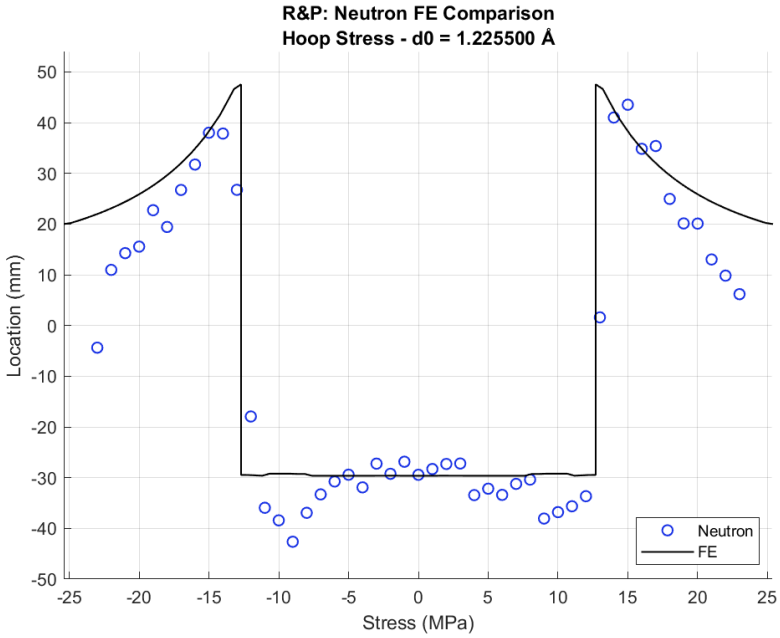


Figure 47: Neutron Hoop Stress

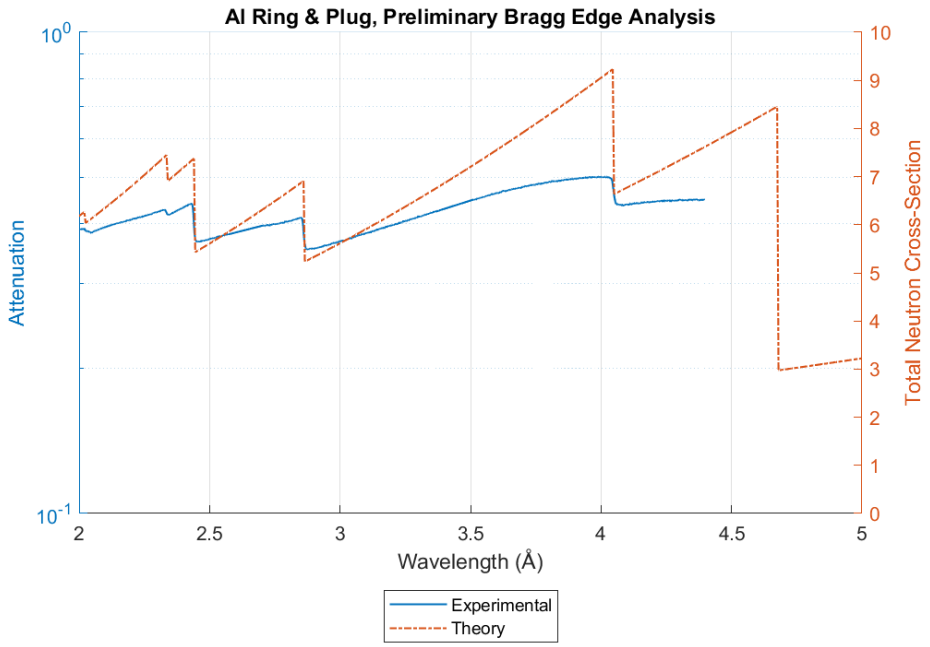


Figure 48: Ring & Plug Bragg Edge Results Compared to Theory

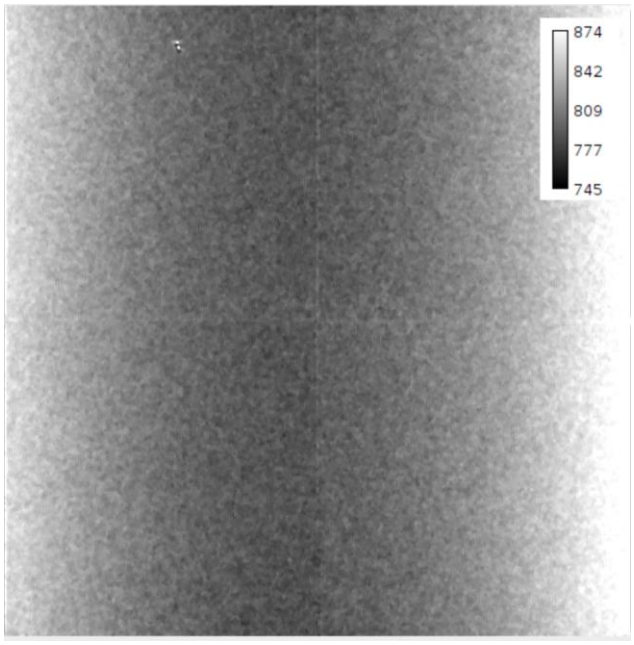


Figure 49: Grey Scale Summed Across Wavelength Range, Radiograph

concluded that these effects were artificial. Based on this conclusion, the artificial defects were removed from the profile in comparison to other measurement techniques.

Incremental Hole Drilling

In this study, three incremental hole drilling residual stress measurement techniques were performed. 3D DIC was used for analysis with the radial displacement and integral methods, and the conventional strain gauge rosettes were used for an integral method analysis. All three results were in good agreement after a statistical analysis was performed. Of most prominent note, the radial displacement method greatly undermeasured negative stresses in the sample. Prior to implementation here, the radial displacement method was calibrated with several 4-point bending tests and showed great accuracy. Statistical analysis of average standard deviations between all tests was performed and is represented with the error bars in Figure 43. This analysis showed that the minimum stresses measured with the radial displacement method are statistically closer to the expected finite element profile that initially observed.

The DIC integral method is also presented here as it is a more conventional method of calculating residual stress from DIC IHD measurements. The DIC integral method results better captured the negative stresses in both the ring and the plug. The average standard deviation for the DIC integral method results is higher due to variability in the calculated stress profile. The maximum stresses calculated with the DIC integral method however were much higher than those calculated by the radial displacement method. Another limitation with the DIC integral method results was the availability of smooth strain profiles. For several measurement points, there were not enough smooth strain profiles to create a usable rosette assembly. Therefore, DIC integral method analyses were not applicable at every DIC measurement location. It is concluded in this study that the radial displacement method was more consisted in calculating a uniform stress profile, and overall, better matched the expected stress profiles.

Residual stress measurements with conventional IHD strain gauge rosettes were performed at two locations in the ring of the sample. These results were in good agreement with the maximum and minimum stresses calculated with the DIC radial displacement method. It should be noted here that the conventional strain gauge rosettes also did not calculate the low magnitude compressive stresses in the ring of the sample. At the IHD measurement locations, the compressive stresses were approximately -10 and -2 MPa, which are relatively low for IHD residual stress measurements.

A successful comparison of three separate IHD residual stress measurement techniques is presented here. The DIC radial displacement method was of most interest to this study as it had previously shown great accuracy in calculating uniform residual stresses. The radial displacement method accurately calculated the tensile residual stresses in the ring, with fewer outlying data points than the DIC integral method results. For DIC radial displacement IHD measurements, it has previously been verified by finite element analysis that the method can be applied to residual stresses in aluminum equal to and greater than 50 MPa based on the typical DIC noise floor. All stresses measured in the aluminum 7050 ring and plug assembly were below this value, likely contributing to the measurement errors. Even with this limitation, the DIC radial displacement method of calculating residual stress was compatible with DIC integral method and conventional strain gauge rosette method. It can therefore be concluded that the DIC radial displacement method of calculating residual stress with IHD was successful for this ring & plug sample with the technique's limitations.

X-Ray Diffraction

The magnitude of x-ray diffraction results on the ring and plug assembly were very far from those of the finite element expected stress profile. It is hypothesized in this study that this is a direct result of the manufacturing of the aluminum 7050, and the heating and cooling cycles implemented for the ring and plug assembly. Aluminum 7050 is often subject to high compressive stresses at shallow depths into the material. A study presented in ASM international 2023 [28] explored surface level residual stresses in

aluminum 7050. The stresses published in [28] are of the same magnitude of the residual stresses measured by XRD in this study. It is proposed here that residual stress levels near the surface of the part are controlled by micro stresses that are influenced by the machining and manufacturing of the aluminum 7050. As the depth into the part increases, the stresses better resemble those proposed by finite element analysis where bulk residual stresses control. For the XRD $Sin^2 X$ analysis, the stresses are measured at depths of ~0.1 to 0.025mm. At available locations, the DIC integral method results at earliest depth of 0.025mm were compared here to the XRD results. The early DIC integral method results were of the same magnitude as the XRD results, supporting the idea that stress at this level is controlled by those induced by machining and heating cooling cycles.

Neutron Diffraction

Bulk neutron diffraction residual stress measurements were successfully performed for this sample. The neutron diffraction residual stress measurements presented here were the result of two approximations. Axial strain measurements were not performed for this sample, and hoop and radial stresses were calculated from the assumption that axial stresses are low as shown in finite element profiles. The approximate stresses follow the expected trends very well, supporting the assumption of low axial stress. The second assumption was the unstrained d spacing of the aluminum 7050 alloy. The unstrained d spacing used in strain and following stress calculations was approximated based on the d spacings measured closes to the edge of the sample in the radial direction where stresses go to zero. The average of these d spacings in the radial and hoop directions was 1.2255 Å and this value was used as the unstrained d spacing here. This proved to be a sound approximation as the radial and hoop stresses fit the expected profile well.

The bulk neutron diffraction residual stress measurements successfully fit the expected profile, even with the two state approximations. These measurements were performed at half of the sample height far from free edges. These results fit the expected trends more uniformly than DIC and XRD. The XRD measurements were made near the surface of the sample as discussed previously. It can be observed in these results that measurements

through the bulk of the sample are more accurate and freer from manufacturing defects in comparison to XRD. As stated earlier, the stress levels of this part were below the known accurate level of the DIC radial displacement method. For these small stresses it can therefore be concluded that neutron diffraction is the superior choice of residual stress measurements of the performed methods here.

Bragg Edge Imaging

Preliminary Bragg edge results were successful in determining the location of Bragg edges in the aluminum ring and plug sample. The agreeable comparison to theory indicates future ability to replicate the data at multiple radial positions around the sample. With limited view of the sample, it will be of utmost interest to verify the symmetry of the Bragg edges at all radial positions. With this replication, comprehensive analysis of the strain field through the sample is achievable. A visualization of the sample from neutron imaging shows details of neutron interaction with Bragg edges throughout the sample. Complete analysis of the sample will provide insight into strain fields. These preliminary results show great promise in the application of Bragg edge imaging to residual stress and strain measurements. For new and emerging neutron techniques, it is advantageous to have a known sample for calibration purposes. A shrink fit ring and plug sample as presented here is an ideal candidate for routine checks of neutron measurement setups. With cumulative technique results presented in this study, the ring and plug can be used to ensure neutron imaging setup and accuracy.

Conclusions

A variety of successful residual stress measurement techniques are presented here for comparison of an aluminum 7050 alloy ring and plug assembly. Measurement techniques included finite element analysis, three incremental hole drilling analyses, grazing incident XRD, bulk neutron diffraction, and neutron imaging. Each respective measurement was successful in measuring the induced residual stress at different spatial locations on the sample. Finite element analysis proved to be a valid method of determining stresses induced through the assembly of a part. These results provided a baseline of expected

values for comparison to other methods. While artificial defects were found, it was proven that the overall trends of induced stresses could be determined while keeping computational times low. Incremental hole drilling was performed on the ring and plug for its wide use in engineering application. The IHD results successfully captured the bulk uniform stresses at low depth into the part. Of the three explored techniques (strain gauge rosette integral method, DIC radial displacement method, and DIC integral method) the DIC radial displacement method was the most consistent and had less variability than the DIC integral method from a standard deviation consideration. Grazing incidence XRD was performed at 0.1 to 0.25mm into the part. The XRD results had large negative magnitudes that varied from the expected finite element profile. This is assumed to be due to manufacturing effects of the aluminum alloy and from heating and cooling cycles implemented for part assembly. Neutron diffraction was performed through the bulk of the sample, and two assumptions were made about the stress state and unstrained lattice spacing of the sample. Even with these assumptions, the neutron diffraction radial and hoop stresses accurately followed the finite element profile. Preliminary neutron imaging and Bragg edge analyses were also performed in this study to evaluate imaging techniques on the ring and plug sample. The initial results were promising and future tests to validate symmetry conditions will be performed. The neutron imaging technique is advantageous for complete strain field analysis on samples of interest.

Each method proved to have benefits for both accuracy and real-world applications. Incremental hole drilling can be performed in house and as part of the manufacturing process and provides useful information about the bulk stress present in the sample. The DIC radial displacement method was consistent and applicable to uniform and non-uniform residual stresses. Grazing incidence XRD provided critical information about the near surface stresses likely due to manufacturing and part assembly. This is beneficial to the development of new additively manufactured materials. Bulk neutron diffraction proved highly accurate through the thickness of the sample and provides a surplus of data points. This is advantageous when a comprehensive stress analysis is of interest for unique samples. With Bragg edge and neutron imaging analysis, the comprehensive

strain and stress field can be further analyzed when of interest. All methods are compared here to provide useful guidance on which residual stress measurement method is of most interest and use to the engineering industry.

Acknowledgements

Thank you to my advisor, Dr. Penumadu, for assistance and support with this project. Thank you to Dr. Jeff Bunn for the extensive mentoring on neutron diffraction and for completing the neutron diffraction measurements at ORNL. Thank you also to Dr. Hassina Bilheux for completing and providing neutron and Bragg edge imaging results, and for the time taken to mentor on these respective topics. Thank you to Dr. Penumadu for providing me with these connections and for guidance on diffraction residual stress measurements.

CONCLUSIONS

In this research, a comprehensive analysis of incremental hole drilling with integrated three-dimensional digital image correlation was performed. The application of the integral method and a newly developed radial displacement method were explored for 3D DIC IHD residual stress measurement. Extensive finite element analyses were completed to determine required calibration coefficients for the radial displacement method. The resulting calibration coefficients were used on aluminum, steel, and titanium finite element models with varying plate thicknesses. For the investigated materials, conclusions were made on the applicability of the radial displacement method based on the typical DIC noise floor. It was found that for aluminum plates, radial displacements at distances of 1.5 and 2.0r-r0 are most accurate. For steel, it was found that radial displacements at 1.5r-r0 are most accurate, and caution and engineering judgment should be implemented at early hole depths. Radial displacements at all investigated distances (1.5, 2.0, 2.5 and 3.0r-r0) are accurate in measuring residual stress with integrated DIC for titanium samples. The finite element results were successful and found the radial displacement method accurately measured uniform stresses. Based on the nature of their derivation, the radial displacement method of calculating residual stress can be applied to non-uniform stress distributions. Four-point bending tests were performed to validate the DIC radial displacement method and for direct comparison to the DIC and conventional strain gauge rosette integral methods. Four-point bending experiments were performed in a fixture with constant applied stress and in a fixture where stress varies across the hole drilling area. In both cases, the DIC radial displacement method was found to be more uniform and consistent than both DIC and strain gauge rosette integral methods. In this study, the DIC radial displacement method of measuring residual stress was found to be accurate and applicable to aluminum, steel, and titanium samples.

An aluminum 7050 ring and plug sample with diametral interference of 30 micron was subject to a variety of residual stress measurement methods. Finite element analysis of the ring and plug assembly provided expected stress profiles through the width of the

sample. In direct relation to work in the first chapter of this thesis, IHD with DIC and strain gauge rosette measurement was performed at radial locations on the sample. From IHD, residual stress was calculated with the DIC integral and radial displacement methods and with the integral method for strain gauge rosettes. The results of the strain gauge rosette and DIC radial displacement method were in good agreement, proving the DIC radial displacement method's validity. The DIC integral method was not applicable at all 10 measurement locations, due to non-uniform strain profiles. Where applicable, the DIC integral method better captured negative stresses throughout the sample. IHD residual stress measurements were successful, and it was found that the DIC radial displacement method results were more uniform and accurate than the DIC integral method results. Grazing incidence XRD was performed at the surface of the ring and plug assembly. These measurements yielded highly compressive residual stress results that did not agree with the finite element profile. It is hypothesized here that these results reflect residual stresses near the surface of the sample induced my manufacturing of the aluminum 7050 alloy and from cyclic heating and cooling during sample assembly. Bulk neutron diffraction measurements provided residual stress values far from free edges of the sample. These results are in good agreement with finite element expected values even with previously stated assumptions. Preliminary Bragg edge and neutron imaging analyses were performed here for limited comparison to traditional methods. The results were sound and showed great promise to wider applicability.

The work presented here provides a comprehensive analysis of residual stress measurement techniques with a focus on DIC IHD radial displacement method. The proposed radial displacement method is highly applicable to needs in the engineering community and takes advantage of ~270 measurement points. This method has been extensively compared to more conventional and widely accepted methods. It is concluded here that the radial displacement method is in good agreement with all compared measurements and improves on the measurement of a uniform stress profile. Analysis of a variety of residual stress measurements on an aluminum 7050 shrink fit ring and plug assembly is provided here to compare measurement techniques. It is the hope in this

study that these techniques are compared, and conclusions can be drawn by individual users to suit the needs of their specific applications.

LIST OF REFERENCES

[1] D. Furrer and N. B. Salah, “Overview of Residual Stresses from Manufacturing Processes,” in *Residual Stress Fundamentals*, D. Furrer, J. Pineault, and M. Hill, Eds., ASM International, 2025, pp. 1–3. doi: 10.31399/asm.hb.v25a.a0007127.

[2] G. S. Schajer, *Practical Residual Stress Measurement Methods*. Newark, UNITED KINGDOM: John Wiley & Sons, Incorporated, 2013. Accessed: Sept. 22, 2025. [Online]. Available: http://ebookcentral.proquest.com/lib/utk/detail.action?docID=1380176

[3] M. N. James, “Residual stress influences on structural reliability,” *Eng. Fail. Anal.*, vol. 18, no. 8, pp. 1909–1920, Dec. 2011, doi: 10.1016/j.engfailanal.2011.06.005.

[4] P. J. Withers and H. K. D. H. Bhadeshia, “Residual stress. Part 1 – Measurement techniques,” *Mater. Sci. Technol.*, vol. 17, no. 4, pp. 355–365, Apr. 2001, doi: 10.1179/026708301101509980.

[5] E28 Committee, *Test Method for Determining Residual Stresses by the Hole-Drilling Strain-Gage Method*. doi: 10.1520/E0837-20.

[6] D. V. Nelson, A. Makino, and T. Schmidt, “Residual Stress Determination Using Hole Drilling and 3D Image Correlation,” *Exp. Mech.*, vol. 46, no. 1, pp. 31–38, Feb. 2006, doi: 10.1007/s11340-006-5859-0.

[7] E. Arabul and A. J. G. Lunt, “A Novel Low-Cost DIC-Based Residual Stress Measurement Device,” *Appl. Sci.*, vol. 12, no. 14, p. 7233, July 2022, doi: 10.3390/app12147233.

[8] G. S. Schajer, “Hole-Drilling Residual Stress Measurements at 75: Origins, Advances, Opportunities,” *Exp. Mech.*, vol. 50, no. 2, pp. 245–253, Feb. 2010, doi: 10.1007/s11340-009-9285-y.

[9] D. Vangi and S. Tellini, “Hole-Drilling Strain-Gauge Method: Residual Stress Measurement With Plasticity Effects,” *J. Eng. Mater. Technol.*, vol. 132, no. 1, p. 011003, Jan. 2010, doi: 10.1115/1.3184030.

[10] N. J. Rendler and I. Vigness, “Hole-drilling strain-gage method of measuring residual stresses: Authors indicate that this method permits the magnitudes and

principal directions of residual stresses at the hole location to be determined," *Exp. Mech.*, vol. 6, no. 12, pp. 577–586, Dec. 1966, doi: 10.1007/BF02326825.

[11] G. S. Schajer, "Optical Hole-Drilling Residual Stress Calculations Using Strain Gauge Formalism," *Exp. Mech.*, vol. 61, no. 9, pp. 1369–1380, Nov. 2021, doi: 10.1007/s11340-021-00740-7.

[12] A. Makino and D. Nelson, "Residual-stress determination by single-axis holographic interferometry and hole drilling—Part I: Theory," *Exp. Mech.*, vol. 34, no. 1, pp. 66–78, Mar. 1994, doi: 10.1007/BF02328443.

[13] "Measurement of Non-Uniform Residual Stresses Usingthe Hole-Drilling Mehod. Part 1 - Stress Calculation Procedures."

[14] A. Baldi, "Residual Stress Measurement Using Hole Drilling and Integrated Digital Image Correlation Techniques," *Exp. Mech.*, vol. 54, no. 3, pp. 379–391, Mar. 2014, doi: 10.1007/s11340-013-9814-6.

[15] K. Atkinson, *Elementary Numerical Analysis*, 2nd edn. New York, NY: J. Wiley, 1993.

[16] *Abaqus Standard*.

[17] *Aramis Professional*. Trillion Quality Systems.

[18] *StrainSmart*. Vishay Precision Group.

[19] G. S. Schajer, *H-Drill*.

[20] M. T. Hutchings, P. J. Withers, T. M. Holden, and T. Lorentzen, *Introduction to the Characerization of Residual Stress by Neutron Diffraction*. BocaRaton, FL: CRC Press, 2005.

[21] A. Tabatabaeian, A. R. Ghasemi, M. M. Shokrieh, B. Marzbanrad, M. Baraheni, and M. Fotouhi, "Residual Stress in Engineering Materials: A Review," *Adv. Eng. Mater.*, vol. 24, no. 3, p. 2100786, Mar. 2022, doi: 10.1002/adem.202100786.

[22] R. Woracek, J. Santisteban, A. Fedrigo, and M. Strobl, "Diffraction in neutron imaging—A review," *Nucl. Instrum. Methods Phys. Res. Sect. Accel. Spectrometers Detect. Assoc. Equip.*, vol. 878, pp. 141–158, Jan. 2018, doi: 10.1016/j.nima.2017.07.040.

[23] T. M. Holden, G. A. Webster, and R. C. Wimpory, “VAMAS - Neutron Diffraction Measurements of Residual Stress in a Shrink-Fit Ring & Plug,” 38, ISSN 1016-22186, Jan. 2000.

[24] B. D. Cullity and S. R. Stock, *Elements of X-Ray Diffractioin*, Third. UK: Pearson, 2014.

[25] “High Intensity Diffractometer for Residual Stress Analysis HIDRA | HB-2B | HFIR,” Oak Ridge National Laboratory, Oct. 2024. Accessed: Oct. 16, 2024. [Online]. Available: https://neutrons.ornl.gov/hidra

[26] C. M. Fancher *et al.*, “*pyRS* : a user-friendly package for the reduction and analysis of neutron diffraction data measured at the High Intensity Diffractometer for Residual Stress Analysis,” *J. Appl. Crystallogr.*, vol. 54, no. 6, pp. 1886–1893, Dec. 2021, doi: 10.1107/S1600576721010554.

[27] “Versatile Neutron Imaging Instrument VENUS | BL-10 | SNS,” Oak Ridge National Laboratory, Oct. 2024. Accessed: Oct. 18, 2024. [Online]. Available: https://neutrons.ornl.gov/venus

[28] M. Zhang, K. Gu, Z. Weng, C. Cui, and J. Wang, “Residual Stress Evolution of 7050 Aluminum Alloy during Thermal Processing and Its Effects on Processing Deformation and Mechanical Properties,” *J. Mater. Eng. Perform.*, vol. 33, no. 21, pp. 11467–11483, Nov. 2024, doi: 10.1007/s11665-023-08816-2.

APPENDIX

Chapter 1: Finite Element Analysis Results

Table 4: a Values for IHD Depths of 2.0mm Diameter Hole, 4mm Thick Model

a Values, 20x20x4mm Plate				
Depth (mm)	1.5 r/r_0	2.0 r/r_0	2.5 r/r_0	3.0 r/r_0
0.05	0.007115	0.010964	0.011428	0.00094
0.1	0.042971	0.016743	0.021069	0.008133
0.15	0.091524	0.032261	0.02943	0.018208
0.2	0.134416	0.051475	0.037466	0.026749
0.25	0.181702	0.076893	0.048834	0.036165
0.3	0.220844	0.100691	0.060506	0.044549
0.35	0.262287	0.128285	0.07552	0.054517
0.4	0.295976	0.152222	0.089605	0.063692
0.45	0.331267	0.17871	0.10634	0.074619
0.5	0.359796	0.20107	0.121276	0.084533
0.55	0.389637	0.225357	0.138341	0.096133
0.6	0.413744	0.245586	0.153145	0.106448
0.65	0.438939	0.267334	0.169677	0.118284
0.7	0.459201	0.285248	0.183754	0.128615
0.75	0.480531	0.304495	0.199303	0.140311
0.8	0.497819	0.320369	0.212448	0.150412
0.85	0.515968	0.337321	0.226825	0.161703
0.9	0.530614	0.351202	0.238839	0.171318
0.95	0.545831	0.365845	0.251773	0.181873
1	0.557695	0.377652	0.26269	0.191221

Table 5: b Values for IHD Depths of 2.0mm Diameter Hole, 4mm Thick Model

b Values, 20x20x4mm Plate				
Depth (mm)	1.5 r/r_0	2.0 r/r_0	2.5 r/r_0	3.0 r/r_0
0.05	0.030693	0.024323	0.022889	0.005816
0.1	0.098493	0.041624	0.043524	0.019975
0.15	0.189443	0.075028	0.063429	0.040057
0.2	0.271843	0.11371	0.081918	0.057924
0.25	0.365388	0.16452	0.106747	0.078122
0.3	0.445492	0.21267	0.131562	0.096276
0.35	0.533089	0.269639	0.163234	0.117895
0.4	0.606727	0.320229	0.193077	0.137828
0.45	0.686317	0.377594	0.228928	0.161669
0.5	0.752751	0.427279	0.261404	0.183442
0.55	0.824367	0.482634	0.299151	0.209163
0.6	0.884015	0.529944	0.332513	0.232299
0.65	0.948248	0.58213	0.370509	0.259207
0.7	1.00153	0.62628	0.403546	0.283048
0.75	1.05922	0.674899	0.44078	0.310449
0.8	1.107338	0.716032	0.472923	0.334505
0.85	1.1594	0.76115	0.508882	0.361889
0.9	1.202756	0.799154	0.539676	0.385701
0.95	1.249559	0.840653	0.573852	0.412564
1	1.286485	0.873868	0.601763	0.434927

Table 6: a Values for IHD Depths of 2.0mm Diameter Hole, 15mm Thick Model

a Values, 20x20x15mm Plate				
Depth (mm)	1.5 r/r_0	2.0 r/r_0	2.5 r/r_0	3.0 r/r_0
0.05	0.021666	0.005381	0.012829	0.002753
0.1	0.066853	0.020463	0.016926	0.010101
0.15	0.118352	0.048024	0.027424	0.017177
0.2	0.15496	0.072824	0.04049	0.025234
0.25	0.191411	0.099543	0.05703	0.035958
0.3	0.219602	0.121108	0.071759	0.045955
0.35	0.247393	0.14312	0.087909	0.057453
0.4	0.268916	0.160612	0.10132	0.067392
0.45	0.290288	0.178402	0.115468	0.078273
0.5	0.306959	0.192523	0.126987	0.087385
0.55	0.323679	0.206922	0.139007	0.097148
0.6	0.336672	0.218257	0.148647	0.10514
0.65	0.349693	0.229771	0.158618	0.113578
0.7	0.36018	0.23911	0.166791	0.120582
0.75	0.370974	0.248805	0.175376	0.128039
0.8	0.379612	0.256617	0.182361	0.134176
0.85	0.388572	0.264778	0.189726	0.140718
0.9	0.395787	0.271389	0.195739	0.146106
0.95	0.40328	0.278301	0.202079	0.151838
1	0.408749	0.28342	0.206848	0.156215

Table 7: b Values for IHD Depths of 2.0mm Diameter Hole, 15mm Thick Model

b Values, 20x20x15mm Plate				
Depth (mm)	1.5 r/r_0	2.0 r/r_0	2.5 r/r_0	3.0 r/r_0
0.05	0.048799	0.016915	0.025658	0.007643
0.1	0.131583	0.04679	0.037797	0.023133
0.15	0.231735	0.100026	0.060191	0.038841
0.2	0.308339	0.150865	0.087075	0.05595
0.25	0.388989	0.208118	0.122148	0.07851
0.3	0.454372	0.256484	0.154334	0.099977
0.35	0.521849	0.308098	0.190895	0.125383
0.4	0.576271	0.350706	0.222266	0.147935
0.45	0.632572	0.395739	0.25651	0.173348
0.5	0.678038	0.43266	0.285216	0.195167
0.55	0.725349	0.471621	0.316124	0.219197
0.6	0.763362	0.503265	0.341623	0.239365
0.65	0.80289	0.536528	0.36883	0.261247
0.7	0.835438	0.564082	0.39158	0.279743
0.75	0.869924	0.593482	0.416089	0.299901
0.8	0.898163	0.61769	0.436438	0.316794
0.85	0.928348	0.64371	0.458469	0.335238
0.9	0.953243	0.66527	0.476836	0.35073
0.95	0.979979	0.688539	0.496788	0.367672
1	1.001269	0.707209	0.512917	0.381481

Table 8: a Values for IHD Depths of 2.0mm Diameter Hole, 20mm Thick Model

a Values, 20x20x20mm Plate				
Depth (mm)	1.5 r/r_0	2.0 r/r_0	2.5 r/r_0	3.0 r/r_0
0.05	0.022076	0.005447	0.013374	0.00255
0.1	0.066806	0.020644	0.017528	0.010066
0.15	0.118063	0.048317	0.028105	0.017296
0.2	0.154455	0.073254	0.041199	0.025586
0.25	0.19054	0.099882	0.057759	0.036494
0.3	0.218573	0.121389	0.072503	0.046608
0.35	0.245963	0.143139	0.088557	0.058139
0.4	0.267234	0.160444	0.101886	0.068083
0.45	0.288196	0.177916	0.115845	0.078891
0.5	0.304591	0.191807	0.127216	0.087938
0.55	0.320917	0.205875	0.139002	0.097562
0.6	0.333778	0.217081	0.148545	0.105503
0.65	0.346419	0.228258	0.158247	0.113756
0.7	0.356595	0.237317	0.166196	0.120598
0.75	0.367042	0.246699	0.174521	0.12786
0.8	0.375416	0.254267	0.181296	0.133832
0.85	0.384083	0.262155	0.188426	0.140187
0.9	0.391073	0.268551	0.194246	0.145419
0.95	0.398345	0.275249	0.200398	0.150997
1	0.40385	0.280379	0.205168	0.155383

Table 9: b Values for IHD Depths of 2.0mm Diameter Hole, 20mm Thick Model

b Values, 20x20x20mm Plate				
Depth (mm)	1.5 r/r_0	2.0 r/r_0	2.5 r/r_0	3.0 r/r_0
0.05	0.049758	0.017001	0.026236	0.00741
0.1	0.132298	0.047353	0.038532	0.023074
0.15	0.232254	0.101165	0.061286	0.039087
0.2	0.308733	0.152464	0.088497	0.056659
0.25	0.389041	0.20985	0.12394	0.079683
0.3	0.454248	0.258293	0.156394	0.101522
0.35	0.521141	0.309669	0.193062	0.127211
0.4	0.575115	0.352054	0.22447	0.149951
0.45	0.630716	0.396657	0.258586	0.175449
0.5	0.67563	0.433209	0.287154	0.197305
0.55	0.722209	0.47165	0.317795	0.221263
0.6	0.759921	0.503074	0.343206	0.24146
0.65	0.798663	0.535723	0.370009	0.26314
0.7	0.830526	0.562737	0.392396	0.281434
0.75	0.864275	0.591541	0.416489	0.301338
0.8	0.891914	0.615256	0.436475	0.317999
0.85	0.921383	0.640676	0.45806	0.336146
0.9	0.945677	0.661722	0.476032	0.351361
0.95	0.971776	0.68444	0.495553	0.367989
1	0.9929	0.702939	0.511551	0.381724

Table 10: a Values for IHD Depths of 2.0mm Diameter Hole, 30mm Thick Model

a Values, 20x20x30mm Plate				
Depth (mm)	1.5 r/r_0	2.0 r/r_0	2.5 r/r_0	3.0 r/r_0
0.05	0.032496	0.005015	0.012071	0.00487
0.1	0.080215	0.028382	0.018493	0.010407
0.15	0.125429	0.058299	0.034334	0.019839
0.2	0.15614	0.0822	0.049245	0.030526
0.25	0.185046	0.105172	0.065716	0.042772
0.3	0.206315	0.122427	0.078979	0.05297
0.35	0.226314	0.139002	0.092323	0.063599
0.4	0.241239	0.151573	0.102715	0.072104
0.45	0.255588	0.163843	0.113082	0.0808
0.5	0.266454	0.173232	0.121136	0.087677
0.55	0.277049	0.182481	0.129182	0.094663
0.6	0.284995	0.18948	0.135341	0.100087
0.65	0.292997	0.196571	0.141633	0.105687
0.7	0.299247	0.202135	0.146607	0.110145
0.75	0.305568	0.207794	0.151698	0.11475
0.8	0.310552	0.212274	0.15575	0.11844
0.85	0.315672	0.216898	0.159961	0.122297
0.9	0.31976	0.220606	0.163352	0.125426
0.95	0.323987	0.224459	0.166895	0.128715
1	0.32715	0.22737	0.169603	0.131253

Table 11: b Values for IHD Depths of 2.0mm Diameter Hole, 30mm Thick Model

b Values, 20x20x30mm Plate				
Depth (mm)	1.5 r/r_0	2.0 r/r_0	2.5 r/r_0	3.0 r/r_0
0.05	0.063655	0.015745	0.02529	0.010807
0.1	0.153216	0.059127	0.04023	0.02376
0.15	0.246054	0.119895	0.072197	0.043672
0.2	0.315094	0.171708	0.104241	0.066016
0.25	0.384328	0.224859	0.141508	0.092713
0.3	0.43815	0.267122	0.172911	0.116008
0.35	0.491505	0.309907	0.206014	0.141394
0.4	0.533172	0.343792	0.232863	0.162484
0.45	0.57504	0.378297	0.260739	0.184859
0.5	0.607925	0.405641	0.283127	0.203115
0.55	0.641251	0.433593	0.306296	0.222282
0.6	0.667237	0.455546	0.324668	0.237661
0.65	0.69422	0.47846	0.34399	0.25398
0.7	0.715854	0.496907	0.359645	0.267289
0.75	0.738469	0.516277	0.376171	0.281446
0.8	0.756802	0.532035	0.389681	0.29308
0.85	0.776317	0.548869	0.404179	0.305619
0.9	0.792394	0.56278	0.4162	0.316064
0.95	0.809755	0.577856	0.429275	0.327469
1	0.824001	0.590296	0.440116	0.336961

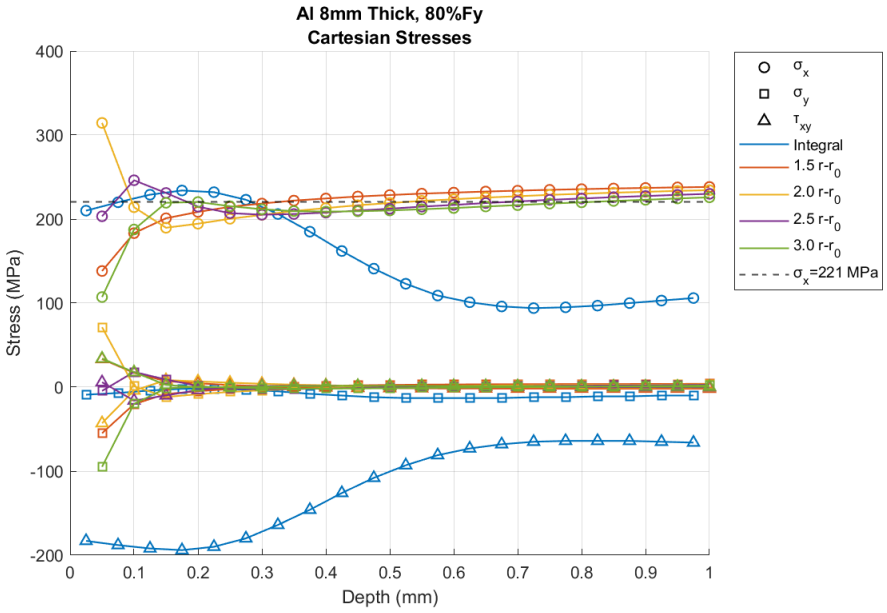


Figure 50: Cartesian Stresses, 8mm Thick Al Plate, 80% Fy Uniaxial Applied Stress, Radial Displacement and Integral Methods

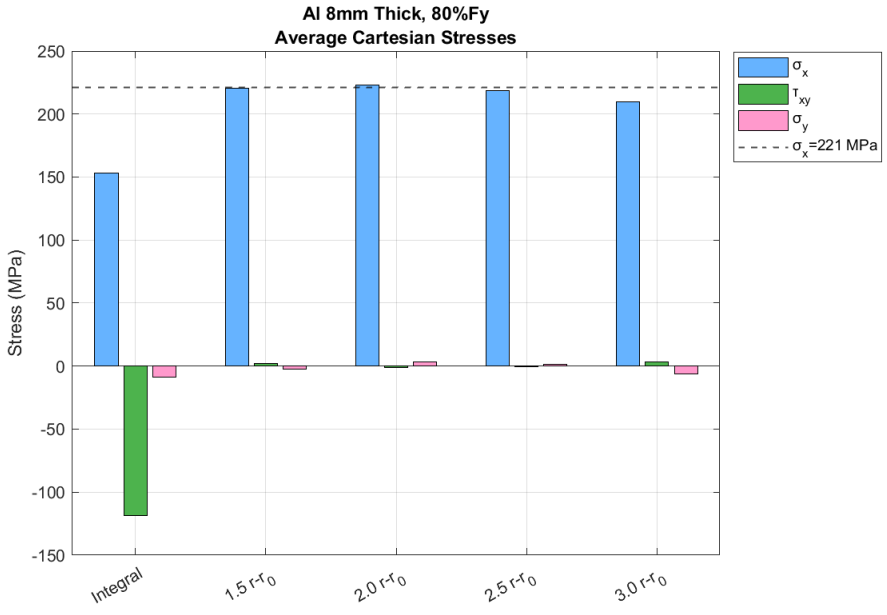


Figure 51: Average Cartesian Stresses, 8mm Thick Al Plate, 80% Fy Uniaxial Applied Stress, Radial Displacement and Integral Methods

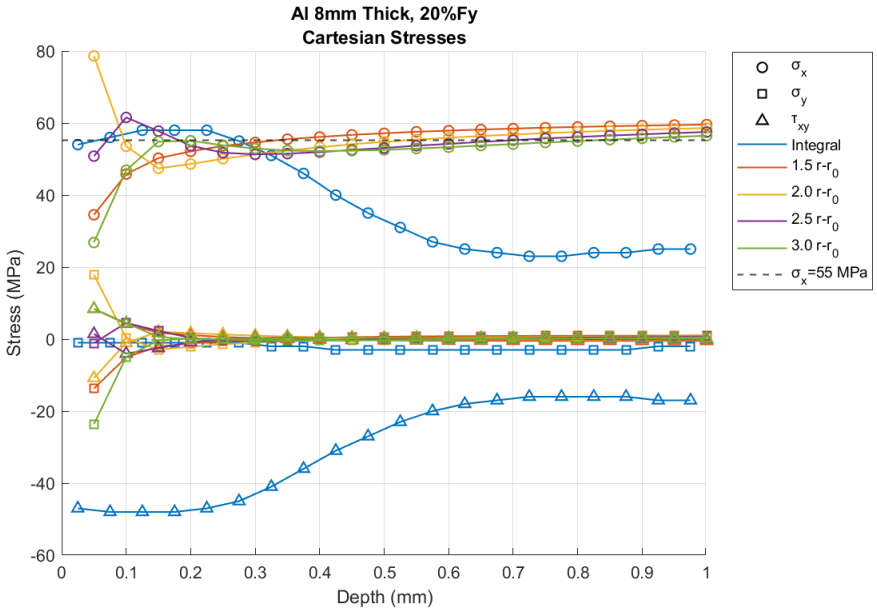


Figure 52: Cartesian Stresses, 8mm Thick Al Plate, 20% Fy Uniaxial Applied Stress, Radial Displacement and Integral Methods

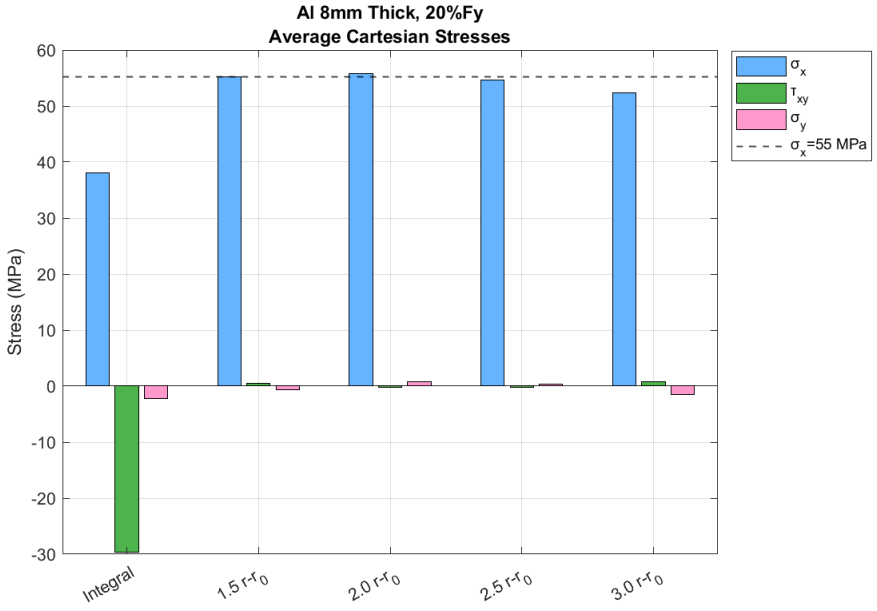


Figure 53: Average Cartesian Stresses, 8mm Thick Al Plate, 20% Fy Uniaxial Applied Stress, Radial Displacement and Integral Methods

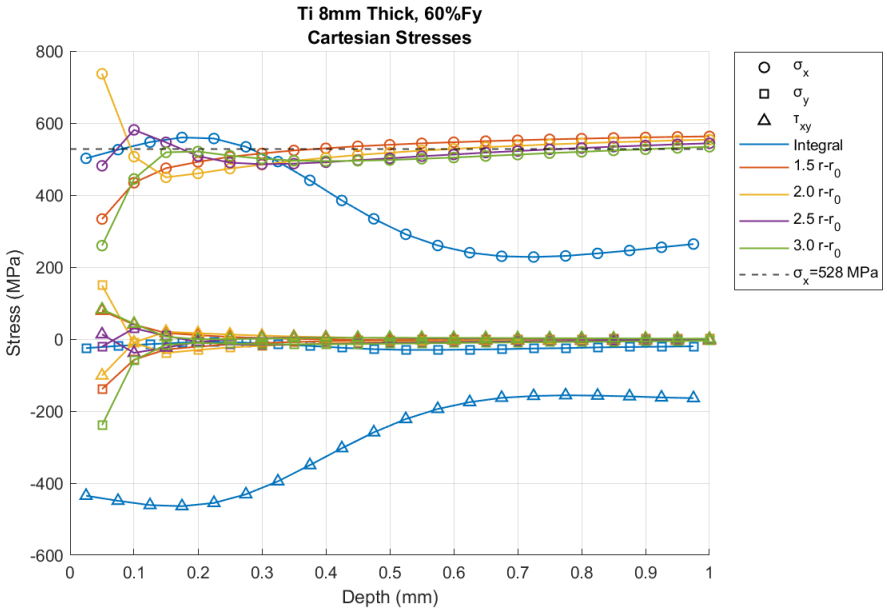


Figure 54: Cartesian Stresses, 8mm Thick Ti Plate, Radial Displacement and Integral Methods

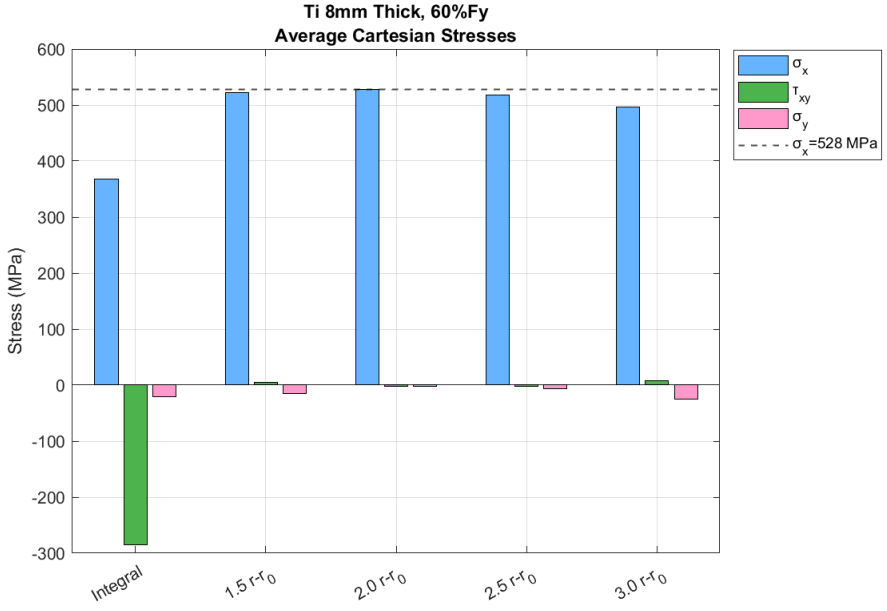


Figure 55: Average Cartesian Stresses, 8mm Thick Ti Plate, Radial Displacement and Integral Methods

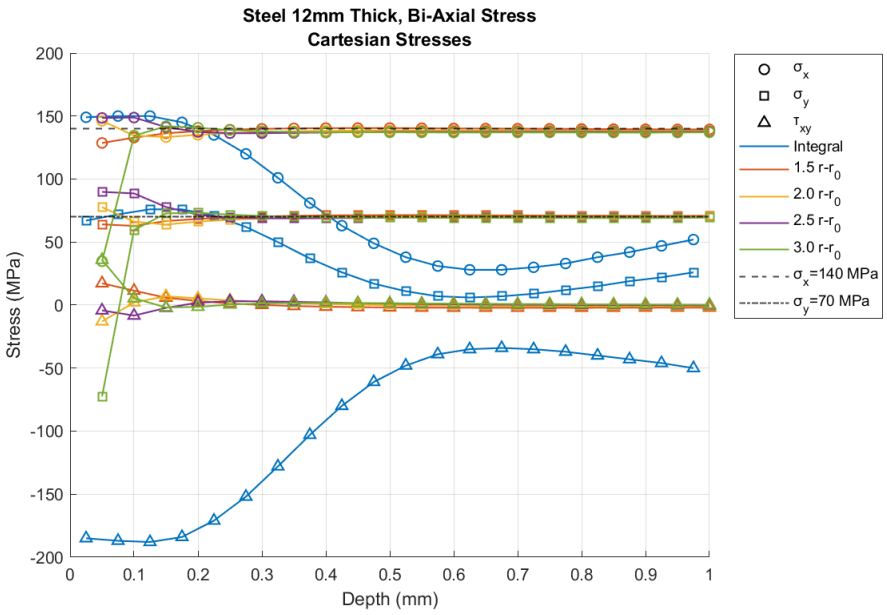


Figure 56: Cartesian Stresses, 12mm Thick Steel Plate, Radial Displacement and Integral Methods

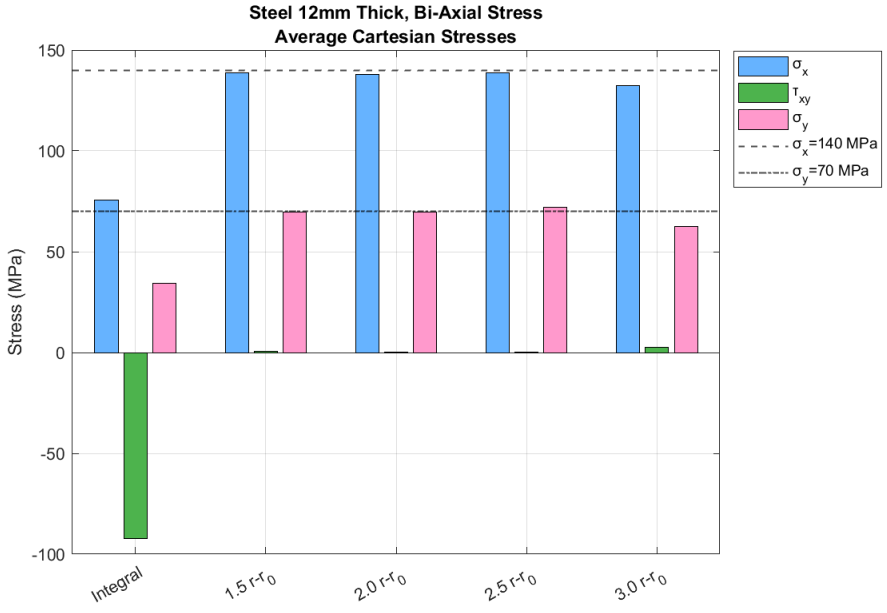


Figure 57: Average Cartesian Stresses, 12mm Thick Steel Plate, Radial Displacement and Integral Methods

Chapter 1: 4-Point Bending Results

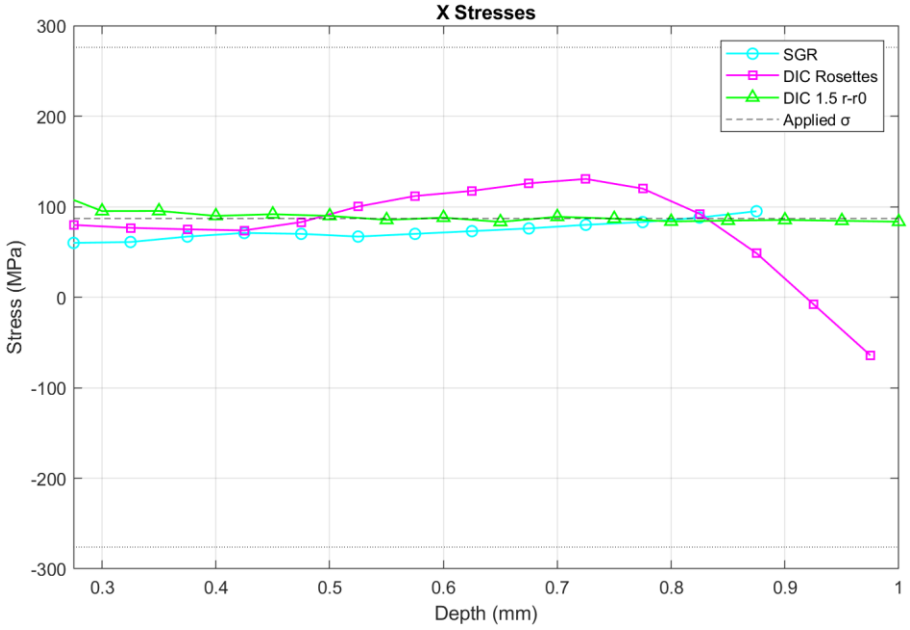


Figure 58: X Stress Profile Comparison, Out of Plane 4-pt Bending

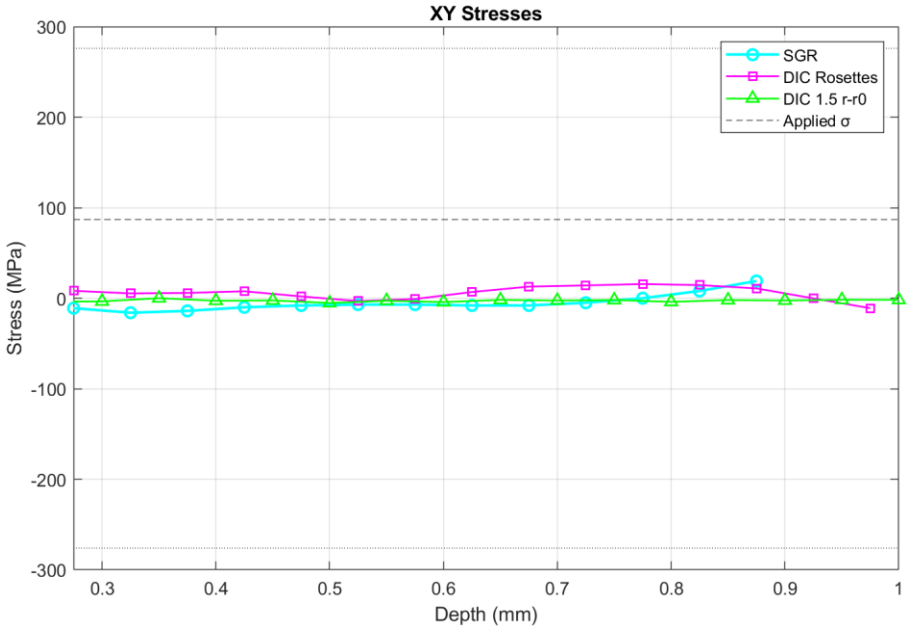


Figure 59: XY Stress Profile Comparison, Out of Plane 4-pt Bending

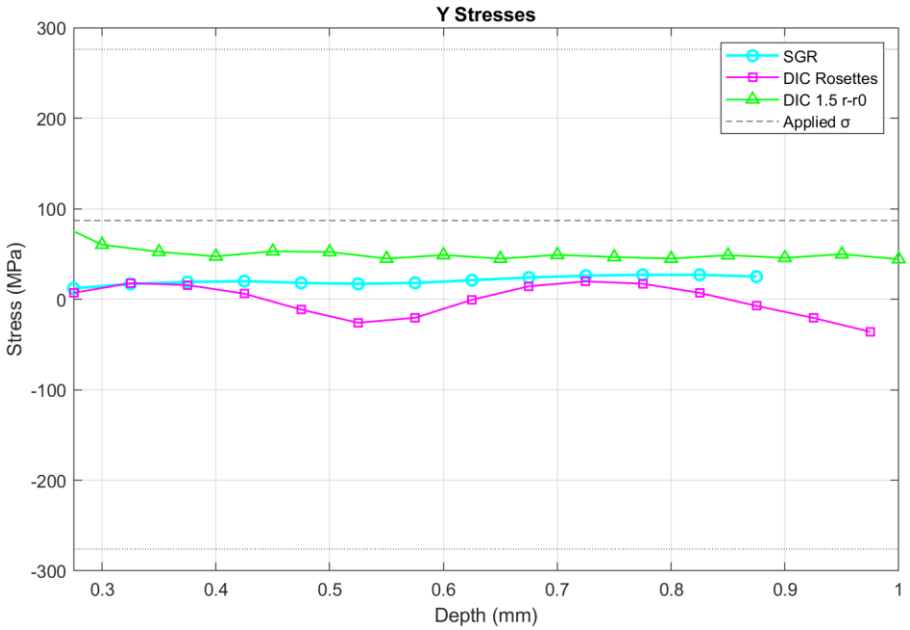


Figure 60: Y Stress Profile Comparison, Out of Plane 4-pt Bending

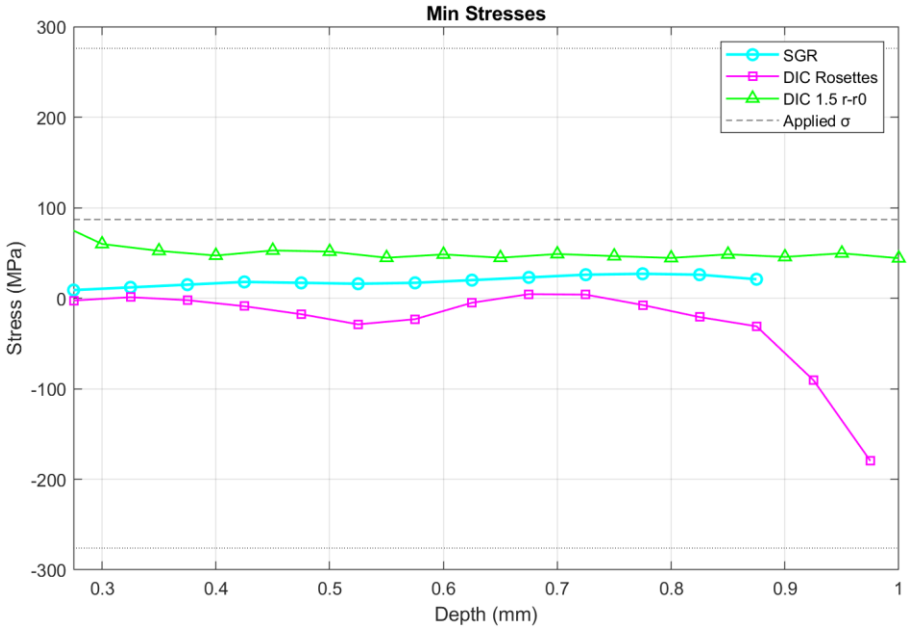


Figure 61: Minimum Stress Profile Comparison, Out of Plane 4-pt Bending

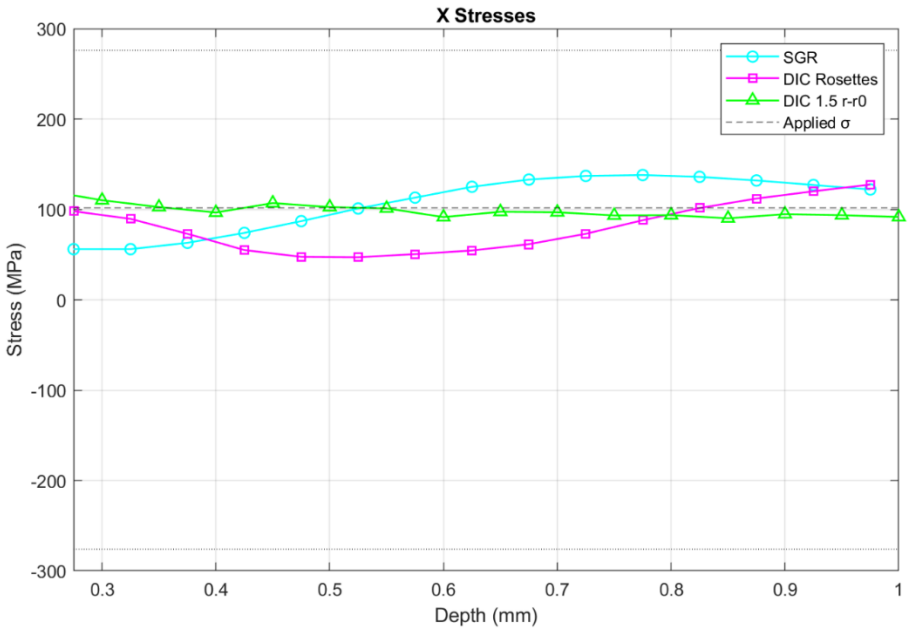


Figure 62: X Stress Profile Comparison, In Plane 4-pt Bending

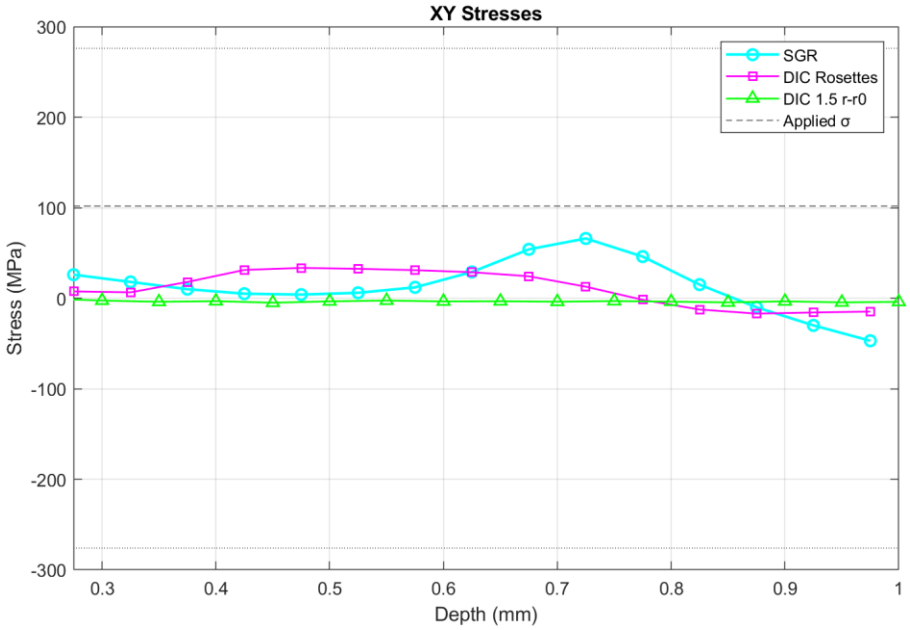


Figure 63: XY Stress Profile Comparison, In Plane 4-pt Bending

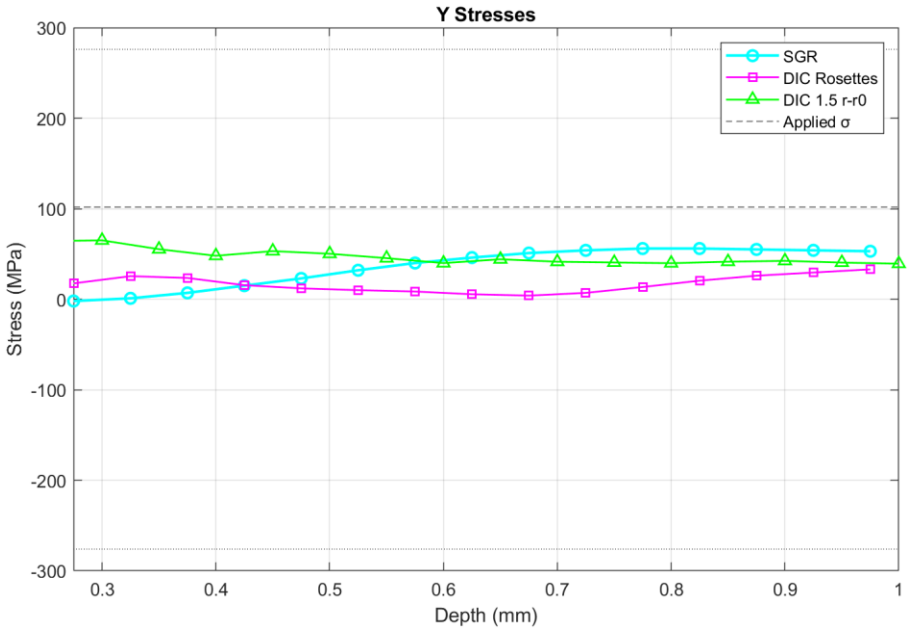


Figure 64: Y Stress Profile Comparison, In Plane 4-pt Bending

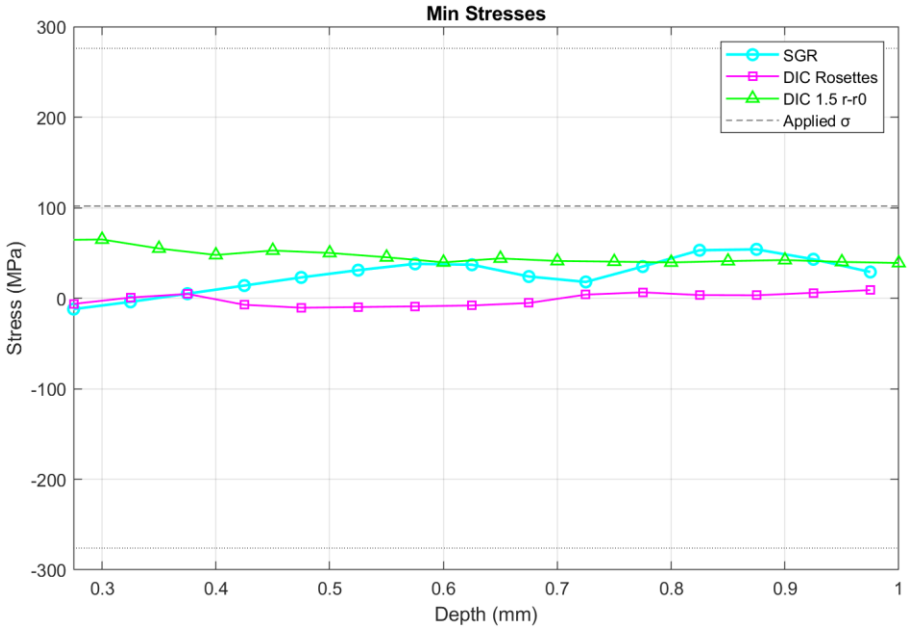


Figure 65: Minimum Stress Profile Comparison, In Plane 4-pt Bending

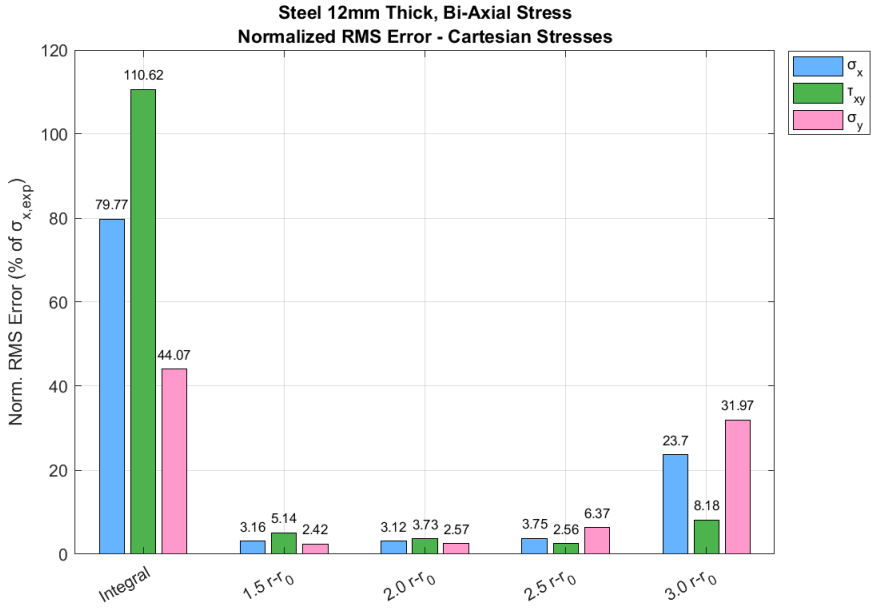


Figure 66: RMS Error, FE Cartesian Stress Results

Chapter 2: X-Ray Diffraction Ring & Plug Linear Fit Plots

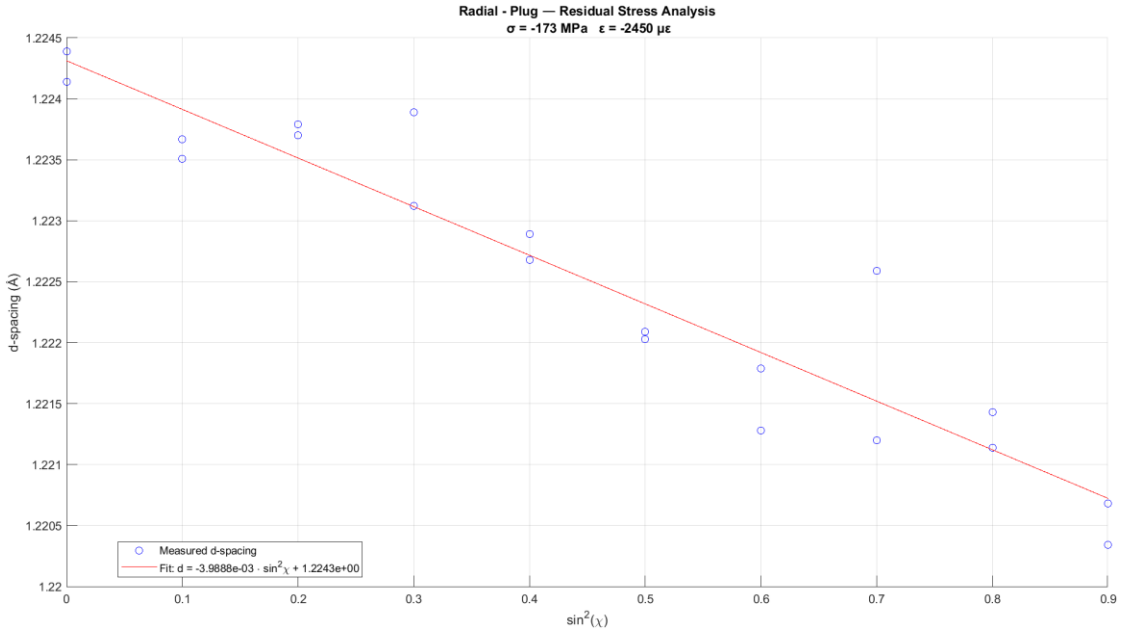


Figure 67: XRD Radial Plug Measurement d-spacing Sin^2 X linear at ¼ Radial Distance off Center

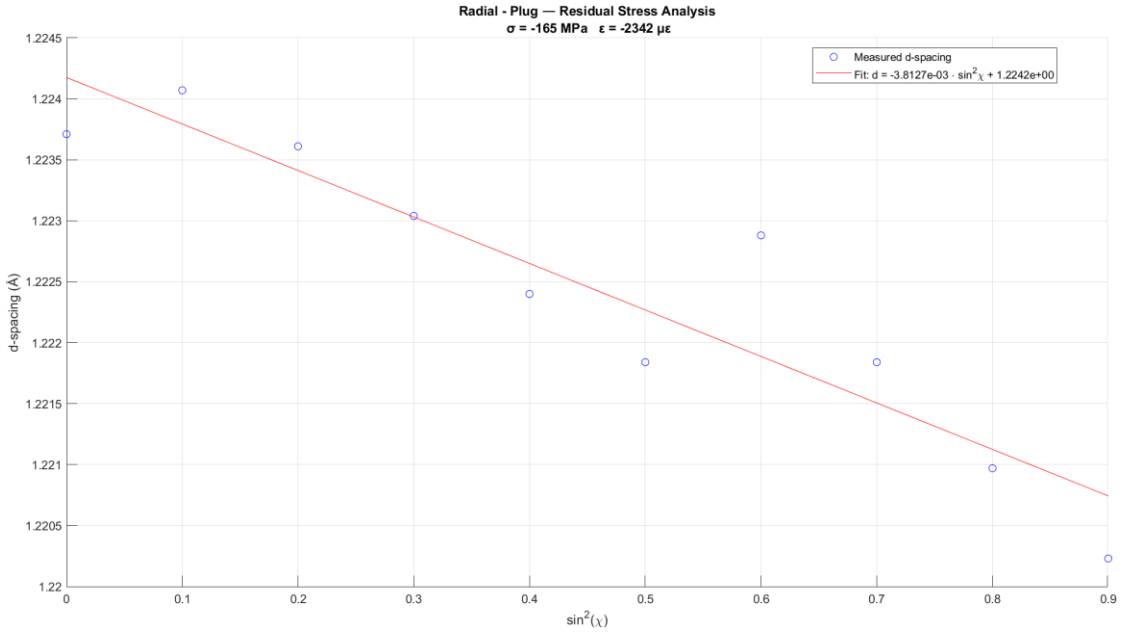


Figure 68: XRD Radial Plug Measurement d-spacing Sin^2 X linear at -¼ Radial Distance off Center

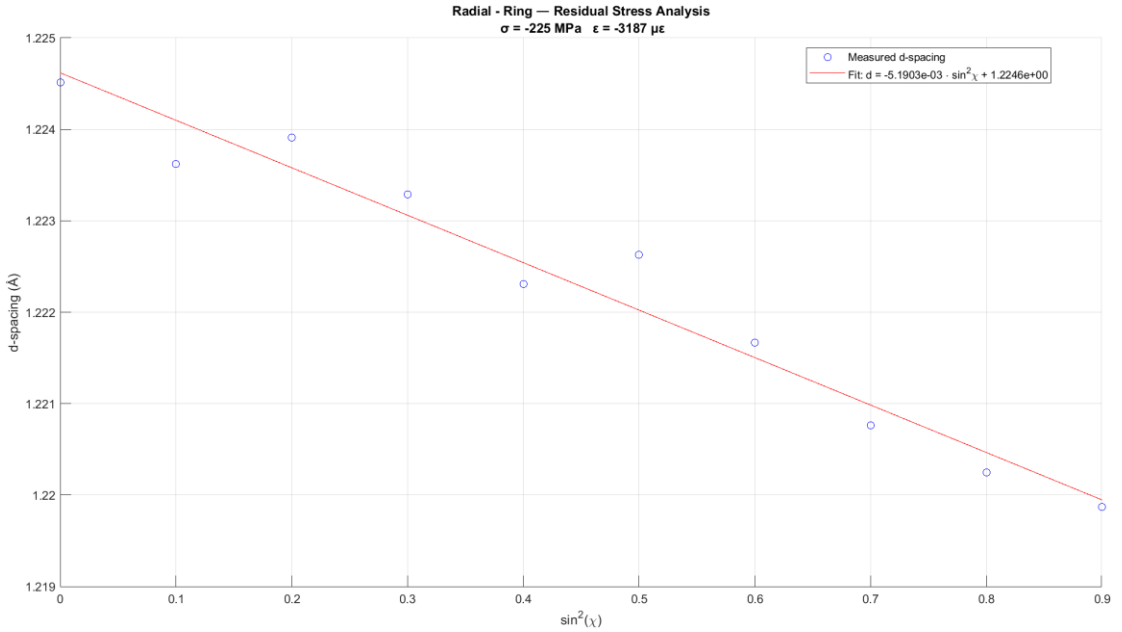


Figure 69: XRD Radial Ring Measurement d-spacing Sin^2 X linear at ¾ Radial Distance off Center

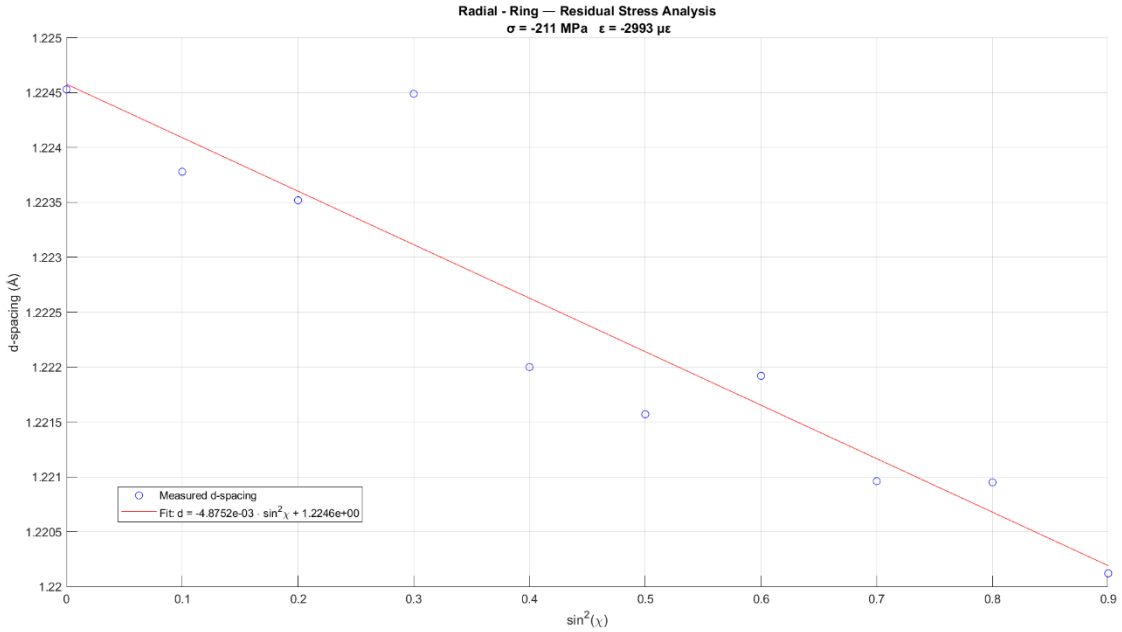


Figure 70: XRD Radial Ring Measurement d-spacing Sin^2 X linear at -¾ Radial Distance off Center

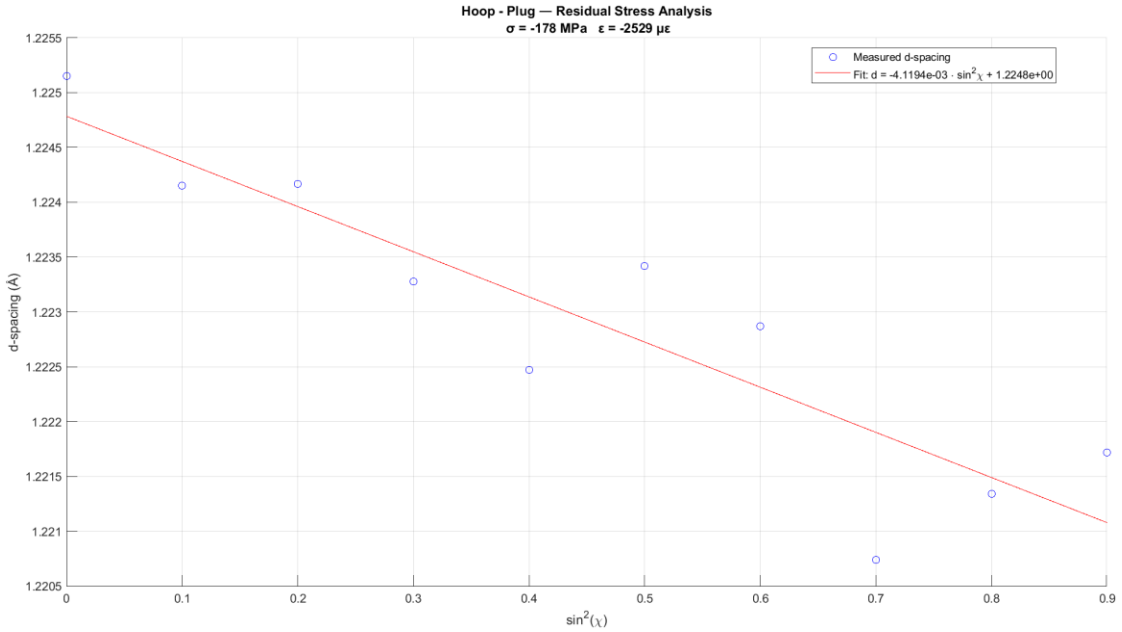


Figure 71: XRD Hoop Plug Measurement d-spacing Sin^2 X linear at ¼ Radial Distance off Center

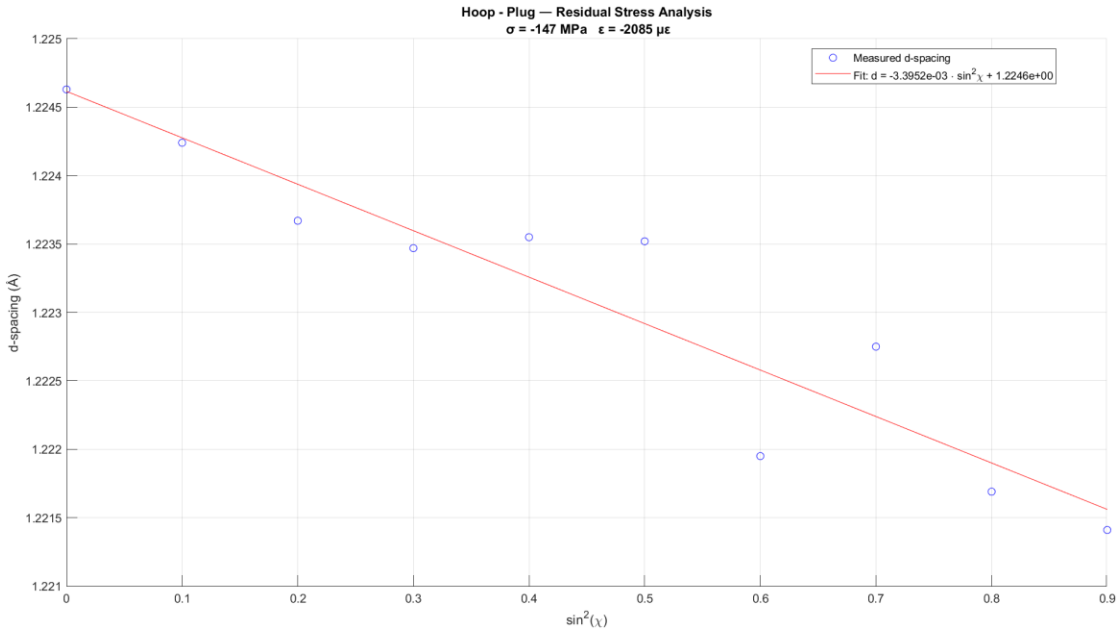


Figure 72: XRD Hoop Plug Measurement d-spacing Sin^2 X linear at -¼ Radial Distance off Center

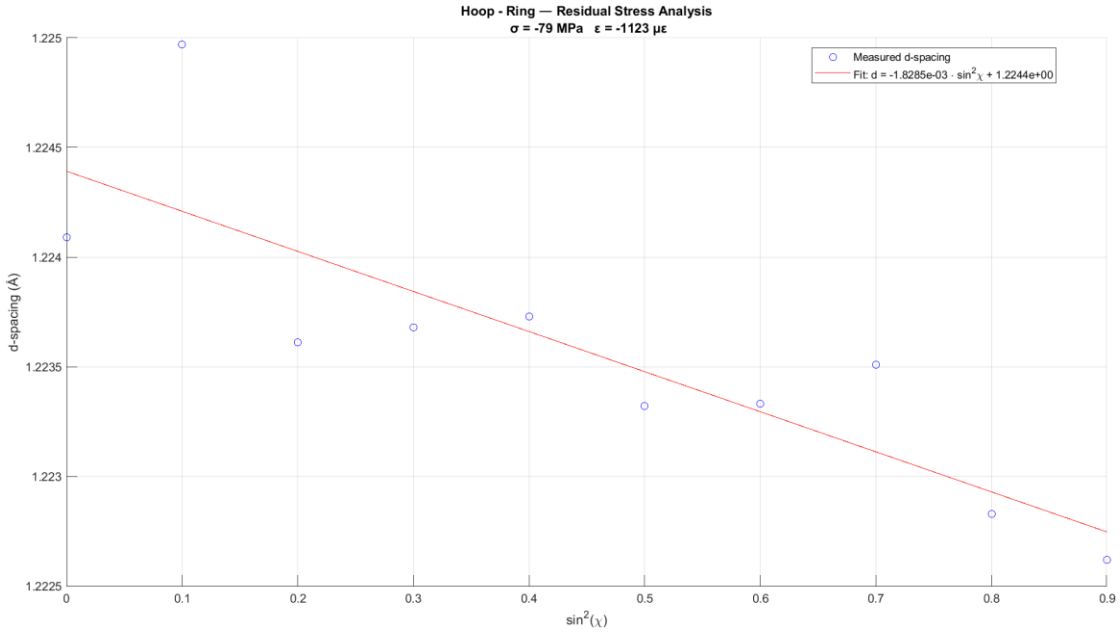


Figure 73: XRD Hoop Ring Measurement d-spacing Sin^2 X linear at ¾ Radial Distance off Center

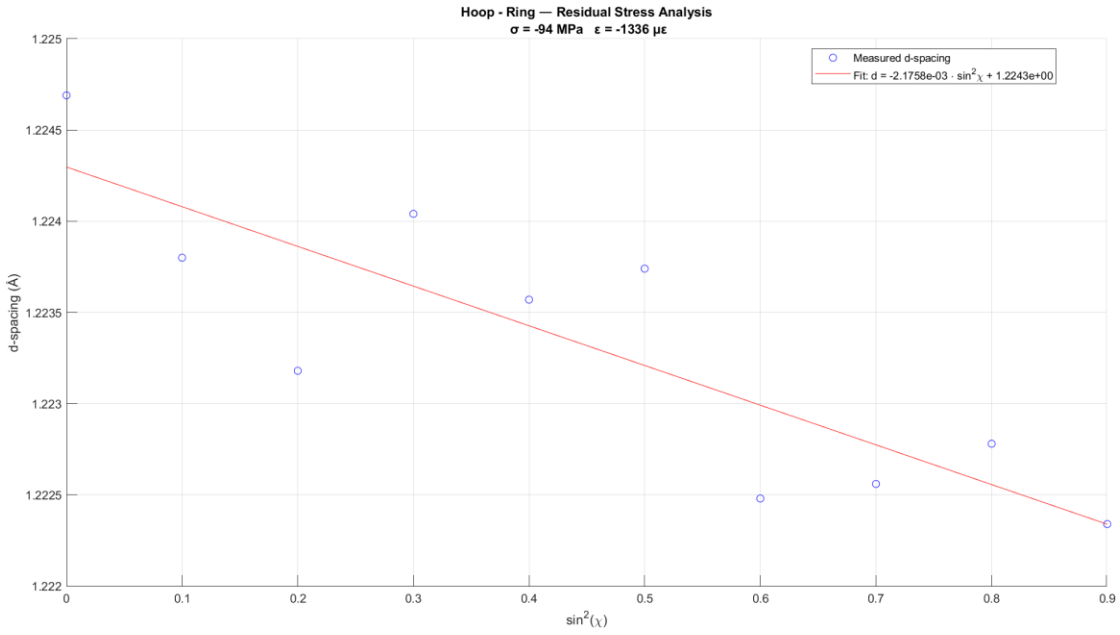


Figure 74: XRD Hoop Ring Measurement d-spacing Sin^2 X linear at ¾ Radial Distance off Center

VITA

Chloe Mehelic attended the University of Tennessee Knoxville for her undergraduate degree and earned a Bachelor of Science in civil engineering with a concentration in structural and environmental engineering in May 2024. During her time as an undergraduate, Chloe was an active member and chapter founder of Alpha Omega Epsilon, the university's STEM sorority. Through this sorority, Chloe discovered her passion for research and the STEM community. Chloe began working as an undergraduate research assistant with Dr. Penumadu in the spring semester of her senior year. She began researching residual stress measurements and began her master's thesis work.

After graduating, Chloe began her Master of Science in civil engineering with a concentration in structural engineering under Dr. Penumadu's advisement at the University of Tennessee Knoxville. Her graduate work focused on residual stress measurement using incremental hole drilling with integrated 3D DIC. Her research extended over time to other methods of residual stress measurement, including diffraction-based techniques. Chloe plans to work in the field of structural forensic engineering with a focus on failure analysis after graduation.